



HAL
open science

Phonon engineering for hot-carrier solar cells

Hugo Levard

► **To cite this version:**

Hugo Levard. Phonon engineering for hot-carrier solar cells. Physics [physics]. UPMC Université Paris VI, 2015. English. NNT: . tel-01123624v1

HAL Id: tel-01123624

<https://theses.hal.science/tel-01123624v1>

Submitted on 5 Mar 2015 (v1), last revised 1 Sep 2015 (v2)

HAL is a multi-disciplinary open access archive for the deposit and dissemination of scientific research documents, whether they are published or not. The documents may come from teaching and research institutions in France or abroad, or from public or private research centers.

L'archive ouverte pluridisciplinaire **HAL**, est destinée au dépôt et à la diffusion de documents scientifiques de niveau recherche, publiés ou non, émanant des établissements d'enseignement et de recherche français ou étrangers, des laboratoires publics ou privés.



Ecole Doctorale 397

THESE DE DOCTORAT

Spécialité : Physique et Chimie des Matériaux

présentée par

Hugo LEVARD

pour obtenir le grade de

DOCTEUR DE L'UNIVERSITE PIERRE ET MARIE CURIE

Ingénierie phononique pour les cellules solaires à porteurs chauds

Soutenue le 20 janvier 2015 devant le jury composé de :

M. Sebastian VOLZ	EM2C	Rapporteur
M. Christophe DELERUE	ISEN	Rapporteur
M ^{me} Nadine WITKOWSKI	INSP	Examineur
M. Bernard JUSSERAND	INSP	Examineur
M. Philippe BARANEK	MMC	Examineur
M ^{me} Sana LARIBI	IRDEP	Encadrant
M. Jean-François GUILLEMOLES	IRDEP	Directeur de thèse

IRDEP - EDF R&D
Bat. K
6, quai Watier
78400 Chatou

Ecole doctorale ED397
Physique et Chimie des Matériaux
4 place Jussieu
75 252 Paris cedex 05



Ecole Doctorale 397

THESE DE DOCTORAT

Spécialité : Physique et Chimie des Matériaux

présentée par

Hugo LEVARD

pour obtenir le grade de

DOCTEUR DE L'UNIVERSITE PIERRE ET MARIE CURIE

Phonon Engineering for Hot-Carrier Solar Cells

Soutenue le 20 janvier 2015 devant le jury composé de :

M. Sebastian VOLZ	EM2C	Rapporteur
M. Christophe DELERUE	ISEN	Rapporteur
M ^{me} Nadine WITKOWSKI	INSP	Examineur
M. Bernard JUSSERAND	INSP	Examineur
M. Philippe BARANEK	MMC	Examineur
M ^{me} Sana LARIBI	IRDEP	Encadrant
M. Jean-François GUILLEMOLES	IRDEP	Directeur de thèse

IRDEP - EDF R&D
Bat. K
6, quai Watier
78400 Chatou

Ecole doctorale ED397
Physique et Chimie des Matériaux
4 place Jussieu
75 252 Paris cedex 05

*[...] Two roads diverged in a wood and I-
I took the one less traveled by,
And that has made all the difference.*

ROBERT FROST

Remerciements

Comme le reste du tapuscrit, ces remerciements seront *ab initio*, mentionnant *depuis les origines* tous ceux qui, de près ou de loin, sont impliqués dans la venue au monde de cet ouvrage.

Un de mes premiers gestes en m'installant à mon bureau le jour de mon arrivée au laboratoire, le lundi 12 septembre 2011, fut de noter sur un post-it "*Penser à remercier MBB*". Le post-it s'est révélé inutile puisque je ne l'ai jamais oublié. Aussi ce n'est pas sans émotion que je commence ce petit livre en remerciant chaleureusement Marie-Bénédicte de Bournonville, ancien professeur de physique et chimie au collège-lycée Saint Jean de Passy, à Paris, qui pendant quatre années a nourri ma curiosité scientifique naissante. D'elle en premier j'ai entendu le mot *recherche*, et il ne fait aucun doute que son influence fut décisive dans le choix d'orienter mon cursus vers des études universitaires plutôt que vers le duo classique prépa-école.

Plus proche de nous, j'ai chaque jour une dette intellectuelle incommensurable envers Claude Aslangul, professeur de mathématiques (dites *pour physiciens*) en deuxième et troisième année de licence, puis de mécanique quantique en première année de master, à l'université Pierre et Marie Curie. Grâce à lui, 2009 fut l'année d'étude la plus stimulante d'entre toutes. Je suis fier, passant chez Gibert, de voir que ses (énormes) volumes de cours, fruits d'une vie d'enseignements, sont désormais exposés juste à côté du sacro-saint Cohen-Tannoudji. Je garde également un souvenir fort des cours de physique statistique de Thierry Hocquet lors de cette même année. Il est le premier à m'avoir initié à la physique des phonons, chapitre du cours que j'ai détesté à l'époque. Soulagé d'apprendre qu'il ne figurerait pas au programme de l'examen, l'ironie du sort a voulu que j'y consacre finalement, en stage puis en thèse, quatre ans de recherche.

L'autre composante majeure de ce travail est le traitement numérique des problèmes de physique, discipline découverte et adorée en premier lieu grâce à Philippe Depondt, professeur de physique numérique, en licence, puis en master ; à Fabio Finocchi, ensuite, pour les méthodes *ab initio* ; enfin, à Philippe Baranek, lors de mon stage de master 2, pendant lequel j'ai acquis des bases indispensables sans lesquelles cette thèse n'aurait pas pu être menée à bien.

La thèse, justement. J'exprime ma profonde reconnaissance à Yves Schlumberger, en son

temps, suivi par Matthieu Versavel, chefs du groupe EDF de l'IRDEP, à Daniel Lincot, directeur du laboratoire, et surtout à Sana Laribi, mon encadrant, à qui je dois un cadre de travail exceptionnel qui ferait pâlir nombre de doctorants en France et dans le monde : d'une part par un accès quasi-illimité à des infrastructures de calcul hpc, et d'autre part par la possibilité d'être allé présenter mes travaux dans sept pays, sur trois continents.

Vient celui qui est à l'origine de toutes les idées maîtresses de ce travail : ma gratitude va à Jean-François Guillemoles, auquel j'ai déjà eu l'occasion de dire que mon admiration ne se limite pas à sa fulgurance d'esprit, mais aussi à sa patience quand il s'agit de diplomatie. Ses surnoms sont nombreux, mais je ne retiendrai que "*l'homme toujours souriant à la poigne de fer*".

Remercier c'est aussi prendre le temps de figer dans l'écrit les souvenirs que l'on garde de chacun au cours d'une journée. Aussi pensé-je aux matinaux, d'abord, ceux avec lesquels j'ai épluché les torchons gratuits du matin, Sébastien Jutteau, Alain Portesse, Samuel Rives, Cédric Guérard, Julien Couderc. Puis mes voisins de bureau, Anne-Laure Joudrier, toujours de bonne humeur, et Florian Proise, qui m'a gratifié d'interminables chemine-ments scientifiques oraux, entrecoupés de surréelles interprétations a cappella de chansons de Brassens et de sonneries de porte.

J'ai évolué pendant trois ans à l'intersection de deux triumvirats. Le premier, celui des cellules solaires à porteurs chauds, au sein duquel Jean Rodière, François Gibelli et moi-même nous sommes soutenus dans notre acharnement à les faire passer de la science fiction à une réalité future. Le second, celui de la simulation *ab initio*, avec Julien Vidal et Eric Tea, pour lesquels la phrase "*Ah bah c'est sûr si tu mets un cutoff de 2 Rydberg tu vas ouvrir un gap !*" sonne effectivement comme une histoire drôle.

Il y a celles sans qui l'espérance de vie du laboratoire tomberait à une demi-journée, Claire Vialette et Mireille Owona-Ngono, nos chères co-directrices, et Sophie Gaillard notre ange gardien. Les membres du fight club de milieu de journée, Grégory Savidand et Florian Proise. Ceux qui m'ont fait rire aux larmes à l'heure du café, Laurent Lombez et Jean Rousset. Ceux avec qui le plaisir de la conversation s'élève subitement vers des sommets, Myriam Paire et Daniel ory. Ceux avec qui j'ai échangé des fiches de lecture, Loraine Duclaux et Aurélien Duchâtelet. Ceux avec qui j'ai partagé le soir mon goût de la bonne chère et ma prétendue science du vin, Cathy Bugot, Marie Jubaut & Fredrique Donsanti, Sébastien Delbos, Pierre Rale, Jorge Posada, Torben Klinkert. Ceux qui nuitamment, enfin, se sont risqués à me suivre dans les sous-sols de Paris (et qui en sont revenus), Nathanaelle Schneider et Serena Gallanti, Fabien Molica, Laurent Lombez, Torben Klinkert, Jorge Posada et Amaury Delamarre, Pierre Rale et Jean Rodière.

Il paraît que la section *remerciements* d'un tapuscrit de thèse est de toutes la plus lue. Chers lecteurs, gardez-vous de l'envie d'appliquer une herméneutique complexe à ces quelques lignes, car elles n'en suggèrent pas plus qu'elles n'en disent.

Contents

Introduction	13
1 The Hot-Carrier Solar Cell	17
1.1 Third generation Photovoltaics: beyond the Shockley-Queisser limit	18
1.1.1 The last decade objective	18
1.1.2 "There's plenty of room above"	19
1.1.3 Promising already existing technologies	19
1.2 Carrier cooling, the hot topic	20
1.2.1 Carrier-carrier scattering	21
1.2.2 Intravalley versus intervalley scattering	22
1.2.3 Auger scattering and carrier multiplication	25
1.2.4 The role of phonons in carrier cooling	25
1.3 Hot Carrier Solar Cell: the ultimate PV device	26
1.3.1 Principle and comparison with a single p-n junction solar cell	26
1.3.2 Maximum efficiencies expected	26
1.3.3 Recent experimental achievements on hot-carrier solar cell issues . .	27
1.4 Materials for hot-carrier solar cell absorber	30
1.4.1 Carrier cooling and atomic scale engineering	30
1.4.2 Formal requirements	32
1.4.3 Physical challenges for materials science	33
1.5 Open questions	33
2 Phonons: density of final states	35
2.1 The Physics of phonons	36
2.1.1 Interatomic force constants	36
2.1.2 Equation of motion, dynamical matrix and secular equation	37
2.1.3 Phonon dispersion and one-phonon density of states	38
2.2 Phonon decay	39
2.2.1 Conservation rules	39
2.2.2 Decay channels nomenclature	39
2.2.3 Engineering phonon band structure for hot-carrier solar cells	40
2.2.4 Need for a complete picture	41

2.3	Phonons within Density Functional Perturbation Theory	42
2.3.1	Principle and formalism	42
2.3.2	Successes and limitations	44
2.4	Two-phonon final states in bulk semiconductors	45
2.4.1	Practical implementation	45
2.4.2	Detailed two-phonon states analysis	46
2.4.3	Discussion	52
2.5	Gaps in the density of states of nanostructured materials	53
2.5.1	Practical implementation of PhDOS calculation on large systems . .	53
2.5.2	Application to superlattices	54
2.5.3	Application to quantum dots	54
2.6	Gaps in the density of states, a lost cause ?	56
2.6.1	Superlattice: how gaps are filled	56
2.6.2	Quantum dot: how gaps vanish because dots are not round	57
2.6.3	How it turns out that gaps are sufficient but not necessary	58
2.7	Conclusion on the two-phonon final states investigation	59
3	Phonons: decay rate	61
3.1	LO-phonon lifetime	62
3.1.1	Phonon decay from experiment	62
3.1.2	Lifetime in bulk materials	62
3.2	Formalism - Beyond the harmonic approximation	63
3.2.1	Derivation	63
3.2.2	State of the art of phonon lifetime calculation	65
3.2.3	Drawbacks of tantalizing approximations	65
3.2.4	Misleading success in fitting experimental data	66
3.3	Third order anharmonic tensor within DFPT	67
3.4	Practical implementation	69
3.4.1	Phonons eigenvectors and eigenfrequencies	69
3.4.2	q-space mesh and energy smearing	69
3.4.3	The two-phonon density of final states	71
3.4.4	Validation and commentary on DFPT for HCSC	72
3.5	Application to SiSn	73
3.5.1	Two-phonon density of states	73
3.5.2	Lifetime of the LO-phonon: beyond the zone centre approximation .	74
3.5.3	Lifetime dependence on the LO-phonon reciprocal position	75
3.5.4	Eventual photovoltaic efficiency	76
3.6	Towards higher orders-phonon processes	77
3.6.1	Previous discussions on four-phonon processes	77
3.6.2	Estimation of the four-phonon processes contribution	79
3.6.3	Consecutive three-phonon processes	80

3.6.4	Crystal symmetry and higher-order anharmonic tensors	82
3.7	Conclusions on LO phonon lifetime calculations for HCSC	84
3.7.1	SiSn features as references	84
3.7.2	Limitations	85
3.7.3	Towards other ways to hinder carrier cooling	85
4	Electron-phonon interaction	87
4.1	Dimensionality issue	88
4.1.1	Electron cooling in superlattices	88
4.1.2	Self-induced electric field and intraband scattering	89
4.1.3	$[\text{InAs}]_n\text{-}[\text{GaAs}]_n$	89
4.2	Directionally dependent electron-phonon interaction model	89
4.2.1	Electron-phonon coupling strength	90
4.2.2	Electron wave function	92
4.2.3	Electron evolution equations	93
4.3	Full-band cascade: practical implementation	93
4.3.1	Electronic band	93
4.3.2	Phonon polar field	94
4.3.3	Electronic cascade	94
4.3.4	Validation: bulk case	95
4.4	Effects of the superlattice size	96
4.4.1	Effect on the electric field	97
4.4.2	Effect on the electron-phonon interaction dimensionality	100
4.5	Conclusions on the electron-phonon interaction in superlattices	103
4.5.1	Approach and results	103
4.5.2	Approximations and subsequent limitations	103
4.5.3	Perspective on the hot-carrier effect in superlattices	103
	Conclusion	105
	A Elements of Density Functional Theory	109
	B Elements of Density Functional Perturbation Theory	111
	C SiSn electronic band structure	113
	D DFT calculation using hybrid functional	115
	E Transferability of the interatomic force constants	117
	F Conservation rules Gaussian width	119
	G Average fourth-order phonon-phonon coupling constant	121

Résumé en français	123
Bibliography	137
Notations	151
List of publications	153
Abstract	155
Résumé court en français	157

Introduction

Concerning Photovoltaics

Contravening to the well established tradition according to which one must find in the introduction of a doctoral thesis dealing with photovoltaic technology a long pro-solar energy argumentation, I will directly jump to the exciting topic of future generation concepts, guiding the readers who are not convinced by the necessity to diversify energy sources to appropriate literature, namely, for instance, the remarkable review of A. Luque on the race toward 50% efficiency [1].

The current question is not "*will it work ?*" but rather "*how well can it work in practice ?*". The famous *Shockley-Queisser limit* [2], theorised more than fifty years ago, and that states the upper photovoltaic conversion limit to 31%, was definitely an objective for the last decade. The 2010s are the years of third generation concepts, beyond single p-n junction technologies, and among these, the ultimate photovoltaic device that is the hot-carrier solar cell.

Imagined in 1982 by R. T. Ross and A. J. Nozik [3], it is expected to have a maximum efficiency of the order of the thermodynamical limit [4], and is the *most simple* implementation of photovoltaic energy extraction principle, as it primarily works on charge carriers separation.

The missing link between the concept and the practical realisation is our understanding of some fundamental physical mechanism, so to choose the appropriate materials. But the good news is that hot-carrier solar cells benefit from the exponentially increasing number of works devoted to photovoltaics technologies (figure 1). Significant improvements in the field have then to be expected in the coming years.

Hot-carrier solar cells and Material Physics

With new technologies come fundamental scientific issues which, in the case of hot-carrier solar cells, have a lot to do with interactions between the condensed matter fundamental particles and quasi-particles. The reason indeed for which charge carriers, after

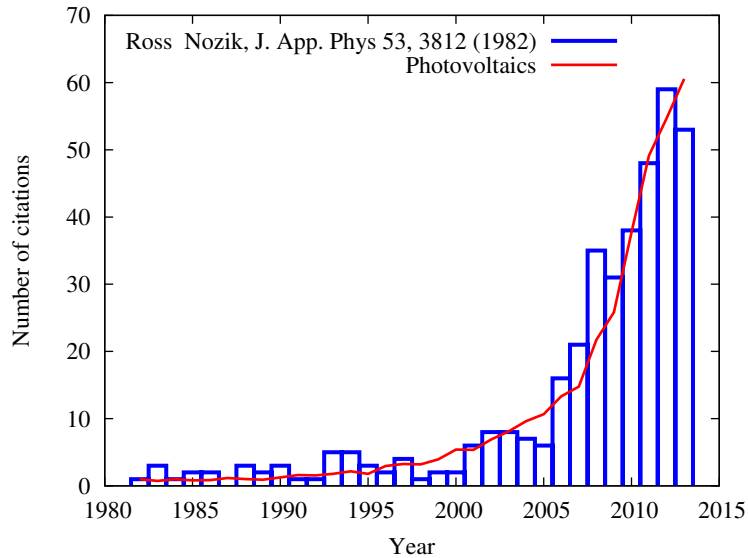


Figure 1: Number of publications referring to the initiating 1982 paper of R. T. Ross and A. J. Nozik on hot-carrier solar cells (blue), compared to the relative increase of publications related to photovoltaics in general (red), versus year.

having been photoexcited, lose their energy is because of their coupling with the atomic environment. The quanta of exchanged energy here are phonons, or elementary vibrations of the lattice, and the loss mechanism then is the *electron-phonon interaction*. But what is yielded can be regained, and carriers may also absorb phonons provided the latter do not decay "too quickly" through *phonon-phonon interaction*.

Research on hot-carrier solar cells absorber materials thus requires to be conducted from the atomic to nanometric scale to first understand experimental existing evidence of the hot-carrier effect, in order then to make predictions on the materials of interest for future devices. *First principle* modelling methods have proven their efficiency and accuracy on such small-sized systems, and the constantly increasing of computational power makes them more and more convenient for this aim.

As demonstrated in A. Luque's review [1], efficiency is the key for the photovoltaic technology to be viable. Not only are the hot-carrier solar cells the most simple one, but they are expected to be able to reach higher efficiency than any other cell [4]. The difficult part is, through our willing to prevent hot carriers from cooling, that we want to slow Nature down.

Outline

This thesis is divided into four chapters. The second and the third ones are closely related and deal with phonon-phonon interaction, while the fourth one deals with electron-

phonon interaction. *Ab initio* computational methods are used for this purpose, namely Density Functional Theory for electronic band features using the VASP code [5], and Density Functional Perturbation Theory for the physics of phonons as implemented in the Quantum Espresso package [6], not to mention the home-made programs for post-processing each these and for coupling the two.

The first chapter is a journey from the classical photovoltaic single p-n junction to the hot-carrier solar cell main issues. The questions related to fundamental Material Science that the concept of hot-carrier solar cell rises are highlighted, and in particular the role of *LO*-phonons. The intricating between hot-carrier solar cells success and a deeper understanding of the physics of phonons from what it is today is emphasised.

The second chapter deals with *LO*-phonon decay in semiconductors. A detailed study of the available final states upon the atomic mass ratio and the *LO*-*TO* splitting is performed in various bulk III-V and group-IV semiconductors, as well as two superlattices examples. Discriminating criteria for absorber selection from a phonon point of view are set, and the question of nanostructuration for *LO*-phonon decay prevention is discussed.

One step further, the third chapter is dedicated to the study of *LO*-phonon lifetime in one singular material standing out from chapter 2. Specific two-phonon characteristics are shown as targets for candidate absorbers. The question of the relevance to use Density Functional Perturbation Theory for this aim is addressed. Open remarks are risen on higher-order phonon processes.

The fourth chapter intends to contribute to the exploration of the intermediate region between bulk and quantum well materials, namely superlattices, from an electron-phonon interaction and a hot-carrier solar cell point of view. A model is proposed to study the evolution of the former strength upon the cell size, and eventually on the dimensionality of the coupled electron and phonon populations. The final results highligh that phonon-phonon and electron-phonon interactions issues should not be treated separately.

Chapter 1

The Hot-Carrier Solar Cell

Contents

1.1	Third generation Photovoltaics: beyond the Shockley-Queisser limit	18
1.1.1	The last decade objective	18
1.1.2	"There's plenty of room above"	19
1.1.3	Promising already existing technologies	19
1.2	Carrier cooling, the hot topic	20
1.2.1	Carrier-carrier scattering	21
1.2.2	Intravalley versus intervalley scattering	22
1.2.3	Auger scattering and carrier multiplication	25
1.2.4	The role of phonons in carrier cooling	25
1.3	Hot Carrier Solar Cell: the ultimate PV device	26
1.3.1	Principle and comparison with a single p-n junction solar cell . .	26
1.3.2	Maximum efficiencies expected	26
1.3.3	Recent experimental achievements on hot-carrier solar cell issues	27
1.4	Materials for hot-carrier solar cell absorber	30
1.4.1	Carrier cooling and atomic scale engineering	30
1.4.2	Formal requirements	32
1.4.3	Physical challenges for materials science	33
1.5	Open questions	33

1.1 Third generation Photovoltaics: beyond the Shockley-Queisser limit

1.1.1 The last decade objective

In 1961, W. Shockley and H. J. Queisser established the theoretical highest possible conversion efficiency of a single p-n junction photovoltaic solar cell [2]. Known as the Shockley-Queisser limit, it is a function of the absorber band gap (E_g) and of the solid angle collection: known as the solar concentration, it is expressed in number of *sun*, and takes a value between one (no concentration device) and approximately 46 000 suns (*maximum concentration*), depending on the concentration device. Within the Shockley-Queisser limit, the maximum efficiency a photovoltaic device can reach is 31% under one sun for $E_g = 1.4 \text{ eV}$ [4] (41% under maximum concentration). It should be noted that Silicon and Gallium Arsenide have a band gap that is close to this optimal value, respectively 1.12 eV and 1.42 eV : in 2010, the world record conversion yield of solar cells with an Si absorber was 24.7% (UNSW), and 25.9% with a GaAs absorber (Radboud University), both without concentration. As we get closer to the maximum attainable efficiency, research in Photovoltaics is diversified and explores beyond-Shockley-Queisser technologies, that are gathered under the name *Third Generation Photovoltaics*.

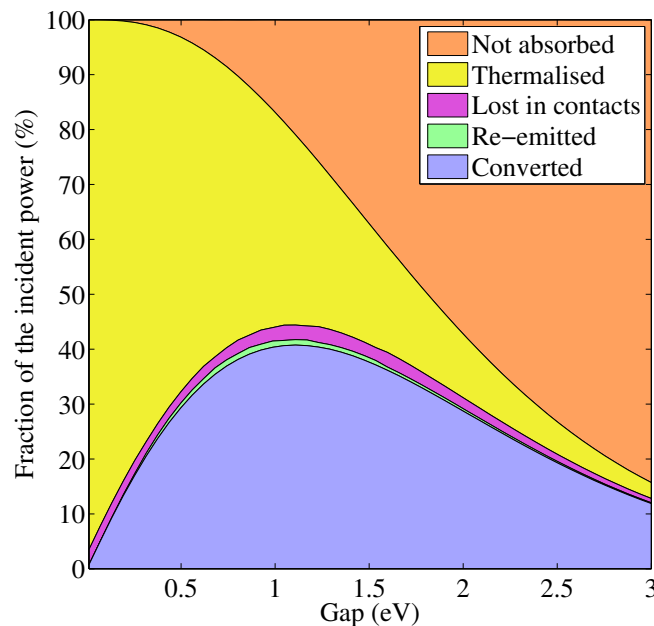


Figure 1.1: Efficiency and losses (non absorption, thermalisation, extraction, and recombination) as a function of the absorbing material band gap, under AM1.0 incident spectrum. An optimal conversion efficiency of 31% is obtained for a 1.4 eV band gap. Reproduced from [7]

1.1.2 "There's plenty of room above"

Figure 1.1 allows an immediate identification of the mechanisms limiting the photovoltaic conversion. Re-emission and loss in contacts contribute faintly to the global waste. The unabsorbed part simply comes from photons whose energy is lower than the absorber band gap, hence that cannot generate an electron-hole pair. This is the evident reason for which single junction photovoltaic technologies requires reasonably low band gap, typically between 1.0 and 1.4 eV [4]. From this latter value and below, the main loss mechanism is labelled *thermalisation*, a rather "catch-all" term gathering several processes that will be itemised in this chapter.

1.1.3 Promising already existing technologies

Third generation photovoltaic technologies thus aim at overstepping unabsorption and *thermalisation*. A brief description of the four major current ones is given below, together with the latest striking achievements in their respective field. An illustration of their operating condition from an electronic band structure point of view is reproduced in figure 1.2.

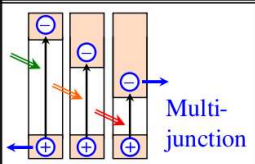
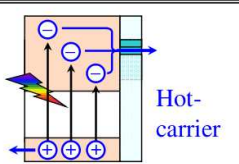
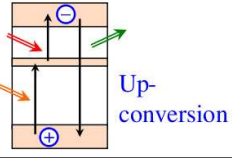
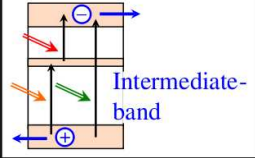
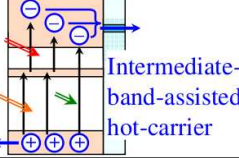
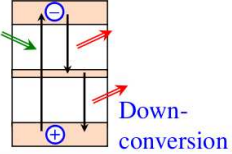
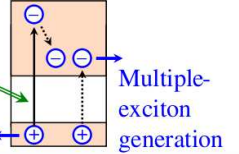
	Spectral conversion	Spectral splitting	Using excess energy
1 photon ↓ 1 electron			
2 particles (low energy) ↓ 1 particle (high energy)			
1 particle (high energy) ↓ 2 particles (low energy)			

Figure 1.2: Types of solar cells to exceed the Shockley-Queisser limit. Reproduced from [8]

Multijunctions

A multijunctions solar cell consists in a stack of different single p-n junctions with decreasing gap ordering, so that the highest gap absorber faces the incoming sun light [9]. Both the *thermalisation* loss and the unabsorbed number of photons are reduced. The total theoretical conversion efficiency is of 42.7%, 49.1%, and 53.0% under one sun (respectively 55.9%, 63.8% and 68.8% under maximum concentration) for a well chosen stack of 2, 3

and 4 junctions [10, 11], and in the limit of an infinite stack of single p-n junctions, the conversion efficiency was calculated to be 86.8% [10]. In August 2014, the photovoltaic conversion world record is held by the Soitec company, with a yield of 44.7% obtained with a GaInP/GaAs/GaInAsP/GaInAs four-junction cell [12].

Intermediate band

Intermediate-band solar cells can be viewed as intrinsic three-junction cells: an additional level lies in the band gap region, so that promoting an electron from the valence band to the conduction band requires either a photon whose energy is at least equal to the band gap, or two photons, exciting the electron in a two-step process through the intermediate level. The latter can be an impurity state [13] or a continuous narrow band that may exist in low dimensional systems [14]. The limiting efficiency is the same as for a three-junction cell [15] (49.1%, or 63.8% under maximum concentration). The intermediate-band solar cell was experimentally demonstrated in 2006 in InAs/(Al,Ga)As quantum dots [16].

Up/Down-conversion

What multijunctions and intermediate-band solar cells are thought to deal with is the polychromatic nature of light. Instead of tuning the device to fit the photons energy, another approach then consists in tuning the photons energy to fit a single-junction band gap, i.e. quantum cutting photons whose energy is at least twice the one of the band gap (down-conversion), or merging low energy photons (up-conversion). Down-conversion, requiring a quantum efficiency greater than 1, is difficult to realise in practice [13], explaining why most of the research is focusing on up-converter materials. The highest achievable efficiency is the same as for an intermediate band solar cell [13], and most experimental progresses had been made using rare earth elements [17] and their coupling with plasmonic structures [18].

Hot carriers

Beyond the obstacle of the number of junctions or the individual photon energy in the photovoltaic cell operating is the simple idea of charges separation and extraction. As the quasi-Fermi levels splitting rules the voltage achieved from the cell, the highest potential difference that can be obtained would be if the carriers were extracted from the absorber well above the band gap, in a *hot* state. The practical implementation of this concept, detailed in section (1.3), first requires a deep understanding of the hot carriers cooling phenomenon.

1.2 Carrier cooling, the hot topic

In this section is recalled the non-radiative physical processes that are responsible for the carriers average energy modification after photoexcitation. The distinction between

carrier cooling and thermalisation is clarified because of their being often semantically blended [14], although they refer to distinct physical mechanisms.

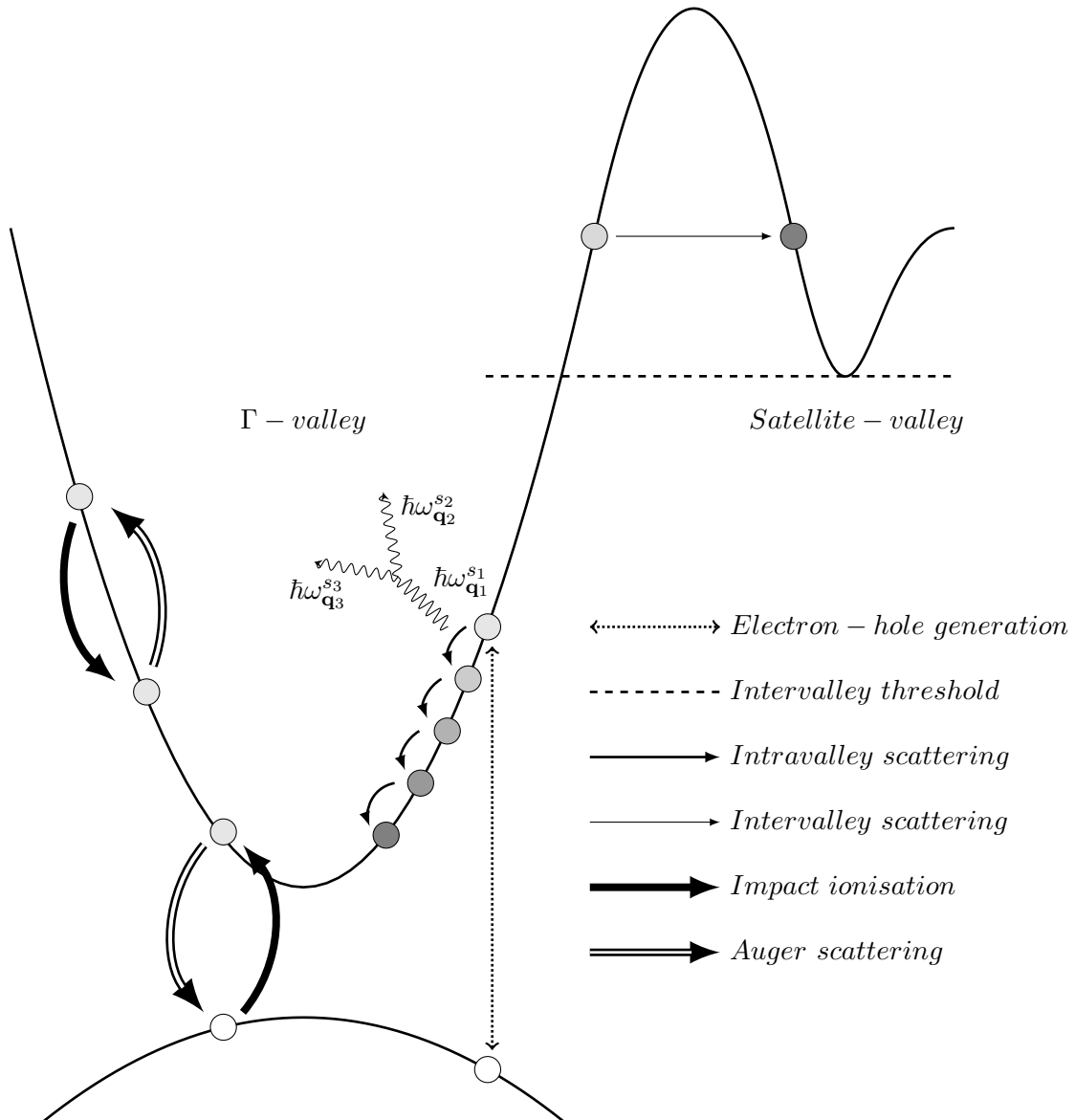


Figure 1.3: Hot electrons cooling processes.

1.2.1 Carrier-carrier scattering

After being photogenerated, the electrons and the holes are said "hot" in a sense that they carry excess energy compared to the band gap. S. A. Lyon gave this definition in his 1986-review:

By "hot carriers" we mean electrons or holes with kinetic energies well above the average thermal energy of the lattice, characterized by kT_L . In general the carriers

are not in an equilibrium distribution, and "hot" does not imply that their distribution can be characterised by a carrier temperature. [19]

Within the first tenths of femtosecond after photogeneration, though, the elastic carrier-carrier interaction dominates and equilibrates the kinetic energies, so that a carrier temperature can be defined [20, 21]. This is called the thermalisation process, and has to be distinguished from the cooling processes, which take place on a longer time-scale. From this point, "hot carriers" definition is to be understood as a *thermalised version* of Lyon's, i.e. as a steady state population of carriers whose average energy is well above the band gap. In practice, working in the steady state regime and being able to define a carrier temperature [7], hereafter labelled T_C , allows to study experimentally the hot carriers energy relaxation with photoluminescence spectroscopy [21, 22].

1.2.2 Intravalley versus intervalley scattering

The cooling processes gather most of the phenomena responsible for the average (thermalised) carrier energy to drop at a level close to the conduction band minimum (CBM) for the electrons, or to the valence band maximum (VBM) for the holes. These are the electron/hole-phonon scattering mechanisms. They consist of unelastic interactions of the carriers with the lattice, *unelastic* in the sense that the carriers energy is not conserved: the loss in energy and momentum is carried by quasi-particles, quanta of atomic vibration, also known as phonons [23, 19]. In the following we will focus on electrons, because only a small part of the photon energy is given to the holes due to their larger effective mass [24, 25].

A distinction is to be made between interband and intraband scattering, since their dominance one over the other is dependent upon the excited electron energy together with the electronic band structure, and because the nature of their coupling with lattice vibrations is of different nature (figure 1.3). The intravalley scattering involves the charge carrier scattering with polar phonons (long wavelength longitudinal optic phonons [26]) through the material polarisation these phonon modes create, whereas the intervalley is dominated by the interaction with short-wavelength phonons, either optic or acoustic [24, 27, 28], through an intervalley deformation potential [28]. The polar intravalley scattering was first theorised by Fröhlich [29], and is often simply referred to as the *Fröhlich interaction*. The experimental truth teaches us that the intervalley scattering is always dominant over the intravalley scattering whenever it is energetically allowed [30, 31]. Thus if, once photogenerated, carriers reach a state from which an intervalley transition is allowed, i.e. as far as their energy is higher than the satellite valleys minimum (or *intervalley threshold energy*, dashed line in figure 1.3 for the electrons), they will undergo such a transition and rather give their excess energy to long wavevector phonons. However, quantifying the scattering times related to these processes, in order to establish their precedence order, led thirty years ago to one decade of unaccordant results. The following sections summarise

the most cited papers results on a simple III-V semiconductor, GaAs, in order to shed some light on these complex band structure phenomena.

1.2.2.1 The 80's: femtosecond luminescence spectroscopy

A significant number of subpicosecond spectroscopy measurements were performed until 1990. While a global consensus was set on the intraband polar-LO-phonon emission rate [24, 30, 32], the value of the intervalley scattering rate remained rather controversial. Table 1.1 gathered the reported data of the most cited papers related to the topic: the Γ -to- L ($\tau_{\Gamma L}$) and L -to- Γ ($\tau_{L\Gamma}$) scattering time values, particularly, scatter by an order of magnitude. It should be highlighted that the experimental conditions from one work to another differ by excitation energies and lattice temperature.

	$\tau_{\Gamma\Gamma}$	$\tau_{\Gamma X}$	$\tau_{\Gamma L}$	$\tau_{L\Gamma}$
Collins and Yu [24](10 K)	~ 0.10	$< 0.10 (\sim 0.3 \text{ eV})$	$< 0.10 (\sim 0.5 \text{ eV})$	> 0.10
Shah <i>et al.</i> [33](300 K)			0.10 (0.50 eV)	2.00
Mirlin <i>et al.</i> [30](2 K),[34](30 K)	0.20	0.25 (0.39 eV)	0.03 (0.57 eV)	
Young <i>et al.</i> [20](300 K)	0.19			1.40
Ulbrich <i>et al.</i> [32](2 K)	0.18	0.54 (0.48 eV)	0.18 (0.58 eV)	

Table 1.1: Intra- ($\tau_{\Gamma\Gamma}$) and intervalley ($\tau_{\Gamma X}$, $\tau_{\Gamma L}$, $\tau_{L\Gamma}$) scattering time according to different authors. All the values are in *ps*. The initial electron energy is indicated in brackets for the transitions from the Γ -valley to satellite-valleys, while, for the L -to- Γ transition, it was always considered to be bottom of the L -valley. The working lattice temperature is indicated for each reference.

1.2.2.2 The 90's: empirical pseudopotentials calculations

A series of works [35, 28, 36, 37, 38] published in the early 1990's by S. Zollner, S. Gopalan and M. Cardona brought new comprehension elements on the large experimental range of results. Using a *rigid-pseudion* model [28], they calculated the intervalley deformation potentials (IDP) in GaAs, whose detailed analysis revealed the following fundamental properties: (i) the IDP are strongly \mathbf{k} -dependent, \mathbf{k} being the initial electron wavevector; (ii) when initial and final states are taken elsewhere than strictly at valley bottom, symmetry breaking allows so far-forbidden phonon assisted transitions to greatly contribute to the scattering; (iii) as a consequence of (i) and (ii), the scattering rates are also dependent on both the lattice temperature (because of its impact on the phonon population) and the electronic temperature.

These conclusions explain why the comparison of experimental results with simple models may fail; in particular, Zollner and co-workers show the considerable importance to take into account TA-phonon mediated transitions from satellite valleys to the Γ -valley, which is missing when considering highly symmetrical initial and final electron states [39, 27].

They also showed that an electron in the X-valley has a probability to scatter in the L-

T (K)	$\tau_{\Gamma L}$	$\tau_{\Gamma X}$	$\tau_{L\Gamma}$	τ_{XL}
10	0.75 ps (165 meV)	0.40 ps (200meV)	6.60 ps	0.41 ps
300			2.20 ps	0.13 ps

Table 1.2: Intervalley scattering rate according to Zollner and co-workers [35, 28, 36, 37, 38] for different lattice temperatures T . The initial electron energy above the $\Gamma - L$ threshold is indicated in brackets for the transitions from the Γ -valley to the satellite valleys, while it was taken as the minimum of the satellite-valleys for the back-to- Γ scattering transitions. It should be noted that the ΓX scattering time, because of the highest energy position of the X -valley compared to the L -valley, physically reflects transitions in both valleys and not only in the former.

valley four times higher than to scatter back into the Γ -valley, so that they consider more relevant to focus on determining τ_{XL} rather than $\tau_{X\Gamma}$. Table 1.2 gathers some of their main results, and we can notice a very good agreement with Ulbrich group's ones [32] reported in table 1.1. It is worth noting that the estimated uncertainties on the experimentally determined/calculated deformation potential are also of comparable amplitude in both studies, i.e. 20% (see [36] for a more detailed insight into this agreement).

1.2.2.3 The 2000's: *ab initio* calculations

Full *ab initio* calculations of the deformation potential and intervalley scattering time in the mid-2000's were carried out by J. Sjakste and co-workers, who found a L-to- Γ transition time of 1.5 ps (4.5 ps) for a lattice temperature of 300K (0K) [40, 41, 42], with an estimated error bar of 0.2 ps. The discrepancy of this value compared to Zollner's work has been attributed by the authors to a consequence of their accurate treatment of the screening potential generated by the intermediate phonon in the scattering process. However, these values remain in the same order of magnitude, strengthening both Zollner and Sjakste group's results.

1.2.2.4 Conclusion on the intravalley/intervalley competition

Matching experimental results and theoretical understanding of intervalley scattering turns out to be extremely complex, due to the multiple interdependency of the electronic band parameters and of the electron-phonon interaction itself [36, 41]. However, we shall retain for the following sections that above the intervalley threshold, the intervalley transition time is at most as high as the intravalley one, making it the dominant scattering process in this energy range. Below the threshold, conservation of energy and momentum restrains the relevant intermediate phonons to the ones with a wavevector close to the Brillouin zone-center, i.e. of the order of few 10^7 cm^{-1} [21]. In non-polar materials, they are the *longitudinal optic* (*LO*) and *transverse optic* (*TO*) phonons. In polar materials,

the atomic displacements related to the LO-phonon modes induce an electric field that makes the coupling between the electron and this phonon largely dominant over the coupling with the TO-phonon [26], so that in the intravalley energy range we only have to deal with the electron-LO-phonon interaction.

1.2.3 Auger scattering and carrier multiplication

Auger scattering and carrier multiplication are opposite phenomena (figure 1.3), and belong to the inelastic-type scattering as the number of particles is not conserved. The latter involves the recombination of an electron with a hole, whose resulting photon is absorbed by another conduction electron, while the former refers to an intraband transition whose released energy is captured by a valence electron then promoted to the conduction band. These processes have a characteristic time of 10^2 ps [21], and are dependent upon the carrier density and the band gap. Those are not strictly speaking "cooling processes", but interfere on a long time scale in the establishment of the average carrier temperature.

1.2.4 The role of phonons in carrier cooling

LO-phonons emitted from intraband scattering are not stable (figure 1.3), but decay into lower energy phonons within few picoseconds [43]. A detailed description of this process will be given in chapter II and III. Previous to this decay, there is a certain probability, related precisely to the phonon lifetime, that the electrons would reabsorb LO-phonons. It was proven by several independent theoretical Monte Carlo studies [44, 19, 45, 46] and Boltzmann equation fitting of experimental data from room temperature femtosecond spectroscopy [47] that the hot carriers energy relaxation time is strongly dependent on the LO-phonon lifetime, and that the longer it is, the slower the cooling for both electrons and holes. As an example, table 1.3 displays the average energy and temperature of a photoexcited hot-electron population, as a function of the LO-phonon lifetime, calculated within a full-band Monte Carlo solving of the Boltzmann Transport Equation in $In_{0.53}Ga_{0.47}As$ (details about the implementation can be found in [44]). 2.5 ps

$\tau_{LO}(ps)$	$\langle E \rangle$ (eV)	T_e (K)
2.5	0.060	320
5	0.099	486
10	0.137	497
20	0.173	544

Table 1.3: Average electron distribution energy and temperature versus LO-phonon lifetime calculated using a full-band Monte-Carlo. Reproduced from [48]

corresponds to the LO-phonon lifetime at room temperature, and is representative of most of III-V semiconductors in the FCC crystal structure [49]. A gain of one order of

magnitude on this parameter induces a significant enhancement of the conduction electrons average energy: tuning the LO-phonon lifetime appears, then, as a key leverage on hot-carrier cooling dynamics, which is of fundamental significance for the *hot-carrier solar cell* concept.

1.3 Hot Carrier Solar Cell: the ultimate PV device

1.3.1 Principle and comparison with a single p-n junction solar cell

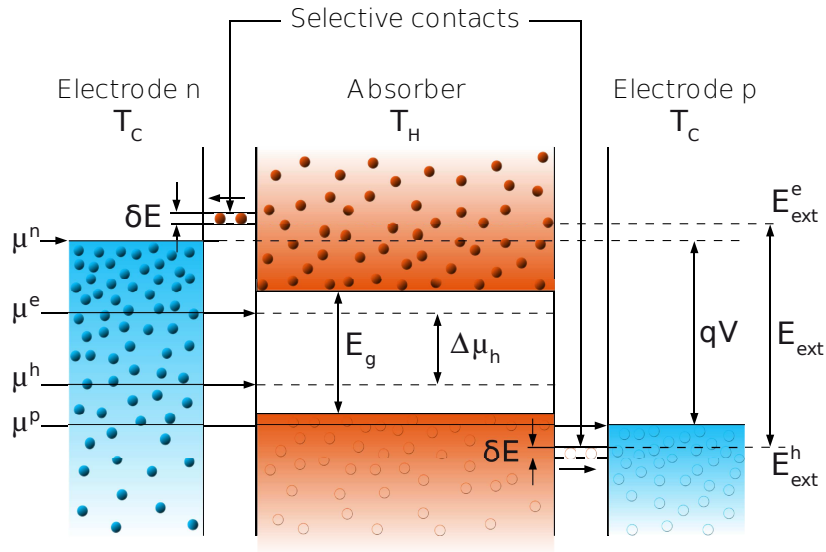


Figure 1.4: Principle of a hot-carrier solar cell. Reproduced from [7]

The principle of a hot-carrier solar cell, suggested in 1982 by R. T. Ross and A. J. Nozik [3], is depicted in figure 1.4. A photon with an energy much larger than the absorber band gap (E_g) creates an electron-hole pair, that is extracted towards the electrodes through energy selective contacts, at energies E_{ext}^e and E_{ext}^h , for the electrons and the holes respectively, so that the total extracted energy $E_{ext} = E_{ext}^e - E_{ext}^h$ is larger than E_g . Namely, the carriers are wished to be extracted in a *hot* state. The energy selective contacts width δE has to be narrow enough to prevent entropy loss during extraction, typically $\delta E \ll k_B T$ [50]. The working potential difference at the cell boundaries is the difference between the electrodes Fermi level, $qV = \mu_n - \mu_p$.

This concept rests upon the *hot-carrier effect*, the steady state population of *hot* carriers [51, 3, 52, 53].

1.3.2 Maximum efficiencies expected

As said in section (1.1.1), photovoltaic energy conversion is limited to 41% when using a single p-n junction under maximum concentration, while the thermodynamic limit is close to 86% [4]. In their original paper [3], R. T. Ross and A. J. Nozik predicted 66%

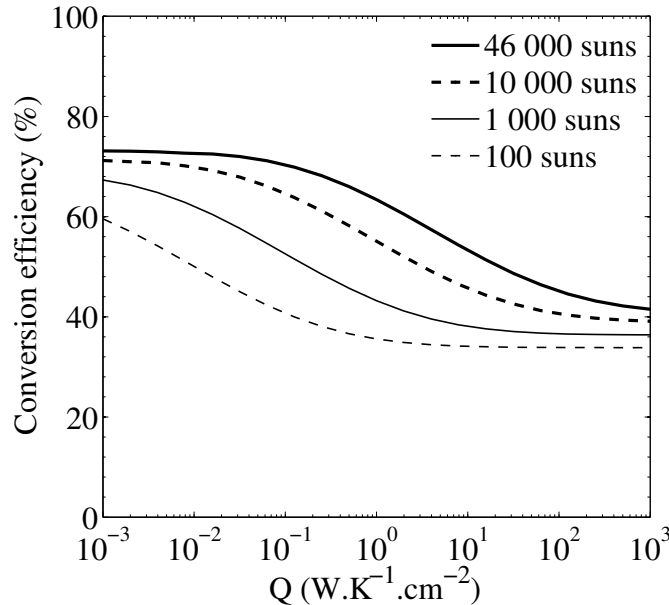


Figure 1.5: Efficiency of a hot-carrier solar cell with a 0.7 eV band gap absorber (as in GaSb) and perfectly selective contacts as a function of the thermalisation coefficient Q for different concentrations of the incident radiation. Reproduced from [7]

of maximum photovoltaic conversion, assuming no thermal contact between the electron population and the environment, namely the atomic field in the absorber. This maximum yield was then found to be close to 86% under maximum concentration [55] (see figure 1.7). To ease the practical implementation of energy selective contacts, A. Le Bris and co-workers [50] simulated the conversion efficiency as a function of the extraction energy, the contact selectivity, and a thermalisation factor Q related to the carrier cooling rate (figure 1.5). For a highly, though not infinitely, selective contact of width $\delta E = 1 \text{ meV}$, they found that the maximum efficiency is considerably lower than the thermodynamical limit when dealing with a realistic thermalisation factor (as measured in bulk GaAs, $Q = 1000 \text{ W.K}^{-1}.\text{cm}^{-2}$, or AlGaAs quantum wells, $Q = 10 \text{ W.K}^{-1}.\text{cm}^{-2}$), but still leading to more than an efficiency of 50% (figure 1.6), which is higher than the current world record with multijunctions. This result was born out by Y. Takeda and co-workers in [56]. Another result of this study is the possibility to reach such a conversion yield with semi-selective contacts, i.e. *well chosen potential barriers* [50], provided the absorber shows a thermalisation factor of $1 \text{ W.K}^{-1}.\text{cm}^{-2}$ at the most. Carrier cooling and energy selective contacts are hence the two key issues for hot-carrier solar cells fulfillment.

1.3.3 Recent experimental achievements on hot-carrier solar cell issues

Below are given the last striking experimental progress related to the hot-carrier solar cell main issues deduced from the just above conversion efficiency analysis.

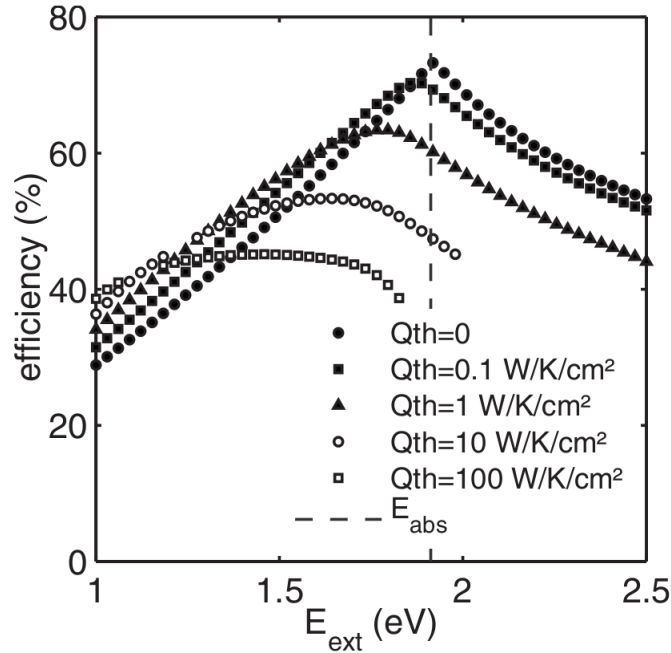


Figure 1.6: Conversion efficiency vs extraction energy at various thermalisation rate, for a 1 eV band gap absorber under maximum concentration with highly selective contacts ($\delta E = 1 \text{ meV}$). $Q = 0 \text{ W.K}^{-1}.\text{cm}^{-2}$: no thermalisation in the absorber. $Q = 100$: fast thermalisation. A value of $Q = 10 \text{ W.K}^{-1}.\text{cm}^{-2}$ was measured in GaAs quantum wells samples [54]. E_{abs} is the average energy of absorbed photons, i.e. 1.91 eV for a 6000 K black body spectrum. Reproduced from [50]

1.3.3.1 Energy selective contacts: resonant tunneling transport

Most of the research dedicated to energy selective contacts focuses on resonant tunneling transport, consisting of a low dimensional structure confined between two bulk materials, and leading to a sharp peak of the electronic transmission coefficient at particular energies [58]. It refers most of the time to quantum wells, but is also relevant for quantum dot superlattices.

Quantum wells

Electronic transport through double barrier resonant tunneling was experimentally proved in AlGaAs/GaAs/AlGaAs structures, first in 1974 by L. L. Chang and co-workers [59], and later by S. Yagi and Y. Okada [60] from an energy selective contact perspective. It reveals that quantum dot superlattices may be more relevant for the extraction purpose because of their narrower energy transmission range. However, in 2013, an AlAs/GaAs/AlAs double barrier structure was made by J. Dimmock and co-workers in a hot-carrier solar cell prototype [61]: although they could not measure the ratio of the converted over the incident energy, they experimentally demonstrated hot-carrier current extraction at zero bias.

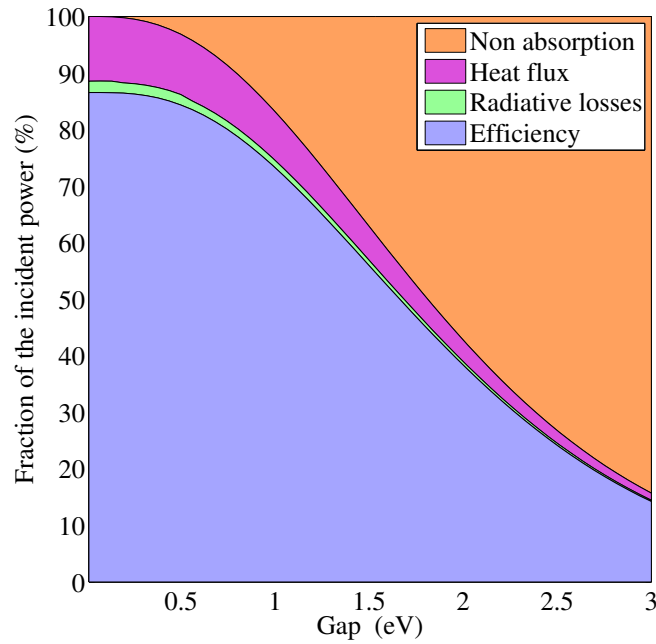


Figure 1.7: Maximum efficiency expected as a function of the electronic band gap in a hot-carrier solar cell. The energy selective contacts are assumed perfect (no entropy loss). Reproduced from [57]

Quantum dots

The discretisation of energy levels in quantum dots could allow to realise transport of carriers in a narrow energy range. The key synthesis challenge then is the homogeneity of the dots size, since non-uniformity causes widening of energy levels [62]. Despite this technical difficulty, experimental evidence of hot carriers extraction was demonstrated in 2008 and 2013, respectively by G. J. Conibeer *et al.* [63] and D. König *et al.* [64], from an Si absorber through an Si-quantum dots array embedded in an SiO₂ matrix.

1.3.3.2 Carrier temperature mapping

Opto-electronic characterisation tools are of highest importance in evidencing hot-carrier effect and hot-carrier absorber characteristics. Photoluminescence using a confocal microscope has been demonstrated to be a relevant tool for this aim [65, 22]. A significant improvement in characterising potential candidates for hot-carrier solar cell absorber was achieved in 2013 by J. Rodière [22]. From spectrally *and* spatially resolved photoluminescence, the carriers temperature T_C , the quasi-Fermi levels splitting $\Delta\mu$ and the thermalisation factor Q [57] were extracted for several light concentrations (figure 1.8). These thermodynamical quantities, although required for hot-carrier absorbers discrimination, are hardly predictable for complex systems such as quantum wells. Rodière's work allows to reach all this quantities almost simultaneously for any semiconductor. In particular, he isolated an InGaAsP multi-quantum well structure that exhibits a thermal-

isation factor of $4 \text{ W.K}^{-1}.\text{cm}^{-2}$, which, referring to figure 1.5, would lead to a conversion efficiency of almost 50% at 10 000 suns.

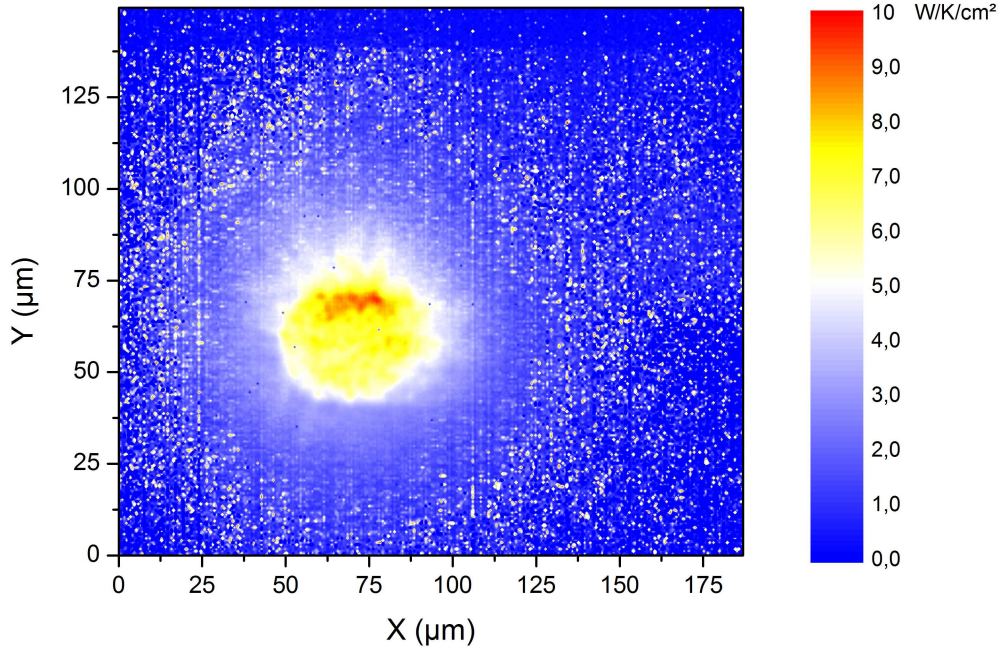


Figure 1.8: Local measurement of the thermalisation rate deduced from an absorbed power map based on integrated PL map and the corresponding local temperature map of emission under 22000 suns. Reproduced from [22]

1.4 Materials for hot-carrier solar cell absorber

After delving into the analysis of a hot-carrier solar cell operating, we face the issue of specific material criteria choices, both for the absorber and energy selective contacts. With nascent technological concepts come fundamental scientific issues: each of these two latter elements have totally different functions, and require both deep and independent investigations. In this thesis, we focus only on the absorber.

1.4.1 Carrier cooling and atomic scale engineering

As seen in section (1.3.1), carrier cooling hindering is one of the two hot-carrier solar cell challenges: we aim at designing (or discovering) a material with a low thermalisation coefficient compared to standard bulk semiconductors, i.e. of the order or lower than $1 \text{ W.K}^{-1}.\text{cm}^{-2}$, or hot-carrier relaxation time longer than 1 ns [62]. From section (1.2) on carrier cooling dynamics, two paths take shape: softening the electron-phonon interaction (what is called the *electron-phonon bottleneck*), and tuning the phonon spectrum so

to extend the LO-phonon lifetime (typically to the order of several tens of ps at 300K), increasing the reabsorption rate (the *phonon-phonon bottleneck*, or simply *phonon bottleneck*, or again *hot-phonon effect*). It is worth noting that this latter effect is only relevant for electrons below the intervalley threshold. In the following we summarise the current knowledge on these two bottlenecks.

1.4.1.1 Electron-phonon bottleneck

Interestingly, most of the experimental reports of reduced carrier thermalisation time [66, 67, 68, 54] came after R. T. Ross and A. J. Nozik essential paper on the hot-carrier solar cell concept [3]. The guiding line of these papers is the comparison of the evolution in time of the electronic temperature in bulk GaAs and GaAs/AlGaAs multi quantum wells. Whether there was or not an energy loss rate reduction in 2D systems compared to bulk was an extremely controversial topic [69, 68] until the conciliating paper of W. S. Pelouch and co-workers [68]. The main admitted conclusions about this topic are:

- The energy loss rate (ELR) of carriers is substantially reduced both in bulk and 2D systems, whatever the carrier density n_c , compared to what can be expected within the simple Fröhlich model, that assumes no electron-phonon interaction screening and a phonon population at the lattice temperature [45, 70]. This ELR reduction has different understandings, though, depending whether n_c is below or above a soft threshold carrier density estimated to be $\tilde{n}_c \approx 0.5 - 1.0 \cdot 10^{18} cm^{-3}$ [54, 70, 71, 68];
- For a given carrier density *below* \tilde{n}_c , the ELR of carriers cannot be explained by electron-phonon interaction screening effect, but can be related to a *hot-phonon* effect, i.e. reabsorption by carriers of out-of-equilibrium LO-phonons [72, 71]. In this range of density, there is no substantial difference between the carriers ELR in bulk and 2D systems, i.e. is dimensionally- and width-independent [73, 74, 70, 75, 68];
- For a given carrier density *above* \tilde{n}_c , the ELR of carriers is substantially reduced in 2D systems compared to bulk, and, in addition to the hot-phonon effect, have to be taken into account electron-phonon interaction screening effects [67, 68, 54] and dependence on \tilde{n}_c [76], as well as plasmon-phonon renormalisation of phonon modes [44, 76]. Finally, the thermalisation factor [7, 77], that is related to the thermalisation time inverse, is linearly dependent on the absorber thickness [57, 22];
- At a given average carrier temperature, the ELR of holes is one to two orders of magnitude lower than the electron one [72].

Recent theoretical works [78, 79] pointed out that considering realistic scattering times leads to the conclusion that the absorber (respectively a stack of absorbers in the case of a multi quantum wells structure) should not be thicker than 10 nm (10 nm each absorber slab) to allow the carriers to efficiently reach the contact without too much energy loss, in accordance with J. Rodière's experimental results [22]. They also highlighted the necessity of correctly including *confinement*, i.e. the modification of electron-phonon interaction in such small 2D systems.

Quantum dots have been a more recent increasing research field for hot-carrier solar cell absorber compared to quantum wells [14, 53, 62], partly because the electron-phonon bottleneck effect is thought to be very efficient, provided the energy difference between two electronic excitation levels is larger than the highest phonon energy, thus preventing carrier cooling through phonon emission [62]. Since radiative recombination would then be the dominant energy losing process, electron-hole separation is a key issue and a hot topic in quantum dot solar cells [62]. It is of fundamental importance to note that, even though dimensionality effects on ELR reduction in 2D materials is a bit better understood since W. S. Pelouch conciliation paper [68], ELR reduction in quantum dots is still a controversial topic considering the large number of papers reporting thermalisation time of the same order or even longer than in bulk materials [14, 62].

1.4.1.2 Phonon-phonon bottleneck

The basic idea of phonon engineering for hot-carrier solar cell is to restrict or deprive the LO-phonon of decay final states. From a quantum mechanical point of view, this induces a shorter transition rate from the one LO-phonon state to the two- (or more-) phonon states, hence a longer characteristic time. This has been shown to occur in binary materials exhibiting a large gap in their phonon band structure [80, 81], because of the large mass ratio between the two atoms. *InN*, for instance, received a particular attention [82, 80, 83, 84], as it was thought to be a "good" candidate due to the large mass difference between Indium and Nitrogen. However, ultrafast Raman spectroscopy experiments have shown the a wide band gap between optic and acoustic branches was not sufficient as other decay processes would occur due to a wide LO-TO splitting [85, 86]. It seems reasonable to the author to state that the LO-phonon decay has not received, from an experimental point of view, a large enough interest, so that a simple literature review could not allow to find a proper candidate, and, apart from few exceptions, theoretical studies of phonon band structure in a hot-carrier solar picture have been performed with approximated phonon band structure, and on high symmetry directions only.

1.4.2 Formal requirements

From what precedes, we can formalise the suitable requirements for a hot-carrier solar cell absorber. From a phononic point of view to start with, the following properties are considered to be beneficial [80, 87].

- (i) First, a large phononic gap between acoustic and optic branches that could be obtained with a large mass difference between the atoms in the unit cell to suppress the channels through which phonons decay into two acoustic phonons, namely the Klemens channels [43];
- (ii) secondly, a narrow LO-TO splitting to suppress Ridley channels [88], leading to one acoustic and one optic phonons;

- (iii) a relatively small LO-phonon and LA-phonon maximum energies, in order to both reduce the energy loss by LO-phonon generation and ensure property (i);
- (iv) as a final phonon requirement, a narrow optic phonon energy dispersion to minimise the Ridley-decays.

In order to absorb the widest part of the solar electromagnetic spectrum, HCSC absorber must fulfill some additional conditions regarding its electronic structure, to wit:

- (v) a low band gap (typically below 1 eV [7]) to maximise the optical absorption;
- (vi) a continuous electronic joint density of states to allow absorption of the entire solar spectrum [87];
- (vii) a low electronic effective mass to ensure a high mobility;
- (viii) finally, since no evidence of intervalley or intra-satellite-valleys scattering rate reduction has been reported so far (unlike intravalley scattering rate), so that this process is considered to be an irrepressible cooling mechanism, a band structure showing high energetic intervalley threshold, typically above 1 eV, is preferable.

1.4.3 Physical challenges for materials science

Thermalisation and cooling processes, channels and rates at the nanoscale are incidentally not only a key issue for hot-carrier solar cells. Those are common challenges shared with various semiconductor physics research fields [89, 90, 91], such as thermal transport in nanotechnologies [91], quantum computing [92], energy conversion and storage [93], and is a fundamental challenge for thermoelectricity [94] and thermionic effect [95].

1.5 Open questions

S. A. Lyon began the conclusion of his review on spectroscopy of hot carriers in semiconductors by: "*So far we have concentrated on what we think we know. Here we will summarise the accomplishments, and discuss some of what we do not know.*" [19]. In the same spirit, we will summarize the missing links in our understanding of hot-carrier cooling from a hot-carrier solar cell point of view, and propose some ways of exploration that will be developed in the next chapters.

- Study of LO-phonon decay has often suffered from its lack of precision because of rough approximation of the band structures, its representation limited to high symmetrical directions, or else the irrelevance or virtuality of the studied materials. We may legitimately ask whether a full picture of the phonon decay, using an exact band structure, would not improve our comprehension of the phenomenon and bring new clues towards finding candidates for hot-carrier solar cells absorbers. This issue will be addressed in chapters II and III.
- Electron-phonon interaction has been extensively studied in bulk as well as quantum wells of width larger than 10 nm, but the intermediate range remains under-explored.

It constitutes however the transition from the bulk to the 2D system, and is thus favourable for studying the fundamental interactions dimensionality dependence. In chapter IV will be exposed such an analysis of the electron-LO-phonon interaction in superlattices.

In both cases, and as explained all along section (1.4), a fine description of electronic and phononic properties is required. In addition, this work intends to be predictive in seeking for candidates materials. These studies will thus be performed using *ab initio* computational tools, namely Density Functional Theory (DFT) and Density Functional Perturbation Theory (DFPT). Only the most basic theoretically founding principles of these techniques are recalled whenever it is required for results understanding.

Chapter 2

Phonons: density of final states

Contents

2.1	The Physics of phonons	36
2.1.1	Interatomic force constants	36
2.1.2	Equation of motion, dynamical matrix and secular equation . . .	37
2.1.3	Phonon dispersion and one-phonon density of states	38
2.2	Phonon decay	39
2.2.1	Conservation rules	39
2.2.2	Decay channels nomenclature	39
2.2.3	Engineering phonon band structure for hot-carrier solar cells . .	40
2.2.4	Need for a complete picture	41
2.3	Phonons within Density Functional Perturbation Theory . . .	42
2.3.1	Principle and formalism	42
2.3.2	Successes and limitations	44
2.4	Two-phonon final states in bulk semiconductors	45
2.4.1	Practical implementation	45
2.4.2	Detailed two-phonon states analysis	46
2.4.3	Discussion	52
2.5	Gaps in the density of states of nanostructured materials . . .	53
2.5.1	Practical implementation of PhDOS calculation on large systems	53
2.5.2	Application to superlattices	54
2.5.3	Application to quantum dots	54
2.6	Gaps in the density of states, a lost cause ?	56
2.6.1	Superlattice: how gaps are filled	56
2.6.2	Quantum dot: how gaps vanish because dots are not round . . .	57
2.6.3	How it turns out that gaps are sufficient but not necessary . . .	58
2.7	Conclusion on the two-phonon final states investigation	59

2.1 The Physics of phonons

Phonons are quanta of atomic vibration in a crystal. They are pseudo-particles, carrying a momentum \mathbf{q} and an energy $\hbar\omega$ (expressed here in cm^{-1}), ω being the vibration frequency. One of the most popular method to experimentally probe phonon band structure is neutron scattering spectroscopy: a neutron beam of known energy and momentum passing through a crystal experiences inelastic scattering with matter; after being collected, the difference in energy and momentum between the final and the initial neutrons gives access to the exchanged quanta of these two quantities within the crystal, hence the phonon energy $\hbar\omega$ versus \mathbf{q} dispersion relation.

It is very convenient to picture a crystal at the atomic scale as a set of nuclei bounded together by springs, on an infinite range. In practice, the springs stiffness is an exponentially decreasing function of the interatomic distance, and is negligible beyond few angstroms [96]. In this section, we will show that the knowledge of the springs stiffness, named *interatomic force constants* within solid state physics, is the essential element to compute the phonon dispersion relation.

2.1.1 Interatomic force constants

We denote \mathbf{R}_I^0 , the nucleus equilibrium position of the unique atom I in the crystal. Its uniqueness is ensured by introducing a cell label l , so that $\mathbf{R}_I^0 = \mathbf{R}_l + \boldsymbol{\tau}_I$, the first term being the position of the cell within the crystal, the second the position of I within the cell. If moved away from its lower-energy position by \mathbf{u}_I^l , the new position \mathbf{R}_I writes:

$$\mathbf{R}_I = \mathbf{R}_l + \boldsymbol{\tau}_I + \mathbf{u}_I^l \quad (2.1)$$

Expanding the total energy upon atomic displacements \mathbf{u} around the equilibrium positions leads to:

$$\begin{aligned} E_{tot}(\{\mathbf{u}_I^l\}) &= E_{tot}^{(0)} \\ &+ \frac{1}{1!} \sum_{l,I,\alpha} \frac{\partial E_{tot}}{\partial u_{I,\alpha}^l} u_{I,\alpha}^l \\ &+ \frac{1}{2!} \sum_{l',I,J,\alpha\beta} \frac{\partial^2 E_{tot}}{\partial u_{I,\alpha}^l \partial u_{J,\beta}^{l'}} u_{I,\alpha}^l u_{J,\beta}^{l'} \\ &+ \frac{1}{3!} \sum_{l''',I,J,K,\alpha\beta\gamma} \frac{\partial^3 E_{tot}}{\partial u_{I,\alpha}^l \partial u_{J,\beta}^{l'} \partial u_{K,\gamma}^{l''}} u_{I,\alpha}^l u_{J,\beta}^{l'} u_{K,\gamma}^{l''} + \dots \end{aligned} \quad (2.2)$$

with I, J, K labeling the atoms in the unit cells, $l, l',$ and l'' the ones they belong to, and α, β and γ the cartesian axes along which they are displaced. The first term in the above equation simply fixes the origin of the energies, and can be set to zero. So must be the second term: as a simple derivative of the energy upon displacement, it corresponds to a spring restoring force, whose sum over all atoms is zero *at equilibrium*. In this chapter,

we limit ourselves to the *harmonic approximation*, truncating the development at the first non-zero term, the second derivative (i.e. the third term in the total expansion). We define the $3N_{at} \times 3N_{at}$ interatomic force constants (IFC) matrix as:

$$C_{I,\alpha;J,\beta}(l,l') := \frac{\partial^2 E_{tot}}{\partial u_{I,\alpha}^l \partial u_{J,\beta}^{l'}} \quad (2.3)$$

$$= C_{I,\alpha;J,\beta}(l,l') \quad (2.4)$$

Within a ball-and-spring picture, $C_{I,\alpha;J,\beta}(l,l')$ corresponds to the stiffness of the spring acting on atom I in the cell l along the α axis when atom J in the cell l' is moved from equilibrium along the β axis. Within this definition we can rewrite the harmonic term of equation (2.2) as:

$$E_{tot}^{(2)}(\{\mathbf{u}_I^l\}) = \frac{1}{2!} \sum_{l',IJ,\alpha\beta} C_{I,\alpha;J,\beta}(l,l') u_{I,\alpha}^l u_{J,\beta}^{l'} \quad (2.5)$$

2.1.2 Equation of motion, dynamical matrix and secular equation

Using Newton's second law and Hooke's law, we can write the equation of motion for the atom (I,l) along the direction α :

$$M_I \ddot{u}_{I,\alpha}^l = - \sum_{J,\beta,l'} C_{I,\alpha;J,\beta}(l,l') u_{J,\beta}^{l'} \quad (2.6)$$

with M_I the mass of atom I . Because of the translational invariance of the crystal at the cell scale, no cell index is required on u , and the IFC matrix elements dependence on the cell labels l and l' can be gathered into the sole $\mathbf{R}^l - \mathbf{R}^{l'}$ difference, so that l can be set to 0, and $C_{I,\alpha;J,\beta}(l,l') \equiv C_{I,\alpha;J,\beta}(0,l')$. The solution should have an oscillatory form such as:

$$u_{I,\alpha}(t) = \frac{u_{I,\alpha}^{(0)} e^{i\omega t}}{\sqrt{M_I}} \quad (2.7)$$

that, by inserting it in equation (2.6), leads to the homogeneous system of unknown amplitudes $u_{J,\beta}^{(0)}$:

$$\sum_{J,\beta} \left[\frac{C_{I,\alpha;J,\beta}(0,l')}{\sqrt{M_I M_J}} - \omega^2 \delta_{IJ} \delta_{\alpha\beta} \right] u_{J,\beta}^{(0)} e^{i\omega t} = 0 \quad (2.8)$$

We introduce the definition of the dynamical matrix defined, at a particular \mathbf{q} -vector, as:

$$D_{I,\alpha;J,\beta}(\mathbf{q}) := \sum_{l'} e^{-i\mathbf{q}\cdot\mathbf{R}^{l'}} \frac{C_{I,\alpha;J,\beta}(0,l')}{\sqrt{M_I M_J}} \quad (2.9)$$

$$= \frac{1}{N} \frac{1}{\sqrt{M_I M_J}} \frac{\partial^2 E}{\partial u_I^{\alpha*}(\mathbf{q}) \partial u_J^\beta(\mathbf{q})} \quad (2.10)$$

with N being the number of unit cells in the crystal. Equation (E.1) becomes:

$$\sum_{J,\beta} \left[D_{I,\alpha;J,\beta}(\mathbf{q}) - \omega(\mathbf{q})^2 \delta_{IJ} \delta_{\alpha\beta} \right] u_{J,\beta}^{(0)} = 0 \quad (2.11)$$

which has non trivial solutions ($u_{J,\beta}^{(0)} \neq 0$) only if the determinant is zero:

$$\text{Det} \left[D_{I,\alpha;J,\beta}(\mathbf{q}) - \omega(\mathbf{q})^2 \mathbf{Id} \right] = 0 \quad (2.12)$$

In a 3-dimensional crystal, there are $3 \times N_{at}$ solutions for each \mathbf{q} , called *modes*, that will be labelled with the letter s . It is worth noting that the knowledge of the IFC matrix, the force constants in real space, allows to calculate the frequencies and atomic displacements for any reciprocal vector \mathbf{q} , without breaking the crystal symmetry [97].

2.1.3 Phonon dispersion and one-phonon density of states

The allowed frequency ω is a function of a three-dimensional \mathbf{q} wavevector. The *one-phonon density of states*, hereafter referred to simply as *phonon density of states* when no confusion is possible, is defined as:

$$g(\omega_0) = \frac{N\Omega}{8\pi^3} \sum_{\mathbf{q},s} \delta(\omega_0 - \omega^s(\mathbf{q})) \quad (2.13)$$

where $N_0\Omega$ is the volume of the entire crystal. It describes the number of states in each infinitely small energy interval at each energy, and its integration over the entire energy spectrum gives $3 \times N_{at}$ [98]. As an example, the calculated phonon dispersion relation and corresponding one-phonon density of states of Silicon is depicted in figure 2.1. The

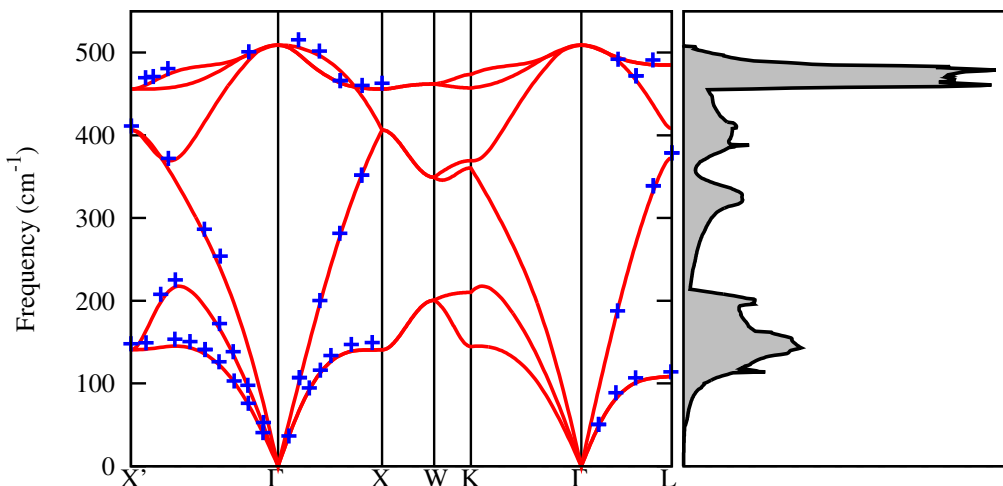


Figure 2.1: Left: Calculated (red) versus experimental (blue, reproduced from [99]) phonon dispersion relation of bulk Si. Right: Calculated one-phonon density of states. The computation methodology is given in section 2.3

phonon branches are usually named after the corresponding atomic displacement in the short wavevector limit. The three lowest ones are called *acoustic* (A), and correspond to vibrations of the cells while the atoms are fixed. All the others are called *optic* (O), and are related to atomic displacement within the cells. Among these two sorts, phonons are said to be *longitudinal* (LA, LO) or *transverse* (TA, TO) depending on whether the displacements are, respectively, parallel or perpendicular to the wavevector.

2.2 Phonon decay

As recalled in section (1.2), we focus here on the interaction between a hot electron and a nearly-zone-centre longitudinal-optic-phonon (hereafter simply called "LO"): below the intervalley transition regime, and because it is responsible for the generation of a static electric field, the LO phonon is most likely to couple with a hot electron [100]. This phonon is not stable in time compared to lower energy phonons [101], and decays, within few picoseconds at most in the known semiconductors, into lower energy phonons [102, 49, 103].

2.2.1 Conservation rules

We limit ourselves to the first order of decay, a three-phonon process, i.e. one phonon ($\omega_{\mathbf{q}_1}^{s_1}$) decaying into two other phonons ($\omega_{\mathbf{q}_2}^{s_2}$ and $\omega_{\mathbf{q}_3}^{s_3}$). This approximation has so far been always sufficient to explain and quantitatively reproduce related experimental results [104, 105, 106]. This decay is governed by the energy and momentum conservation rules:

$$\mathbf{q}_2 + \mathbf{q}_3 = \mathbf{q}_1 \quad (2.14)$$

$$\hbar\omega_{\mathbf{q}_2}^{s_2} + \hbar\omega_{\mathbf{q}_3}^{s_3} = \hbar\omega_{\mathbf{q}_1}^{s_1} \quad (2.15)$$

where "2" and "3" label the two final phonons. As we focus on the LO-phonon decay, we have $\mathbf{q}_1 \equiv \mathbf{q}_{LO}$ and $\omega_{\mathbf{q}_1}^{s_1} \equiv \omega_{LO}$. We denote here a *two-phonon final state* (or simply a *final state* when no confusion is possible) a couple of phonons $\{\omega_{\mathbf{q}_2}^{s_2}, \omega_{\mathbf{q}_3}^{s_3}\}$ that satisfies the energy and momentum conservation rules.

2.2.2 Decay channels nomenclature

The final states in the cubic phase are divided into four subspaces for the upcoming analysis: those that involve two LA-phonons will be referred to as the *first Klemens states* [43], and similarly, when they involve one LA and one TA-phonon, they will be referred to as the *second* and *third Klemens states*, one for each TA mode. The cases where the two resulting phonons are one TO and one acoustic (either LA or TA), are labelled the *Ridley states* [88]; making the distinction between the different Ridley surfaces (TOs+LA/TAs) does not bring here any supplementary information. An illustration of this labeling is displayed in figure 2.2, for all two-phonon states fulfilling the conservation rules (2.14) and (2.15) in *GaAs*, along high symmetry directions in the first Brillouin zone.

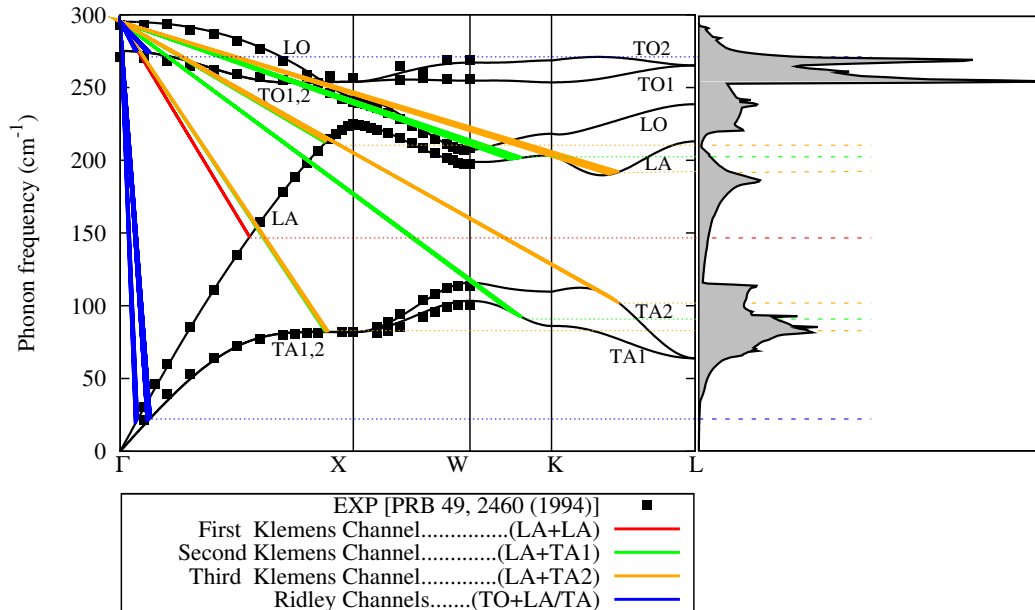


Figure 2.2: Zone-centre LO phonon decay in bulk GaAs. The colored solid lines are visual guides linking the initial LO-phonon at the Brillouin zone centre (top left node) to the possible two-final phonons. The experimental data (black filled squares) are reproduced from [107].

2.2.3 Engineering phonon band structure for hot-carrier solar cells

From a quantum mechanical point of view, the fewer the final states are, the less probable the decay is, and thus the greater is the LO-phonon lifetime. Hence, the first basic idea in phonon engineering for hot-carrier solar cells is to find or design an absorbing material that exhibits few allowed two-phonon final states. The idea of using the gap formation in the density of states may come from an indirect reading of a paper from B. K. Ridley [88], in which he noticed that the gap between the optic and acoustic branches in bulk *GaP* is too large to allow LO-phonon decay through Klemens channels, and that other channels have to be considered (as it happened, the *Ridley channels*).

In a first approach, with a one-dimensional ball-and-spring model [102], it appears that the mass ratio between the atoms is a key parameter. As an example, the phonon band structure was calculated for a one-dimensional $(GaSb)_{NL}-(AlSb)_{NL}$ superlattice, together with bulk *GaSb* and *AlSb* cases, within the approximation of nearest neighbour-only interaction, where NL is the number of layers of each binary, the whole structure having periodic boundary conditions (figure 2.3). In the bulk cases to start with, the gap opening between the acoustic and the optic region is solely determined by the atomic mass ratio: at the zone boundary, the acoustic and optic frequencies are respectively given by $\omega_O = \sqrt{\frac{2C}{m}}$ and $\omega_A = \sqrt{\frac{2C}{M}}$, m and M being the mass of the lightest and heaviest atom, C the stiffness of the interatomic springs, that are assumed atomic species-independent. Hence, the opening is simply $\frac{\omega_O}{\omega_A} = \sqrt{\frac{M}{m}}$. Considering the superlattice, forbidden energy ranges

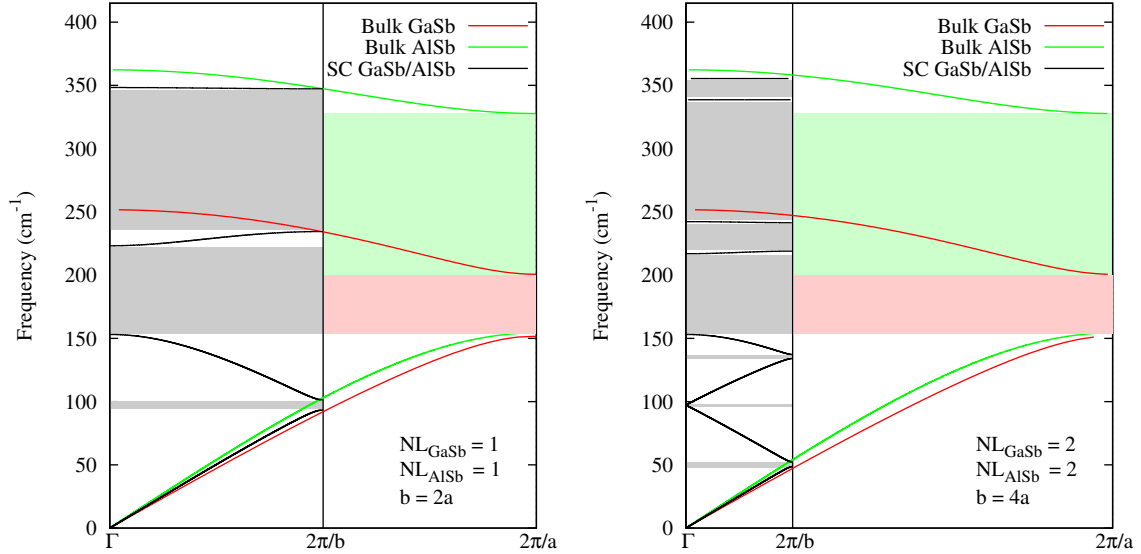


Figure 2.3: Band folding and mini-gaps formation in one-dimensional $(GaSb)_{NL} - (AlSb)_{NL}$ superlattice, NL being the number of layers of each compound. The lattice parameters of $GaSb$ and $AlSb$ are considered to be identical, and equal to a , so that the superlattice one is $b = 2aNL$. The shaded areas highlight the forbidden energy range for bulk $GaSb$ (red), bulk $AlSb$ (green), and the superlattice (grey).

appear in the equivalent bulk acoustic regions (grey shaded areas), whose number and extent depend on NL . As it turns out, the size of the gaps decreases as an inverse function of the superlattice size (as found elsewhere in [96]). However, the size and position of the gaps can be tuned, depending on the periodic arrangement of the layers. Hence, nanostructuring allows creating gaps in the acoustic region that seems to make Klemens decay prevention possible. From a hot-carrier solar cell point of view, this has been the motivation for seeking large phononic gaps in both simple bulk semiconductors [80, 87] superlattices and quantum dots [108, 83, 109].

2.2.4 Need for a complete picture

At this point, we need a tool to compute the phonon dispersion relation with an arbitrary precision and an excellent accordance with experiment. The band structure and gap formation in figure 2.3 were calculated within a first-neighbour ball-and-spring approach, a toy model, that is not satisfactory for accurate phonon engineering, since only a rough accordance with experimental dispersion can be expected. In addition, it does not take into account the three degrees of freedom of a real crystal, that may change the band dispersion and thus the gaps width.

As seen in section (2.1), the key parameter for calculating phonon band structure is the interatomic force constant matrix. Empirical methods exist to calculate long range interatomic interactions, within which the matrix elements are parametrised and adjusted to reproduce some experimental values, such as the sound velocity or the Raman peak

position. A review of the most common parametrisation methods can be found in [100]. However the transferability of the fitted parameters for two materials A and B for computing the band structure of any A_xB_y material is questionable, not to mention that, most of the time, they do not allow to include the long range polar interaction responsible for LO-TO splitting [26] (see section (2.3.1.2)).

For these reasons, the Density Functional Perturbation Theory (*DFPT*), an *ab initio* method, is chosen to compute the interatomic force constant matrix, preventing us from any *ad hoc* assumption on the band structure and dependence on existing experimental data for the materials of interest.

2.3 Phonons within Density Functional Perturbation Theory

The *ab initio* calculation of phonon properties is one of the brightest successes of computational condensed matter physics, as it provides a predictive tool, for instance, to perform Raman spectra analysis, or to search for new materials according to specific parameters, such as the lattice thermal conductivity in the field of thermoelectricity. In this section are recalled the essential ideas and equations required for an overall understanding of the manuscript, leaving the exhaustive derivation to specialised litterature [97, 110].

2.3.1 Principle and formalism

We focus here on the computation of the interatomic force constant (IFC) matrix in real space (equation (2.4)) using the ground state electronic density as the basic ingredient.

2.3.1.1 Generalized forces and IFC as an electronic density functional

Within the Born-Oppenheimer approximation, the Hamiltonian of N electrons in the field of fixed nuclei with coordinates $\{\mathbf{R}\}$ is [110]:

$$H = H^{el} + H^N + H^{e-N} \quad (2.16)$$

$$H^{el} = T_i + E_i^C \quad (2.17)$$

$$= \sum_i \frac{-\hbar^2}{2m_i} \frac{\partial^2}{\partial \mathbf{r}_i^2} + \frac{e^2}{2} \sum_{i \neq j} \frac{1}{|\mathbf{r}_i - \mathbf{r}_j|} \quad (2.18)$$

$$H^N = T_N + E_N^C(\{\mathbf{R}\}) \quad (2.19)$$

$$= \sum_I \frac{-\hbar^2}{2m_I} \frac{\partial^2}{\partial \mathbf{R}_I^2} + \frac{e^2}{2} \sum_{I \neq J} \frac{Z_I Z_J}{|\mathbf{R}_I - \mathbf{R}_J|} \quad (2.20)$$

$$H^{e-N} = \sum_{I \neq J} \frac{-Z_I e^2}{|\mathbf{r}_i - \mathbf{R}_I|} \equiv \sum_{i,I} \partial v_I(\mathbf{r}_i - \mathbf{R}_I) \quad (2.21)$$

where $H^{el/N}$ is the sum of the electronic/nucleus kinetic energy and Coulombic interaction between the electrons/nuclei, and H^{e-N} is the total electron-phonon interaction. The

capital letters refer to nuclei, the small ones to the electrons; \mathbf{r}_i is the position of the electron i , e is the elementary electronic charge, Z_I the charge of nucleus I .

The equilibrium state of the crystal is reached when the sum of all the forces acting on every nucleus is zero. We thus define the generalised expression of the force \mathbf{F} as the partial derivative of the Hamiltonian with respect to R_α^I :

$$\mathbf{F}_I \equiv -\frac{\partial E(\{\mathbf{R}\})}{\partial \mathbf{R}_I} = \left\langle \Psi_{\{\mathbf{R}\}} \left| \frac{\partial H_{\{\mathbf{R}\}}}{\partial \mathbf{R}_I} \right| \Psi_{\{\mathbf{R}\}} \right\rangle \quad (2.22)$$

where Ψ is the *ground state* wavefunction of the system *in the nuclear configuration* $\{\mathbf{R}\}$. The electronic charge density in this set is:

$$n(\mathbf{r}) = N \int \left| \Psi_{\{\mathbf{R}\}}(\mathbf{r}, \mathbf{r}_2, \dots, \mathbf{r}_N) \right| d\mathbf{r}_2 \dots d\mathbf{r}_N \quad (2.23)$$

and making use of the Hellmann-Feynman theorem [111, 112], equation (2.22) now reads:

$$\mathbf{F}_I = - \int n(\mathbf{r}) \frac{\partial v_I(\mathbf{r} - \mathbf{R}_I)}{\partial \mathbf{R}_I} d\mathbf{r} - \frac{\partial E_N(\{\mathbf{R}\})}{\partial \mathbf{R}_I} \quad (2.24)$$

From here to the interatomic force constants remains only one single derivation step. Evaluating terms of equation (2.24) is achievable within different models and approximations [97], either *ab initio*, empirical or semi-empirical. The adopted method here the Density Functional Theory (*DFT*), as briefly recalled in appendix A, within which we can rewrite the generalised force expression:

$$\mathbf{F}_I^{DFT} = - \int n(\mathbf{r}) \frac{\partial V_{\{\mathbf{R}\}}(\mathbf{r})}{\partial \mathbf{R}_I} d\mathbf{r} - \frac{\partial E_N(\{\mathbf{R}\})}{\partial \mathbf{R}_I} - \frac{\delta E(\{\mathbf{R}\})}{\delta n(\mathbf{r})} \frac{\partial n(\mathbf{r})}{\partial \mathbf{R}_I} \quad (2.25)$$

(where $V_{\{\mathbf{R}\}} \equiv \sum_I v_I(\mathbf{r} - \mathbf{R}_I)$). Because the system total energy is extremal for the ground state density, when all atoms are in their equilibrium positions, the last term vanishes and the latter equation matches exactly the generalised force expression (equation (2.24)). Differentiating \mathbf{F}_I^{DFT} with respect to nuclear coordinates leads to the interatomic force constant expression within DFPT:

$$\frac{\partial^2 E(\{\mathbf{R}\})}{\partial \mathbf{R}_I \partial \mathbf{R}_J} = \int \frac{\partial n(\mathbf{r})}{\partial \mathbf{R}_J} \frac{\partial V_{\{\mathbf{R}\}}(\mathbf{r})}{\partial \mathbf{R}_I} d\mathbf{r} + \delta_{I,J} \int n(\mathbf{r}) \frac{\partial^2 V_{\{\mathbf{R}\}}(\mathbf{r})}{\partial \mathbf{R}_I \partial \mathbf{R}_J} d\mathbf{r} + \frac{\partial^2 E_N(\{\mathbf{R}\})}{\partial \mathbf{R}_I \partial \mathbf{R}_J} \quad (2.26)$$

and we end up with what was required in equation (2.10) to compute the dynamical matrix $D_{I,\alpha;J,\beta}(\mathbf{q})$. Defining $\tilde{C}_{J,\beta}^{I,\alpha}(\mathbf{q}) := \sqrt{M_I M_J} \times D_{I,\alpha;J,\beta}(\mathbf{q})$, the *reciprocal space interatomic force constant matrix*, we can write $\tilde{C}_{I,\alpha;J,\beta}$ as the sum of two terms:

$$\tilde{C}_{J,\beta}^{I,\alpha} = {}^{el} \tilde{C}_{J,\beta}^{I,\alpha} + {}^{ion} \tilde{C}_{J,\beta}^{I,\alpha} \quad (2.27)$$

where the second term in the right hand side is an ionic contribution that does not depend on the density (the last term in equation (2.26)). The electronic contribution ${}^{el}\tilde{C}_{J,\beta}^{I,\alpha}$ writes:

$${}^{el}\tilde{C}_{J,\beta}^{I,\alpha} = \frac{1}{N} \left[\int \left(\frac{\partial n(\mathbf{r})}{\partial u_I^\alpha(\mathbf{q})} \right)^* \frac{\partial V_{\{\mathbf{R}\}}(\mathbf{r})}{\partial u_J^\beta(\mathbf{q})} d\mathbf{r} + \delta_{I,J} \int n(r) \frac{\partial^2 V_{\{\mathbf{R}\}}(\mathbf{r})}{\partial u_I^{*\alpha}(\mathbf{q}=\mathbf{0}) \partial u_J^\beta(\mathbf{q}=\mathbf{0})} dr \right] \quad (2.28)$$

Hence, the second derivative of the energy depends *solely* on the linear response to the lattice distortion of the electronic charge density ($\partial n/\partial u$). This is a particular case of the so-called $(2n+1)$ theorem [113], stating that the knowledge of the density response to the n^{th} order gives access to the energy response up to the $(2n+1)^{\text{th}}$ order. The interatomic force constants in reciprocal space can then be Fourier-transformed back to real space, so that the $\omega(\mathbf{q})$ relation can be computed at any \mathbf{q} vector.

2.3.1.2 The LO-TO splitting

In polar materials, the long wavelength vibrations of oppositely charged atoms are responsible for a macroscopic electric field [26]. In addition to the only remaining term in equation (2.2) up to the second order at equilibrium, one has to include this electric field \mathbf{E} contribution to the total energy. It can be divided into two terms, an electronic one and an ionic one, so that the new total energy writes [99]:

$$E(\{\mathbf{u}\}, \mathbf{E}) = \frac{1}{2} \sum_{IJ} \sum_{\alpha\beta} \mathbf{u}_I \cdot {}^{an}\tilde{C}_{IJ} \cdot \mathbf{u}_J - \frac{\Omega}{8\pi} \mathbf{E} \cdot \boldsymbol{\epsilon}_\infty \cdot \mathbf{E} - e \sum_I \mathbf{u}_I \cdot \mathbf{Z}_I^* \cdot \mathbf{E} \quad (2.29)$$

where the label an was added onto the dynamical matrix to highlight its analytical feature, $\boldsymbol{\epsilon}_\infty$ is the dielectric tensor, and \mathbf{Z}_s^* the Born effective charge carried by the atom I . To the analytical term ${}^{an}\tilde{C}$ has then to be added the system response to the perturbation it creates itself, a non-analytical term ${}^{na}\tilde{C}$, that writes:

$${}^{na}\tilde{C}_{J,\beta}^{I,\alpha} = \frac{4\pi e^2}{\Omega} \frac{(\mathbf{q} \cdot \mathbf{Z}_I^*)_\alpha (\mathbf{q} \cdot \mathbf{Z}_J^*)_\beta}{\mathbf{q} \cdot \boldsymbol{\epsilon}_\infty \cdot \mathbf{q}} \quad (2.30)$$

This coupling between the lattice vibrations and the polarisation is responsible for the so-called *LO-TO splitting* in polar semiconductors. Although we will develop this point later in chapter 4, it is already worth noting that this "correction" is not only effective at the very vicinity of the zone-centre, and, strictly speaking, not only for the LO mode, as can be seen in figure 2.4.

2.3.2 Successes and limitations

DFPT as implemented in the Quantum Espresso package [97, 6] has been used for this thesis. It has been worldwide recognised as an extremely efficient tool in the comprehension of a significant number of vibrational related properties, among which, study of soft modes and pressure induced phase transitions [115]; phonons in superlattices [116],

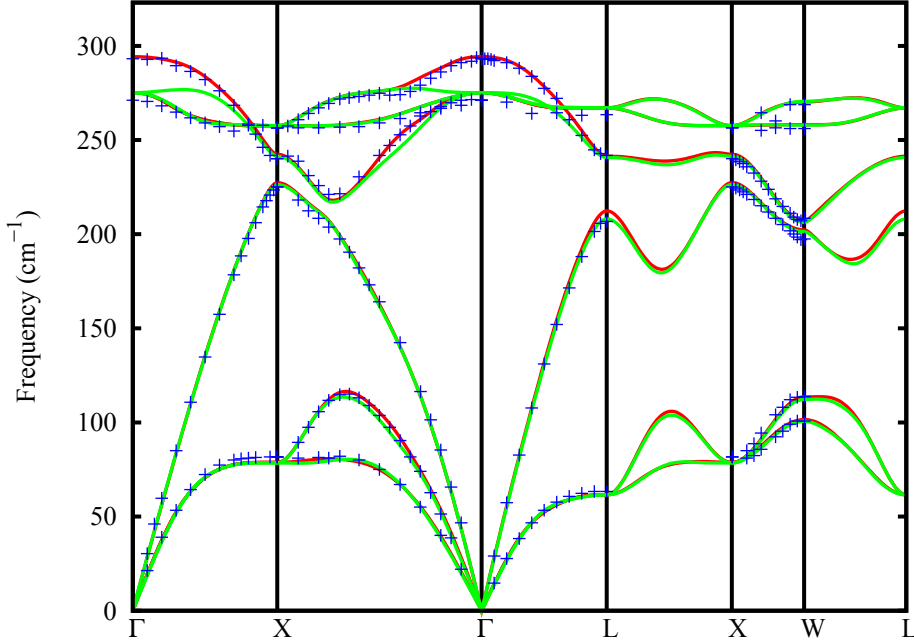


Figure 2.4: Phonon dispersion relation of bulk GaAs with (red) and without (green) taking into account the coupling between electric field at atomic vibration. Experimental data (blue points) are reproduced from [114].

alloys [117], and nanostructures such as Graphene [118] and Fullerene [119]; defects vibrational properties [120]; surface modes [121]; thermodynamics properties of solids within the quasi-harmonic approximation [122]; Raman tensor analysis [123]; and phonon lifetime in semiconductors [104, 124].

Unfortunately, the required computational effort scales as N_{at}^α , $\alpha \sim 3 - 4$, which limits the affordable system size to ~ 100 atoms [97]. This corresponds for instance to a $1.3 \times 1.3 \times 1.3 \text{ nm}^3$ Silicon FCC cubic cell, or a $1.6 \times 1.6 \text{ nm}^2$ Graphene sheet.

2.4 Two-phonon final states in bulk semiconductors

In this section, we use the phonon band structure of different bulk materials computed within DFPT, and apply the energy and momentum conservation rules, equations (2.14) and (2.15), for an initial LO-phonon emitted in the intraband electron cooling process. We then investigate the phonon criteria defined in section (1.4.2).

2.4.1 Practical implementation

Below are given practical details on the implementation of the conservation rules (2.14) and (2.15) for any material in the entire first Brillouin zone. Additional computational details can be found in appendix B.

2.4.1.1 The zone centre approximation

Since the exchange wavevector in the electronic cooling process is small compared to the Brillouin zone size [21], a very common [43, 125, 104, 126, 84, 127] and convenient approximation is to set \mathbf{q}_{LO} to $\mathbf{0}$ in equation (2.14), so that the conservation rules now write:

$$\mathbf{q}_2 = -\mathbf{q}_3 \quad (2.31)$$

$$\hbar\omega_{\mathbf{q}_2}^{s'} + \hbar\omega_{\mathbf{q}_3}^{s''} = \hbar\omega^{LO} \quad (2.32)$$

Since phonon eigenvalues have the inversion property $\omega(\mathbf{q}) = \omega(-\mathbf{q})$, within this approximation the two conservation rules reduce only to (2.32).

2.4.1.2 Searching algorithm

The equality (2.32) cannot be exactly solved numerically. A tolerance delta function has to be added on the right-hand side of the equation:

$$\hbar\omega_{\mathbf{q}_2}^{s'} + \hbar\omega_{\mathbf{q}_3}^{s''} = \hbar\omega^{LO} \pm \Delta \quad (2.33)$$

The dispersion relation is computed on a very tight mesh into the whole irreducible Brillouin zone (1/48th of the whole BZ for a bulk FCC crystal, see figure 2.5), so that the volume of each \mathbf{q} -point is $0.125 \cdot 10^{-6}$ in unit of $(\frac{2\pi}{a})^3$, a being the lattice parameter. This is equivalent to mesh the ΓX axis in the reciprocal space into 200 \mathbf{q} -points. In this chapter, because we simply seek for a visual representation of the allowed two-phonon final states, Δ is taken as a rectangular function. E. Haro-Poniatowski and co-workers [125] chose a width of 1% of the optic phonon frequency. Considering the density of the mesh and the reached agreement with experiment (see for instance figure 2.4), we chose 0.1%, so that the density of final states in \mathbf{q} -space is sparse enough to allow a readable analysis. An example is shown in figure 2.2, where this methodology was applied on GaAs along a particular path in the BZ (the negative \mathbf{q} region is folded onto the positive one for clarity).

2.4.2 Detailed two-phonon states analysis

We investigate the two-phonon final states as defined in section (2.2.2), within the framework of phonon criteria for hot-carrier solar cells as defined in (1.4.2), first on a wide range of bulk semiconductors in the Zinc-Blende phase. The results in reciprocal space are displayed in figure 2.6 for the III-V group, and figure 2.7 for the IV-IV: they are the equivalent three-dimensional picture of figure 2.2.

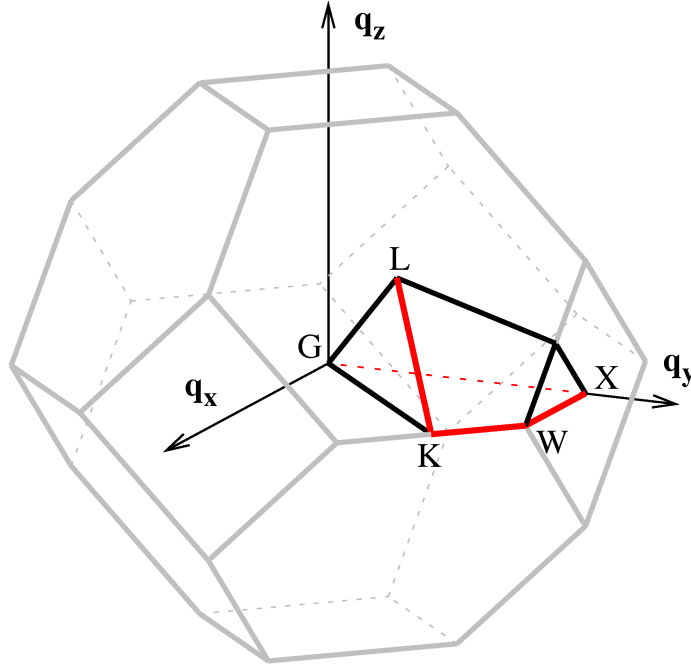


Figure 2.5: Full (grey) and irreducible (black) FCC Brillouin zone. The red broken line corresponds to the \mathbf{q} -path along which the band structure was plotted in figure (2.2).

2.4.2.1 Bulk III-V group

GaAs is a case state since it has been the most studied semiconductor of the III-V group, both experimentally and theoretically [114, 125, 104, 49]. In addition to the Ridley channels, the three different Klemens channels are allowed. The different channels contribution, gathered in table 2.1, is in contradiction with some previous studies [49, 136]. Indeed, F. Vallée and F. Bogani [136] claimed that the LO-phonon decay in GaAs is led by another two-phonon process, involving one LO-phonon near the L point of the Brillouin zone and one LA-phonon. This channel does not appear in our results for the chosen energy conservation function width of 0.1%. Trying to relax this latter parameter, we find that at 7%, a similar channel appears, but involving a zone edge LO-phonon near the K -point of the Brillouin zone. The Vallée-Bogani channel, as it is described above, only appears at 7.2%. In both cases, the tolerance parameter is too large to seem reasonable for the author: in a phonon lifetime calculation (see section (3.4.2)), the Gaussian linewidth in the energy conservation relation is taken at most for simple semiconductors to be 5 cm^{-1} [49, 137, 106, 124], which, for the above channel, gives a Gaussian weight of $5 \cdot 10^{-2}$ (instead of 1 in a perfectly energy conservation situation). This channel thus cannot possibly be the leading one, and is considered not to take place within the current approximations. This conclusion is consistent with recent full-band Boltzmann transport equation solving via Monte Carlo simulation [127].

When increasing the atomic mass ratio, the second and third Klemens surfaces disappear,

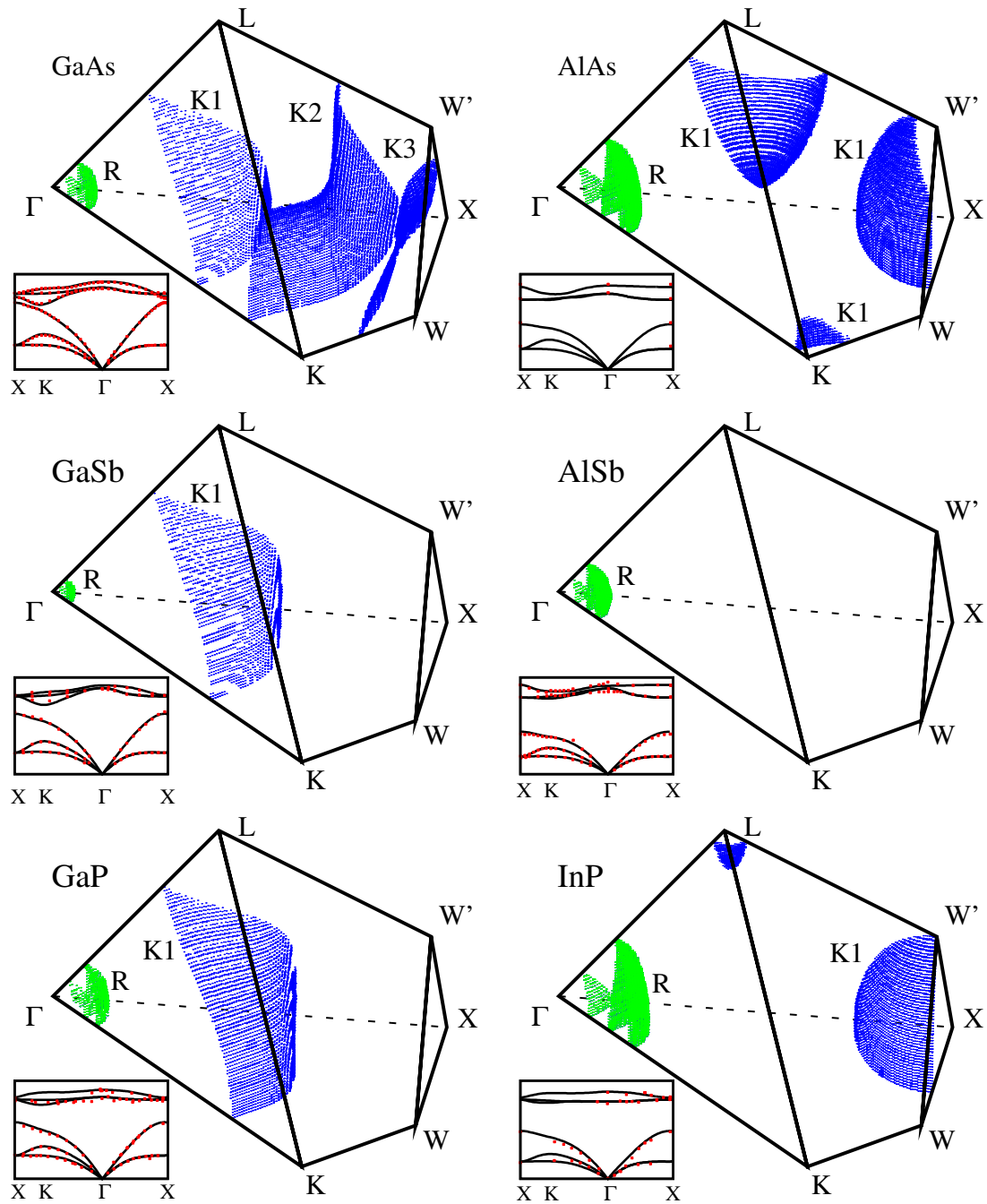


Figure 2.6: Two-phonon final states in the zone-centre approximation for III-V semiconductors. The blue surfaces are Klemens states (K1, K2 and K3 for first, second and third Klemens states), the green ones are Ridley states (R). The insets show the accordance between computed dispersion relation and experimental data on high symmetry lines([114, 107, 128, 129, 130, 131, 132, 133, 134]).

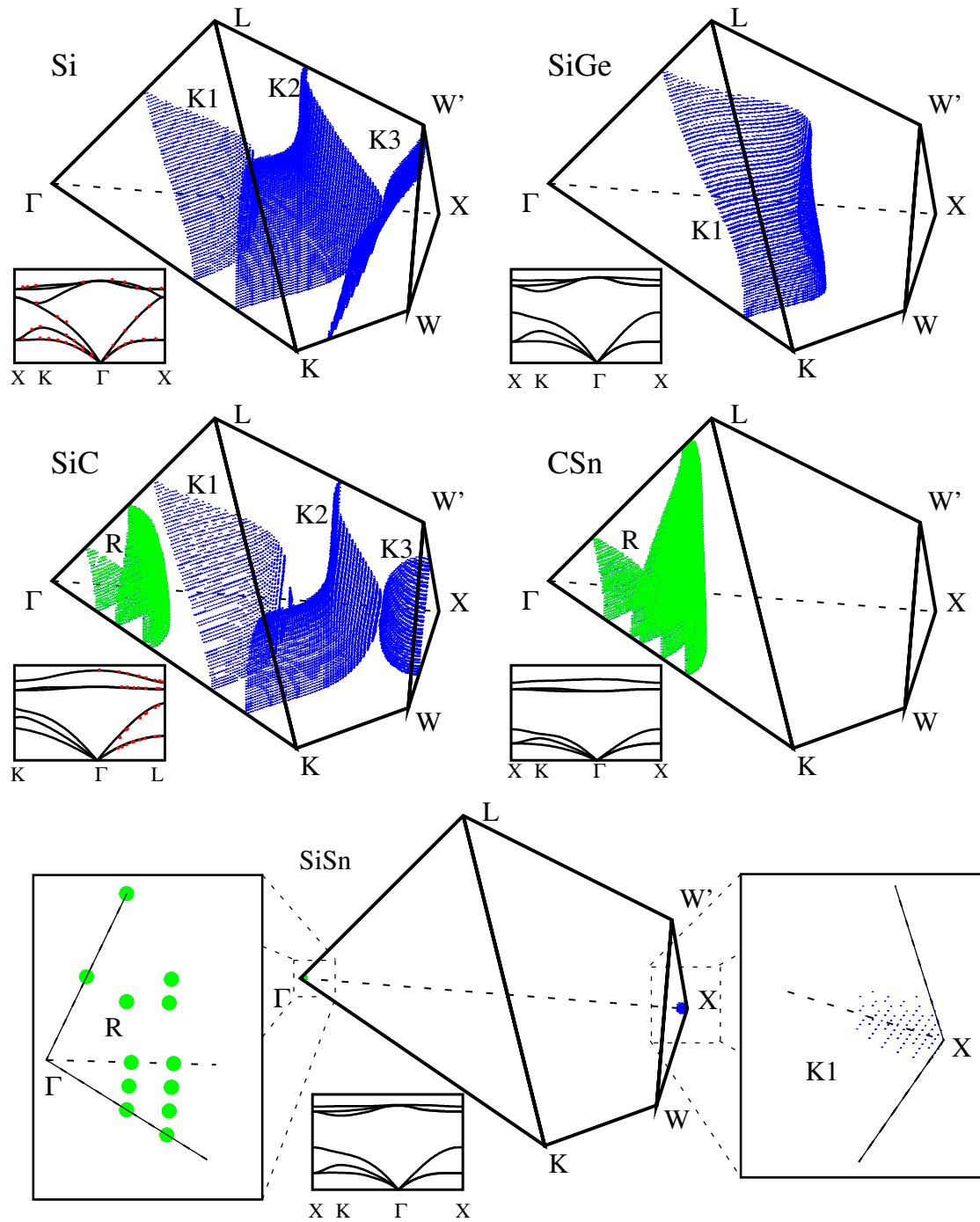


Figure 2.7: Two-phonon final states in the zone-centre approximation for group IV semiconductors. The blue surfaces are Klemens states (K1, K2 and K3 for first, second and third Klemens states), the green ones are Ridley states (R). The insets show the accordance between computed dispersion relation and experimental data whenever they exist ([99, 135]).

	Klemens channel			Ridley channel
	LA+LA	LA+TA1	LA+TA2	
GaAs	93.20			6.80
	9.73	59.23	31.04	
AlAs	67.25			32.71
	100.00	0.00	0.00	
AlSb	0.00			100.00
	0.00	0.00	0.00	
GaSb	83.78			6.22
	100.00	0.00	0.00	
GaP	74.10			25.56
	100.00	0.00	0.00	
InP	16.28			83.72
	100.00	0.00	0.00	

Table 2.1: Contribution of each channel in the two-phonon final states number (in %) in the bulk III-V semiconductors. The detailed of the Klemens states are given in % of the total Klemens channel contribution.

as in GaSb and GaP (figure 2.6). The remaining allowed channels lead to an almost spherical first Klemens surface, which is of high interest when considering creating a gap in the dispersion relation in order to prevent the phonon decay, because the gap has to remain at a constant energy in all reciprocal directions, and this can be directly associated with nanostructures such as quantum dots. The narrow splitting between LO and TO branches is also responsible in GaSb for the Ridley states to be confined very close to the Γ point. As the mass difference between the two atoms increases, the first Klemens surface is split into three parts in the vicinity of particular high symmetry points, K , L and X , as in AlAs. This behaviour is emphasized in InP, where even the first Klemens states near K are not allowed. AlSb is the ultimate case since the Klemens channels are forbidden everywhere because all acoustic branches remain below half of the LO-phonon energy. Unfortunately, AlSb has an indirect band gap, which makes it unsuitable for an absorber.

2.4.2.2 Bulk IV-IV group

The same calculation is performed for Si, SiGe, SiC, CSn and SiSn, and the two-phonon final states are depicted in figure 2.7. Si is the case state of non-polar semiconductors. The three Klemens channels are energetically allowed, and its elemental feature makes Ridley channel not relevant. As in GaAs, we can see from table 2.2 that in this case the first Klemens process is not dominant in the purely acoustic final states. It is also clear when considering the relative size of the three Klemens surfaces in figure 2.7. SiGe is another example for which the mass difference is high enough to forbid the second and third Klemens channels, leaving only possibilities for the first Klemens process. Interestingly, the first Klemens surface in SiGe differs from pure Si. This is an edge case: the first

Klemens surface is bowing in the centre, which for higher mass differences, like in AlAs, leads to the case where this surface is split into three pieces (figure 2.6). The LO and TO branches are centered so close around Γ that no Ridley channel is observed within an energy conservation function width of 0.1%. In SiC, the high electronegative feature of the Carbon atom is responsible for the large and complete LO-TO splitting, so that the gap between the LO and the TO branch is effective in the whole Brillouin zone. As a consequence, we find a large number of Ridley final states. In addition, in accordance with the fact that the mass ratio between the two atoms is between the one of GaAs and of GaP, all the Klemens channels are energetically allowed. In the CSn case, the mass ratio is close to 10, which is much larger than any of the other semiconductors treated here. In addition, the LO-TO splitting is even wider than in SiC. While no Klemens channel decay are allowed, the Ridley surfaces are numerous and stretched even farther from the Γ point than in SiC.

SiSn shows particular features that call for development. The LO and TO branches

Si	100.00			0.00
	12.12	33.94	53.94	
SiGe	100.00			0.00
	100.00	0.00	0.00	
SiC	64.47			35.53
	18.19	20.97	60.84	
CSn	0.00			100.00
	0.00	0.00	0.00	
SiSn	87.28			12.72
	100.00	0.00	0.00	

Table 2.2: Contribution of each channel in the two-phonon final states number (in %) in the IV-IV. The detailed of the Klemens states are given in % of the total Klemens channel contribution.

split just enough around Γ to open an extremely narrow energy window for the Ridley decay to occur. Due to the relatively high mass ratio of 4.23, the first Klemens surface is restricted to a small reciprocal volume in the vicinity of the X -point. In this situation, the results strongly depend on the accuracy of the calculated phonon dispersion relation. Unfortunately, no experimental data exist in the very knowledge of the author.

2.4.2.3 Questioning the zone centre approximation

The relevance of the zone centre approximation as defined in paragraph (2.4.1.1) is illustrated in figure 2.8, on which the variation of the normalised number of final states upon the initial value of the LO-phonon wavevector is depicted. Three behaviors are to be distinguished. The first one is the small increase of this number with $|\mathbf{q}_{LO}|$, and this is relevant, except for AlSb and SiSn, for all the studied semiconductors. In these cases indeed the Klemens surfaces are the leading final states, and they have to undergo

expansion when increasing $|\mathbf{q}_{LO}|$ to keep fulfilling the conservation rules. AlSb, shows the opposite trend since the number of final states decreases: as $|\mathbf{q}_{LO}|$ is enlarged, contrarily to the Klemens surfaces, the Ridley ones shrink, and since only Ridley channels are allowed in this case, this reduction of final states is not compensated by an increasing number of Klemens states. Finally, it is obvious that SiSn has an extraordinary behavior, unrivalled to any other semiconductor. A detailed study of this material will follow in chapter 3. For now, we shall just remember that the zone-centre approximation is reasonable when the final states are not confined near the Brillouin zone edges, and that SiSn is a counter example.

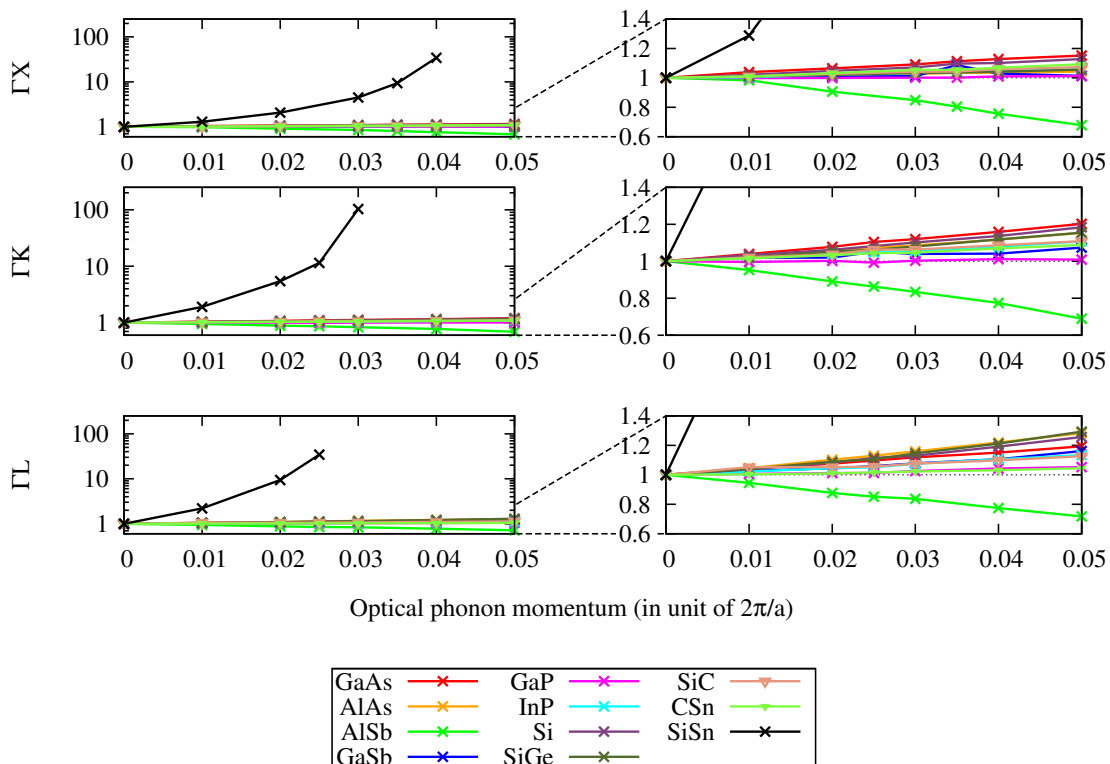


Figure 2.8: Dependence of the bare two-phonon final states number upon the wavevector $|\mathbf{q}_{LO}|$ of an initial LO-phonon belonging to ΓX , ΓK and ΓL . For an easier comparison number of final states are normalized to 1 at $|\mathbf{q}_{LO}| = \mathbf{0}$.

2.4.3 Discussion

In terms of available two-phonon final states, the presence of a wide enough gap between the acoustic and the optic branches has often been pointed out as a sufficient criterion for absorber candidate from a phononic point of view. We showed the importance to consider also the LO-TO splitting width, since it can be responsible for a large number of Ridley states (as in CSn or SiC in figure 2.7, or again InN [85, 86]), and also because it partly determines the optic phonon energy dispersion (condition (iv) in (1.4.2)). This has consequences on the choice of chemical elements for material design: the LO-TO

splitting being related to effective charges on atoms [26], it can be related to the difference of electronegativity of the atoms that form the absorber.

2.5 Gaps in the density of states of nanostructured materials

The analysis on available final states is performed in superlattices and quantum dots, as atomic scale nanostructuring was shown to open forbidden energy ranges in the band structure.

2.5.1 Practical implementation of PhDOS calculation on large systems

Due to band folding, the number of final states in superlattices is expected to be too large to perform a detailed analysis as the one done in section (2.4.2). Hence, we limit ourself to the study of the one-phonon density of states (*PhDOS*), investigating the gap formation as described for instance in [83] and [84].

The size issue

The superlattices size is chosen so to step away from quasi-bulk systems. We consider a 512-atom square box within periodic boundary conditions, in which the atoms are arranged in well or dot patterns. Computing the interatomic force constant in such a large system using DFPT is not affordable within a reasonable time (section (2.3.2)). Hence, we will limit ourselves to atomic types for which the transferability of the force constants is valid.

Transferability of the force constants

Considering equations (2.12) and (2.10), we can address the possibility of building the dynamical matrix of a material using the appropriate atomic masses and the interatomic force constants of another. If one refers to a *ball-and-spring* model, this is equivalent to consider that the springs binding the atoms together have the same stiffness in both materials. This is often referred to as the *mass approximation*. Its accuracy has been studied for III-V and IV-IV FCC materials [99], and led to the conclusion that, for III-V, it gives very satisfactory results when the materials differ by their cations, while a much poorer transferability is observed when they differ by their anions. Finally, the transferability of Si interatomic force constants to Ge is found to be relevant in the sense that the error between the band structure calculated with any of the two sets of force constants is of the same order of magnitude than the one between experimental and calculated values (see appendix E).

Choice of atomic species

We will use Si/Ge as the test case for group-IV materials. Concerning the III-V, lots of work has already been done on GaAs/AlAs superlattices [138, 139, 140, 141] using polarised Raman spectroscopy together with an elastic continuum model for interpretation, that

allowed to witness experimental evidence of few cm^{-1} band gap opening in the superlattice direction. We chose GaSb-AlSb, for it has been less investigated, and as it shows a larger atomic mass ratio than in GaAs/AlAs, enhancing *a priori* our chance to observe phonon gaps formation.

2.5.2 Application to superlattices

The phonon density of states is calculated for $Si_{16-N}Ge_N$ superlattices, N ranging from 0 (bulk *Si*) to 16 (bulk *Ge*). The results in the Silicon *acoustic region*, the region of interest, are plotted in figure 2.9. As can be seen, no gap appears in the density of states: it turns almost continuously from one bulk shape to the other. This last statement is

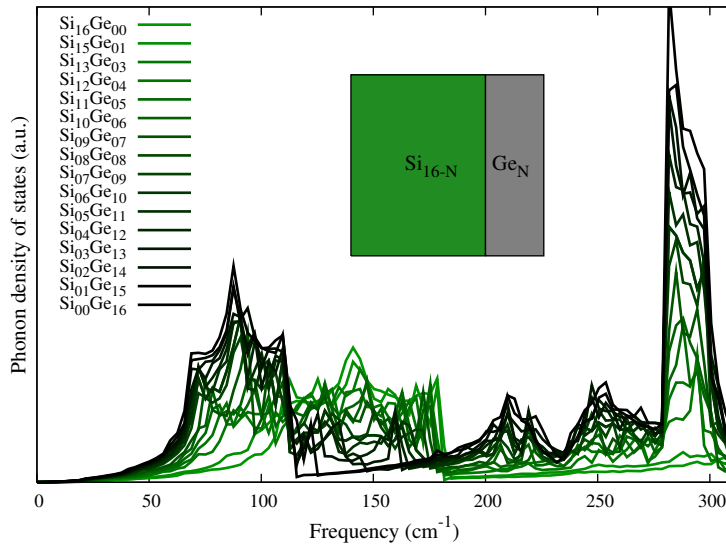


Figure 2.9: Phonon density of states of $Si_{16-N}Ge_N$ superlattices.

even more relevant for $GaSb_{8-N}AlSb_N$ superlattices (figure 2.10), as there is only a very soft change in the acoustic region. This is due to the especially strong overlap of *GaSb* and *AlSb* acoustic branches which, from a phononic point of view, does result in interferences.

2.5.3 Application to quantum dots

Figures 2.11 and 2.12 show the phonon density of states for different sized $Si(Ge)$ quantum dots embedded in a $Ge(Si)$ matrix. We cannot witness the creation of a gap in the acoustic region, even for small-sized dots. On the contrary, the comb-like structure seems to appear when increasing the size of the quantum dot. The same experiment is performed for *AlSb* (*GaSb*) dot in a *GaSb* (*AlSb*) matrix (figure 2.13 (2.14)). In the joint acoustic region we observe the same feature as for superlattices, i.e. an almost unchanging shape. In the case of the *AlSb* dot, the depopulation of the equivalent *GaSb* optic energy range is not sharp enough to create gaps. For the *GaSb* dot, the situation is the opposite. As seen in figure 2.6, *AlSb* alone has a gap wide enough to prevent all Klemens channels

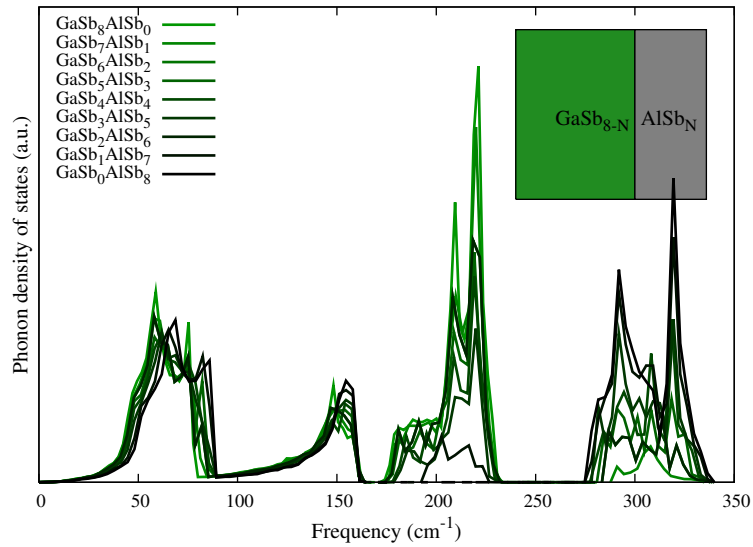


Figure 2.10: Phonon density of states of $GaSb_{8-N}AlSb_N$ superlattices.

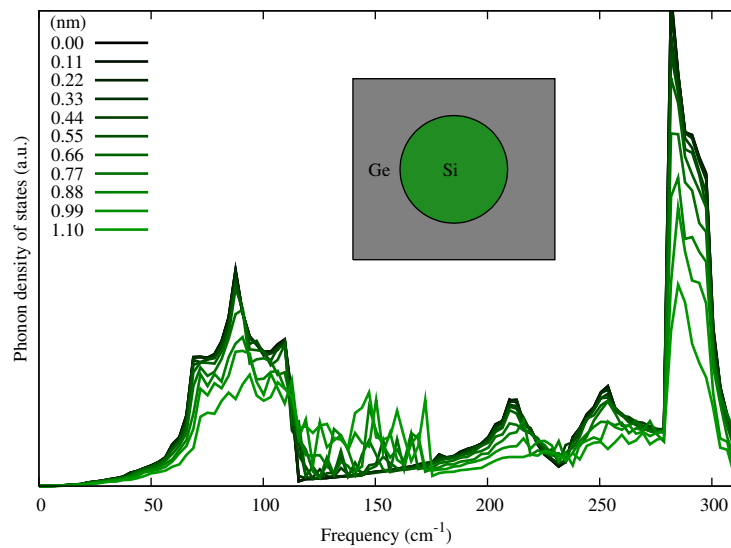


Figure 2.11: Phonon density of states of different sized Si quantum dot embedded in a Ge matrix. The legend indicates the dot radius.

from being allowed: we face the question of the possibility that a dot may or not induce intermediate states in the gap that would form new decay channels. As can be seen in figure 2.14, apart from the limit of *highly diluted defect*, the gap is filled with intra-dot modes that can couple with the quasi-LA region modes to energetically allow LO-phonon decay. However, the *effective weight* of these channels is still an open question.

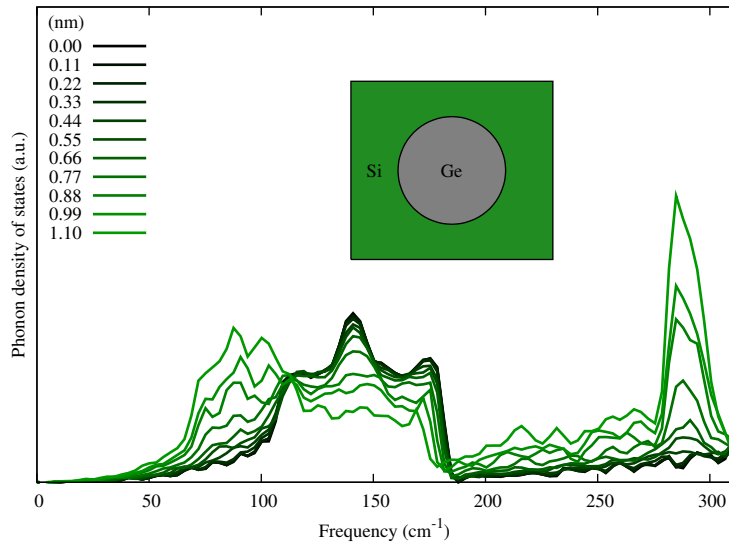


Figure 2.12: Phonon density of states of different sized Ge quantum dot embedded in a Si matrix. The legend indicates the dot radius.

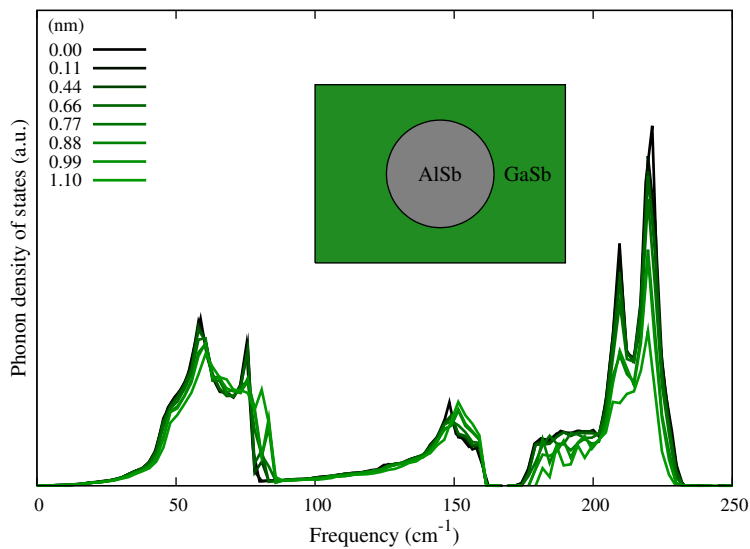


Figure 2.13: Phonon density of states of different sized AlSb quantum dot embedded in a GaSb matrix. The legend indicates the dot radius.

2.6 Gaps in the density of states, a lost cause ?

2.6.1 Superlattice: how gaps are filled

If a gap in the dispersion relation may indeed be observed in the superlattice growing direction [138, 142], this gap does not exist *at the same energy* in any other direction. This feature is illustrated in figure 2.15, where the phonon density of states was calculated by the integration of the band structure on specific directions, from the growing axis to

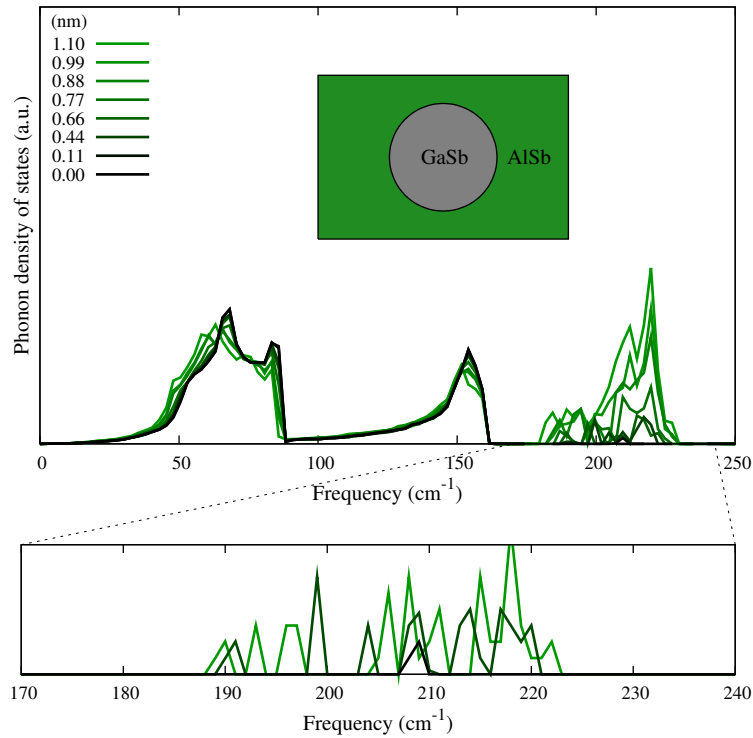


Figure 2.14: Phonon density of states of different sized GaSb quantum dot embedded in an AlSb matrix. The legend indicates the dot radius.

the in-plane axis, for a Si_6Ge_2 superlattice. The gap that exists along ΓZ (the grey area delimited by the two arrows) gets narrower as the integration direction has an increasing in-plane component, until it totally disappears when the z-component reaches 0. The whole space integration though cannot lead to a full, nor a deep, gap in the phonon density of states in the case of a superlattice.

2.6.2 Quantum dot: how gaps vanish because dots are not round

To expand the gap as observed in superlattices in the direction perpendicular to the interface, one would need, at the atomic scale, a flat interface in every direction around a centre, i.e. a perfectly round dot. In the limit of an infinitely small dot, the atomic feature of matter forbid to consider an isotropically smooth interface. In the limit of a large dot, it is tantalizing to treat the system in an elastic continuum model. Yet, this would not include the enormous number of internal degrees of freedom whose corresponding modes vibrational energy is likely to span a large range below the highest optic frequency. In addition, when depopulating a dense frequency region, one has to be careful not to populate a previously empty range that may create new two-phonon final states. This is intrinsically in contradiction with criteria (iii) (see section (1.4.2)) since a wide frequency range would be required to avoid density peaks overlaps.

This is an example of an inverse problem, since it would obviously be more efficient to

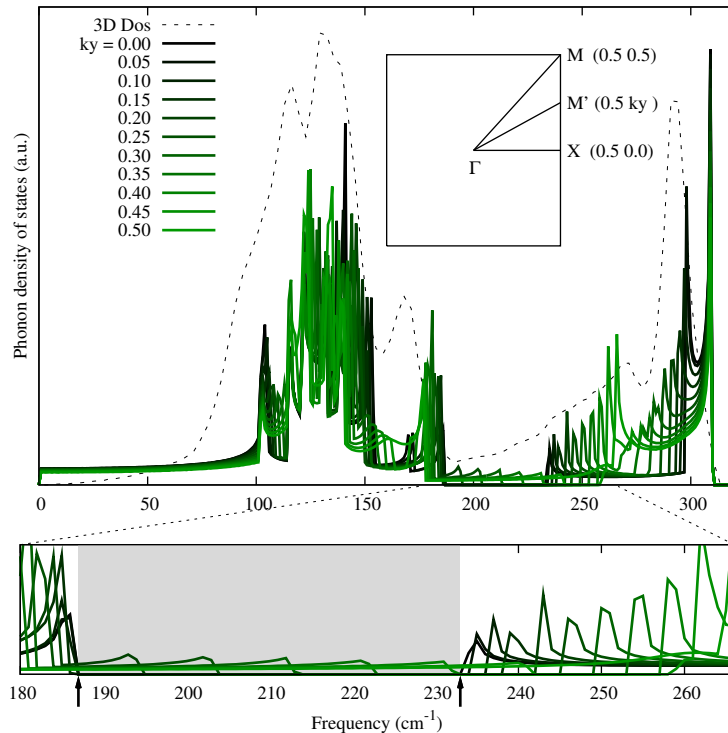


Figure 2.15: Directional phonon density of states in Si_6Ge_2 . The inset illustrates the integration direction in the Brillouin zone. The banner at the bottom in a zoomed picture of a filled acoustic gap.

look for a crystal structure and composition from a given band dispersion, if only it were solvable. However, it has been estimated that such a sufficient single gap in the phonon density of states would be achievable with a 1 nm^3 at the most quantum dot, whose single element exhibits a mass ratio a $1/7$ with the matrix one [83]. This leaves few hopes for the practical achievement of such a phonon band structure.

2.6.3 How it turns out that gaps are sufficient but not necessary

We showed that engineering phonon band structure with, as a goal, the creation of well energetically positioned gaps in the density of states is a very complicated task. It is even more true considering the fact that we have restricted ourselves to cubic systems. For crystal with lower symmetry, the increasing number of degree of freedom decreases the chance to find reasonably large forbidden phonon energy range. However, it is important at this point to recall that the experimental pieces of evidence of the hot-carrier effect have not been highlighted in such materials. In the numerous $GaAs/Al_xGa_{1-x}As$ superlattices systems in which it has *not* been reported [67, 68, 54], it is manifest, referring to figure 2.6, 2.10, and to the previous discussion, that there is no chance to witness an appropriate phonon gap. This later feature is thus a *sufficient but not necessary* condition for a material to be a good candidate for hot-carrier solar cells from a phonon point of

view. From the results presented in this chapter, it appears that such gaps are more likely to be found in bulk materials, such as in SiSn.

2.7 Conclusion on the two-phonon final states investigation

Basic elements of the Physics of phonons were recalled, as well as a summary of the derivation of the dynamical matrix within Density Functional Perturbation Theory. Based on previously existing elements in the literature, an accurate nomenclature of the two-phonon final states was developed.

A detailed study of LO-phonon decay was performed in various III-V and group-IV bulk semiconductors, which revealed that in addition to the atomic mass ratio, the electronegativity difference, related to the LO-TO splitting, was a key parameter to take into account when discriminating potential candidates that exhibit few two-phonon final states. This explains in particular why experimental verification showed that *InN* has a much shorter phonon lifetime than what it was when only considering the atomic mass ratio.

The creation and evolution of gaps in the one-phonon density of states were investigated in *Si/Ge* and *GaSb/AlSb* superlattices. It has been confirmed that, while such a gap can indeed be found in the *growing direction*, the overall integration of the dispersion relation fade it, and that if no specific symmetry conservation rule restricts the two final phonons possible wavevector, expecting a thermalisation rate reduction in such a system *because of the phonon band structure* is by no means relevant.

Finally, it was highlighted that SiSn shows hitherto unseen features, that may be set as target for bulk candidate seeking. For this reason, an even more detailed study of the LO-phonon in this material is to be performed, by investigating the weight of each type of final states using third order Density Functional Perturbation Theory, and get a fully *ab initio* calculation of the phonon lifetime.

Chapter 3

Phonons: decay rate

Contents

3.1	LO-phonon lifetime	62
3.1.1	Phonon decay from experiment	62
3.1.2	Lifetime in bulk materials	62
3.2	Formalism - Beyond the harmonic approximation	63
3.2.1	Derivation	63
3.2.2	State of the art of phonon lifetime calculation	65
3.2.3	Drawbacks of tantalizing approximations	65
3.2.4	Misleading success in fitting experimental data	66
3.3	Third order anharmonic tensor within DFPT	67
3.4	Practical implementation	69
3.4.1	Phonons eigenvectors and eigenfrequencies	69
3.4.2	q-space mesh and energy smearing	69
3.4.3	The two-phonon density of final states	71
3.4.4	Validation and commentary on DFPT for HCSC	72
3.5	Application to SiSn	73
3.5.1	Two-phonon density of states	73
3.5.2	Lifetime of the LO-phonon: beyond the zone centre approximation	74
3.5.3	Lifetime dependence on the LO-phonon reciprocal position	75
3.5.4	Eventual photovoltaic efficiency	76
3.6	Towards higher orders-phonon processes	77
3.6.1	Previous discussions on four-phonon processes	77
3.6.2	Estimation of the four-phonon processes contribution	79
3.6.3	Consecutive three-phonon processes	80
3.6.4	Crystal symmetry and higher-order anharmonic tensors	82
3.7	Conclusions on LO phonon lifetime calculations for HCSC	84
3.7.1	SiSn features as references	84
3.7.2	Limitations	85
3.7.3	Towards other ways to hinder carrier cooling	85

3.1 LO-phonon lifetime

In this section is recalled the relation between LO-phonon lifetime and experimental measurements, as well as this chapter field of study.

3.1.1 Phonon decay from experiment

Considering phonons to be eigen modes easily reach a limit, for instance, by the reality of a finite thermal conductivity. This non-ideality feature finds a macroscopic analogy in the fact that there is no such a thing as a spring vibrating *ad infinitum*. A basic hypothesis then is to assume that phonons have an intrinsic lifetime due to their anharmonic feature, and that they decay into other pseudo-harmonic modes. This decay time was shown to be probed experimentally.

Raman spectroscopy

A Raman experiment consists in measuring the shift in energy of a beam of photons sent on a sample due to their inelastic interaction with matter. They either yield (Stokes shift) or gain (anti-Stokes shift), at first order, one quantum of inner-cell lattice vibration, an optic phonon. From an experimental point of view, and for an isotopically pure crystal [143], the phonon lifetime τ is related to the full width at half maximum Γ of the one-phonon Raman peak through $\Gamma = 1/2\tau$. Because of this relation, and because the accuracy of a Raman experiment is limited, measurable lifetimes can only be of the order or lower than few tens of picoseconds (*short lifetimes*).

Time-resolved coherent anti-Stokes Raman spectroscopy

Another technique uses a picosecond coherent excitation of phonons (Stokes Raman scattering) whose population decrease is probed through coherent anti-Stokes Raman scattering, with a decay probability per unit of time of $1/\tau$. The phonon population lifetime is *not*, strictly speaking, equivalent to the phonon lifetime because of the phonon generation time [143]. However, for a long phonon lifetime, exceeding typically 10 ps (*long lifetimes*), the phonon generation time is small compared to the decay time, so that the measured quantity is close to the bare phonon lifetime.

Hence, Raman spectroscopy is suitable for *short* lifetimes, while Time-resolved coherent anti-Stokes Raman spectroscopy is, on the other hand, suitable for *long* lifetimes [144].

3.1.2 Lifetime in bulk materials

LO-phonon lifetime has been experimentally investigated mostly in bulk material, in which it commonly ranges between 1 and 20 ps near 0 K, and between ~ 0.1 and ~ 10 ps at room temperature (see section (3.2.4)). The target value for the LO-phonon lifetime to be sufficient for hot-carrier solar cells practical implementation is ~ 100 ps,

one order of magnitude greater than the *common range* (1.4). Bare phonon lifetime in nanostructured materials, and more particularly in quantum wire and quantum dots [53], may not be a relevant parameter because of the strong electron-phonon or plasmon-phonon coupling [76, 79]. More than in bulk materials, it cannot be studied independently from the electronic density [145, 146].

Considering the peculiar features noticed in chapter 2, we focus in the following on the *SiSn* bulk case. Based on the elements of the Physics of phonons recalled in 2.1, the analytical formulation of the LO-phonon lifetime is derived, followed by its implementation within Density Functional Perturbation Theory and the eventual results.

3.2 Formalism - Beyond the harmonic approximation

So far we have addressed vibrational issues within the harmonic approximation, i.e. assuming the phonons to be *eigen modes*. To account for experimental evidence of phonons finite lifetime, we have to go beyond this latter assumption, so one order at least further in the total energy development.

3.2.1 Derivation

Back to equation (2.2), we focus this time on the fourth term of the sum, the third derivative of the energy:

$$E_{tot}^{(3)}(\{\mathbf{u}_I^l\}) = \frac{1}{3!} \sum_{l'l''l'''} \frac{\partial^3 E_{tot}}{\partial u_{I,\alpha}^l \partial u_{J,\beta}^{l'} \partial u_{K,\gamma}^{l''}} u_{I,\alpha}^l u_{J,\beta}^{l'} u_{K,\gamma}^{l''} \quad (3.1)$$

where \mathbf{u} is the displacements around the equilibrium position, that we express this time in terms of phonon creation ($a_s^\dagger(\mathbf{q})$) and annihilation ($a_s(-\mathbf{q})$) operators through the second quantization [147]:

$$u_{I,\alpha}^l = \sum_{\mathbf{q},s} \left(\frac{\hbar}{2\omega_s(\mathbf{q})M_I N} \right)^{\frac{1}{2}} e_{I,\alpha}(\mathbf{q},s) e^{i\mathbf{q}\cdot\mathbf{R}^l} \left(a_s^\dagger(-\mathbf{q}) + a_s(\mathbf{q}) \right) \quad (3.2)$$

where M_I is the mass of atom I , N the number of unit cells in the crystal. $e_{I,\alpha}(\mathbf{q},s)$ is the (I,α) element of the phonon eigenvector, solution of the secular equation (2.11). Inserting equation (3.2) into (3.1), we obtain the fourth order term, or the first anharmonic order, of the Hamiltonian:

$$H^{(3)} = \frac{1}{3!} \sum_{\mathbf{q},\mathbf{q}_2,\mathbf{q}_3,s,s_2,s_3} V \begin{pmatrix} \mathbf{q} & \mathbf{q}_2 & \mathbf{q}_3 \\ s & s_2 & s_3 \end{pmatrix} \left[\left(a_s^\dagger(-\mathbf{q}) + a_s(\mathbf{q}) \right) \left(a_{s_2}^\dagger(-\mathbf{q}_2) + a_{s_2}(\mathbf{q}_2) \right) \left(a_{s_3}^\dagger(-\mathbf{q}_3) + a_{s_3}(\mathbf{q}_3) \right) \right] \quad (3.3)$$

The expression of V will be recalled at the end of the section. We place ourself in the zone-centre approximation (section 2.4.1.1), so that $\{ \mathbf{q}, s \}$, $\{ \mathbf{q}_2, s_2 \}$, and $\{ \mathbf{q}_3, s_3 \}$

become respectively $\{ \mathbf{0}, LO \}$, $\{ \mathbf{q}, s_2 \}$ and $\{ -\mathbf{q}, s_3 \}$. Developing the products in the square brackets leads to eight sub-terms in the Hamiltonian, gathered in table 3.1. The

	a product	Relevance
1	$a_{LO}^\dagger(\mathbf{0}) a_{s_2}^\dagger(-\mathbf{q}) a_{s_3}^\dagger(\mathbf{q})$	Forbidden
2	$a_{LO}^\dagger(\mathbf{0}) a_{s_2}^\dagger(-\mathbf{q}) a_{s_3}(-\mathbf{q})$	Forbidden
3	$a_{LO}^\dagger(\mathbf{0}) a_{s_2}(\mathbf{q}) a_{s_3}^\dagger(\mathbf{q})$	Forbidden
4	$a_{LO}^\dagger(\mathbf{0}) a_{s_2}(\mathbf{q}) a_{s_3}(-\mathbf{q})$	Allowed
5	$a_{LO}(\mathbf{0}) a_{s_2}^\dagger(-\mathbf{q}) a_{s_3}^\dagger(\mathbf{q})$	Allowed
6	$a_{LO}(\mathbf{0}) a_{s_2}^\dagger(-\mathbf{q}) a_{s_3}(-\mathbf{q})$	Forbidden
7	$a_{LO}(\mathbf{0}) a_{s_2}(\mathbf{q}) a_{s_3}^\dagger(\mathbf{q})$	Forbidden
8	$a_{LO}(\mathbf{0}) a_{s_2}(\mathbf{q}) a_{s_3}(-\mathbf{q})$	Forbidden

Table 3.1: Creation-annihilation terms of the third-order Hamiltonian within the zone-centre approximation

first and eighth terms are energetically forbidden in any case. Terms 2, 3, 6 and 7 are also forbidden if we consider that no phonon has an energy higher than the zone-centre LO-phonon one, which is the case in Zinc-Blende crystals. The remaining two terms, 4 and 5, represent respectively the "fusion" of two phonons into one LO-phonon, and the decay of an LO-phonon into two lower energy phonons. At thermal equilibrium, the two processes are balanced and the occupation number of any state $\{ \mathbf{q}, s \}$ is given by the Bose-Einstein distribution:

$$n^s(\mathbf{q}) = \frac{1}{e^{\frac{\hbar\omega^s(\mathbf{q})}{k_B T}} - 1} \quad (3.4)$$

where T is the lattice temperature, and $n^s(\mathbf{q})$ is related to the creation and annihilation operators through standard notations:

$$a_s^\dagger(\mathbf{q})|n^s(\mathbf{q})\rangle = \sqrt{n^s(\mathbf{q}) + 1}|n^s(\mathbf{q}) + 1\rangle \quad (3.5)$$

$$a_s(\mathbf{q})|n^s(\mathbf{q})\rangle = \sqrt{n^s(\mathbf{q})}|n^s(\mathbf{q}) - 1\rangle \quad (3.6)$$

As we saw in chapter 1, the electron cooling, or the laser pulse in a Raman experiment, generates an out-of-equilibrium population of LO-phonons. In this case, the contribution of term 4 in table 3.1 is highly negligible compared to term 5, so that we retain only this latter one. The rate of this process is given by the Fermi golden rule:

$$\Gamma = \frac{2\pi}{\hbar} \sum_f \left| \langle f | H^{(3)} | i \rangle \right|^2 \delta(E_f - E_i) \quad (3.7)$$

Inserting equation (3.3) into (3.7) makes the LO-phonon decay rate write, within the zone-centre approximation:

$$\Gamma = \frac{\pi}{2\hbar^2} \sum_{\mathbf{q}, s_2, s_3} \left| V \begin{pmatrix} \mathbf{0} & \mathbf{q} & -\mathbf{q} \\ LO & s_2 & s_3 \end{pmatrix} \right|^2 \times (n^{s_2}(\mathbf{q}) + 1)(n^{s_3}(-\mathbf{q}) + 1) \delta(\omega^{LO}(\mathbf{0}) - \omega^{s_2}(\mathbf{q}) - \omega^{s_3}(-\mathbf{q})) \quad (3.8)$$

where the matrix element V takes the cumbersome visual form:

$$V \begin{pmatrix} \mathbf{0} & \mathbf{q} & -\mathbf{q} \\ LO & s_2 & s_3 \end{pmatrix} = \sum_{\substack{I, J, K \\ \alpha, \beta, \gamma}} \left(\frac{\hbar^3}{8NM_I M_J M_K \omega^{LO}(\mathbf{0}) \omega^{s_2}(\mathbf{q}) \omega^{s_3}(-\mathbf{q})} \right)^{\frac{1}{2}} \times \left[\sum_{l', l''} \frac{\partial^3 E_{tot}}{\partial u_{I, \alpha}^l \partial u_{J, \beta}^{l'} \partial u_{K, \gamma}^{l''}} e^{i\mathbf{q} \cdot (\mathbf{R}^{l'} - \mathbf{R}^{l''})} \right] e_{I, \alpha}(\mathbf{0}, LO) e_{J, \beta}(\mathbf{q}, s_2) e_{K, \gamma}(-\mathbf{q}, s_3) \quad (3.9)$$

The factor between square brackets is called the *anharmonic tensor*.

3.2.2 State of the art of phonon lifetime calculation

Within the elastic continuum model (see for instance [148]), several LO-phonon lifetime calculations were performed in simple bulk binary semiconductors. In this case, the third-order anharmonic tensor taken as a \mathbf{q} -, atom- and coordinate-independent parameter, written either as a function of the experimentally measured second- and third-order elastic constants [149, 125], or, slightly differently, of the Gruneisen parameter, the material density, and the average acoustic velocity [49, 126]. The difficulty in evaluating the anharmonic tensor leads some authors to prejudice the results either on its value, or on the channels involved [43, 150, 107]. In the mid-90's, a full *ab initio* calculation was introduced [151] in order to get rid of the constant anharmonic tensor approximation. The guiding lines of this method will be given in section (3.3).

3.2.3 Drawbacks of tantalizing approximations

Taking anharmonic tensor as a constant parameter and assuming that the polarisation overlap is consistently of the order of unity [150, 88, 109] leads to the problem of ghost channels. Let us take once again Silicon as a simple instance, and find the LO-phonon decay channels on the ΓL -branch when the two-atom Zinc-Blende primitive cell is taken as the crystal building block (figure 3.1, left). The only allowed channel in this direction is the first Klemens channel (blue line), leading to two phonons of equal energies. If we mentally duplicate the building block by a factor of two in all crystallographic directions, we end up with an eight times larger "primitive" cell. In addition to the equivalent of the first Klemens channel (green line), a considerably larger number of other decay channels (black lines)

are found in this case (figure 3.1, right). Since the two materials are identical, the black channels are ghost channels, have not physical relevance, and the information allowing to remove them *has* to be contained in mode- and \mathbf{q} -dependent factors of the matrix element V (equation (3.9)), namely the anharmonic tensor and the polarisation vectors overlap. This argument shows how delicate working with these common approximations can be. Beyond the pointless complication of a non-primitive cell in a bulk calculation, this issue

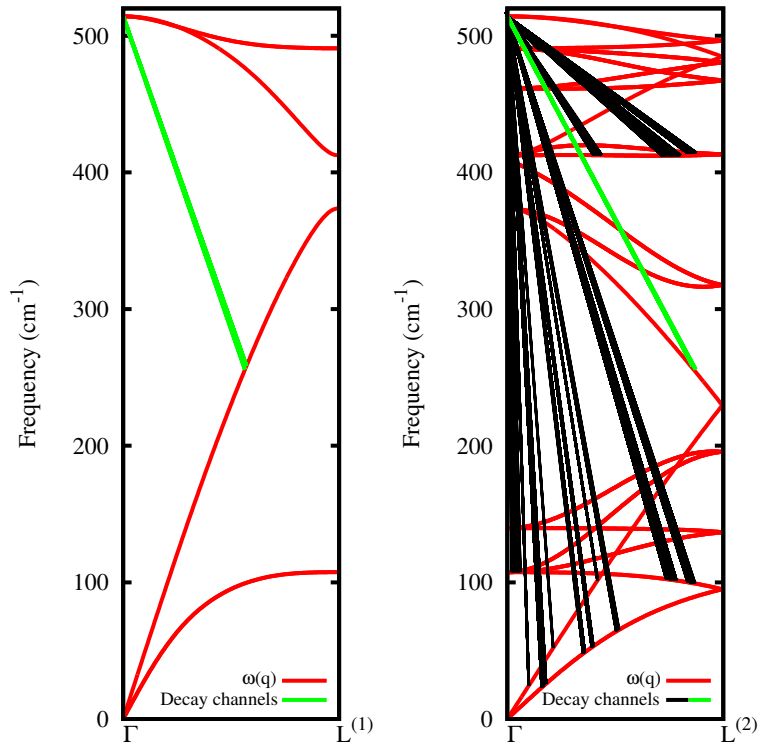


Figure 3.1: (Left) LO-phonon decay channels in bulk Si when the two-atom Zinc-Blende primitive cell is taken as the crystal building block. (Right) LO-phonon decay channels in bulk Si when an eight times larger cell is taken as the crystal building block. The blue line highlights the single common channel between the two, hence the only relevant one.

is of considerable importance in the study of non defect-free crystals, where new channels of unknown contribution relevance may appear, not to talk about the superlattice cases for which the band folding is definitely not an artifact anymore.

3.2.4 Misleading success in fitting experimental data

With the anharmonic tensor taken as a scalar adjustable parameter, though, one can fit experimental data and reproduce the temperature dependence of the phonon lifetime. This was done in the cases of different bulk Zinc-Blende semiconductors for which experimental data were available, and the results are depicted in figure 3.2. The calculated lines follow well the different experimental trends, but, this *does not* give any information on the relative weight of the different processes, *nor* allows to make predictions.

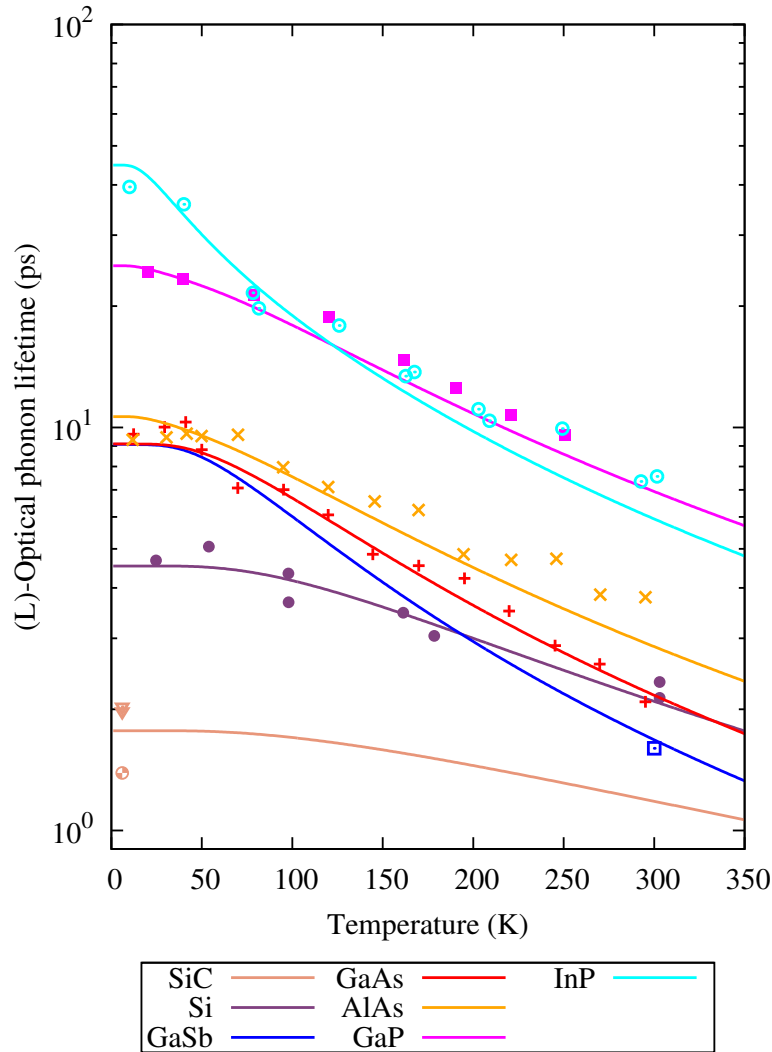


Figure 3.2: LO-phonon lifetime for several Zinc-Blende III-V and IV-IV semiconductors, calculated using a scalar adjustable parameter for the third derivative of the energy (square bracket in equation (3.9)). Experimental data points, acquired using time-resolved coherent anti-Stokes Raman spectroscopy, are reproduced from [105, 125, 152, 136, 106, 107]

3.3 Third order anharmonic tensor within DFPT

The importance to have a first principles knowledge of the third order derivative of the energy upon displacement was shown. In this section, we derive the computational methodology to reach and make use of this latter quantity within Density Functional Perturbation Theory. The complete technical description can be found in [144], [104], and [124]. In the same spirit as in equation (2.5), we express the third order of the total energy as:

$$E_{tot}^{(3)}(\{\mathbf{u}_I^l\}) = \frac{1}{3!} \sum_{l'l''} C_{I,\alpha;J,\beta;K,\gamma}(l,l',l'') u_{I,\alpha}^l u_{J,\beta}^{l'} u_{K,\gamma}^{l''} \quad (3.10)$$

with $C_{I,\alpha;J,\beta;K,\gamma}(l, l', l'')$ defined as:

$$C_{I,\alpha;J,\beta;K,\gamma}(l, l', l'') := \frac{\partial^3 E_{tot}}{\partial u_{I,\alpha}^l \partial u_{J,\beta}^{l'} \partial u_{K,\gamma}^{l''}} \quad (3.11)$$

It is the key ingredient in the matrix element (3.9). It can be rewritten in the wavevector space:

$$C_{I,\alpha;J,\beta;K,\gamma}(\mathbf{q}, \mathbf{q}', \mathbf{q}'') = \frac{1}{N} \sum_{l, l', l''} C_{I,\alpha;J,\beta;K,\gamma}(l, l', l'') e^{i\mathbf{q}\cdot\mathbf{R}^l} e^{i\mathbf{q}'\cdot\mathbf{R}^{l'}} e^{i\mathbf{q}''\cdot\mathbf{R}^{l''}} \quad (3.12)$$

Making use of the reciprocal space expression for the lattice distortion:

$$\mathbf{u}_I(\mathbf{q}) = \sum_l \mathbf{u}_I^l e^{i\mathbf{q}\cdot\mathbf{R}^l} \quad (3.13)$$

and replacing label (I, α) with p for clarity, we can rewrite equation (3.11):

$$C_{p,p',p''}(\mathbf{q}, \mathbf{q}', \mathbf{q}'') = \frac{\partial^3 E_{tot}}{\partial u_p(\mathbf{q}) \partial u_{p'}(\mathbf{q}') \partial u_{p''}(\mathbf{q}'')} \quad (3.14)$$

It was demonstrated [151, 144] that $C_{pp'p''}(\mathbf{q}, \mathbf{q}', \mathbf{q}'')$ can be decomposed into a sum of permutation terms:

$$\begin{aligned} C_{pp'p''}(\mathbf{q}, \mathbf{q}', \mathbf{q}'') &= \tilde{E}_{pp'p''}(\mathbf{q}, \mathbf{q}', \mathbf{q}'') + \tilde{E}_{pp'p''}(\mathbf{q}', \mathbf{q}, \mathbf{q}'') \\ &+ \tilde{E}_{pp'p''}(\mathbf{q}, \mathbf{q}'', \mathbf{q}') + \tilde{E}_{pp'p''}(\mathbf{q}'', \mathbf{q}', \mathbf{q}) \\ &+ \tilde{E}_{pp'p''}(\mathbf{q}', \mathbf{q}'', \mathbf{q}) + \tilde{E}_{pp'p''}(\mathbf{q}'', \mathbf{q}', \mathbf{q}) \end{aligned} \quad (3.15)$$

in which each \tilde{E} is a sum of an electronic part and an electronic density-independent ionic part:

$$\tilde{E}_{pp'p''}(\mathbf{q}, \mathbf{q}', \mathbf{q}'') = \tilde{E}_{pp'p''}^{el}(\mathbf{q}, \mathbf{q}', \mathbf{q}'') + \tilde{E}_{pp'p''}^{ion}(\mathbf{q}, \mathbf{q}', \mathbf{q}'') \quad (3.16)$$

The former contribution takes the broddingnagian¹ form:

$$\begin{aligned} \tilde{E}_{pp'p''}^{el}(\mathbf{q}, \mathbf{q}', \mathbf{q}'') &= \\ &\sum_{\nu} \left\langle \frac{\partial \psi_{\nu}}{\partial u_p(\mathbf{q})} \left| P_c \frac{H}{\partial u_{p'}(\mathbf{q}')} P_c \left| \frac{\partial \psi_{\nu}}{\partial u_{p''}(\mathbf{q}'')} \right. \right\rangle - \sum_{\nu'} \left\langle \frac{\partial \psi_{\nu'}}{\partial u_p(\mathbf{q})} \left| P_c \left| \frac{\partial \psi_{\nu'}}{\partial u_{p'}(\mathbf{q}')} \right. \right\rangle \left\langle \psi_{\nu'} \left| \frac{H}{\partial u_{p''}(\mathbf{q}'')} \right| \psi_{\nu'} \right\rangle \\ &+ \frac{1}{2} \int \frac{\partial^2 V_{ion}(\mathbf{r})}{\partial u_{p'}(\mathbf{q}') \partial u_{p''}(\mathbf{q}'')} \frac{\partial n(\mathbf{r})}{\partial u_p(\mathbf{q})} d\mathbf{r} + \frac{1}{6} \int \frac{\partial^2 V_{ion}(\mathbf{r})}{\partial u_p(\mathbf{q}) \partial u_{p'}(\mathbf{q}') \partial u_{p''}(\mathbf{q}'')} n(\mathbf{r}) d\mathbf{r} \\ &+ \frac{1}{6} \int \frac{\delta^3 E_{xc}[n]}{\delta n(\mathbf{r}) \delta n(\mathbf{r}') \delta n(\mathbf{r}'')} \frac{\partial n(\mathbf{r})}{\partial u_p(\mathbf{q})} \frac{\partial n(\mathbf{r}')}{\partial u_{p'}(\mathbf{q}')} \frac{\partial n(\mathbf{r}'')}{\partial u_{p''}(\mathbf{q}'')} d\mathbf{r} d\mathbf{r}' d\mathbf{r}'' \end{aligned} \quad (3.17)$$

1. Jonathan Swift, *Gulliver's Travels*

In accordance with the "2n+1" theorem [113], the six-order $C_{p,p',p''}(\mathbf{q}, \mathbf{q}', \mathbf{q}'')$ matrix, and thus the third derivative of the total energy, is a functional of *only the electronic density and its first derivative*. Its full derivation was done in an essential work by A. Debernardi and co-workers [153] for elemental semiconductors in the zone-centre approximation, then extended to polar semiconductors [104], and finally generalized very recently to any \mathbf{q} -vector triplet by L. Paulatto and co-workers [124].

3.4 Practical implementation

In this section we take a closer look at the key ingredients appearing in the phonon decay rate equation (3.9). In particular, a great care is taken to assess the relevance of some approximations very commonly found in the literature. The example of bulk Silicon is taken as a case in point to illustrate the following subsections.

3.4.1 Phonons eigenvectors and eigenfrequencies

It has been shown in section (2.3.1) that the phonon frequencies and related atomic displacements can be computed at any \mathbf{q} -vector within Density Functional Perturbation Theory with the same computational cost. As also previously said in section (3.2.3), it is tantalising to prejudice the result of the polarisation overlap, which is the triple atomic displacements product in the right-hand-side of (3.9), by simply considering the involved branches polarisation label. Doing so, a final state involving one LA and one TA-phonon would lead to an overlap of zero, while two LA-phonons would lead to unity [150]. This sophism is the result of a misuse of the terms *longitudinal* and *transverse*, which are strictly valid, from a semantic point of view, *only* in the vicinity of the Γ point. The polarisation, i.e. the longitudinal or transverse character, of the six branches in bulk Silicon is depicted in figure 3.3: each point of a series of \mathbf{q} -slabs in the irreducible Brillouin zone is colored according to its longitudinality, the red colour standing for a fully longitudinal mode, while the blue colour for a fully transverse mode. It appears that the longitudinal or transverse feature of the branches is \mathbf{q} -dependent and easily leads to hybrid characters, as it was obvious *a priori*. This is the reason why the polarisation overlap must be rigorously calculated for each sextuplet $\{I, \alpha; J, \beta; K, \gamma\}$.

3.4.2 \mathbf{q} -space mesh and energy smearing

In section (2.4.1.2) a rectangular function was used to mimick the conservation delta function of equation (2.33). This check function, reported here in equation (3.8), is taken as a Gaussian function of the form [124]:

$$\tilde{\delta}(\omega) = \frac{1}{\sigma\sqrt{2\pi}} e^{-\left(\frac{(\omega-\omega_{LO})^2}{2\sigma^2}\right)} \quad (3.18)$$

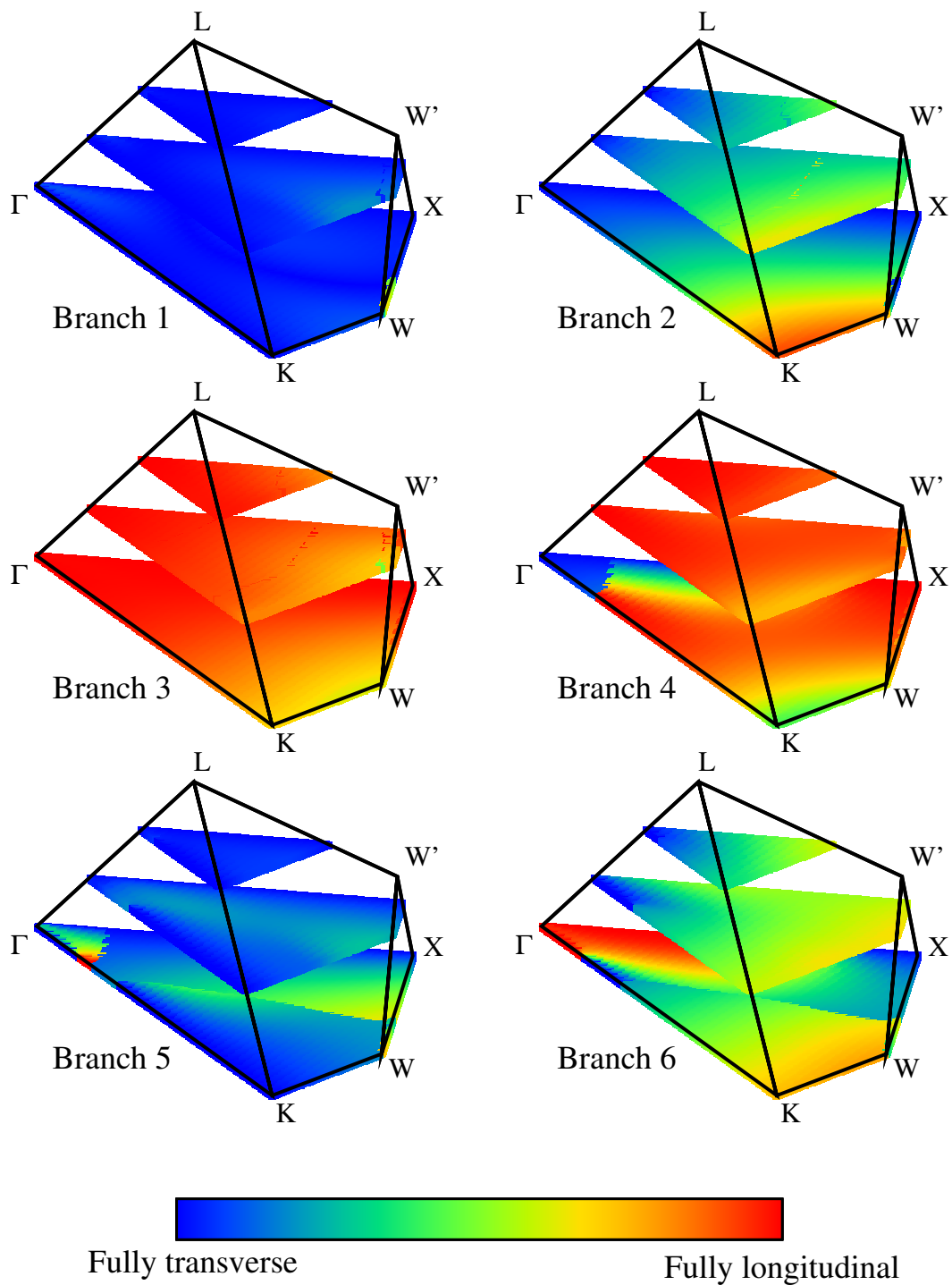


Figure 3.3: Phonon branch polarisation in reciprocal space slices, for bulk Silicon. The red (blue) colour stands for fully longitudinal (transverse) branch. Discontinuities (branches 4, 5 and 6) are due to band crossing (the branches numerotation is simply based on their relative order in energy.)

where ω is the sum of the two final phonons frequency, σ is set to 1 cm^{-1} (a discussion on the proper choice of this parameter is proposed in appendix F). The third order tensor calculation is expected to be computationally demanding. Hence, $\tilde{\delta}$ is used to restrict the number N_q of \mathbf{q} -point in the sum (3.8), so that only the ones for which $\tilde{\delta}(\omega)/\tilde{\delta}(\omega_{LO}) > 0.1$ are retained. The convergence study on the q-space mesh is plotted in figure 3.4, where the reference parameter is taken as the experimental LO-phonon lifetime. It appears that a $25 \times 25 \times 25$ \mathbf{q} -points density is required as a minimum so to reach satisfactorily converged results. On the same figure is depicted the corresponding computational time, that indeed follows a cubic increase upon N_q (dashed blue line), of the form $c \cdot N_q^3$. This highlights the necessity to first perform a second-order calculation as in chapter 2 in order to select only materials in which the volume of final states is small, typically of the order of InP, or confined near the Brillouin zone edges, so not to have to perform a systematic third order calculation for all studied materials.

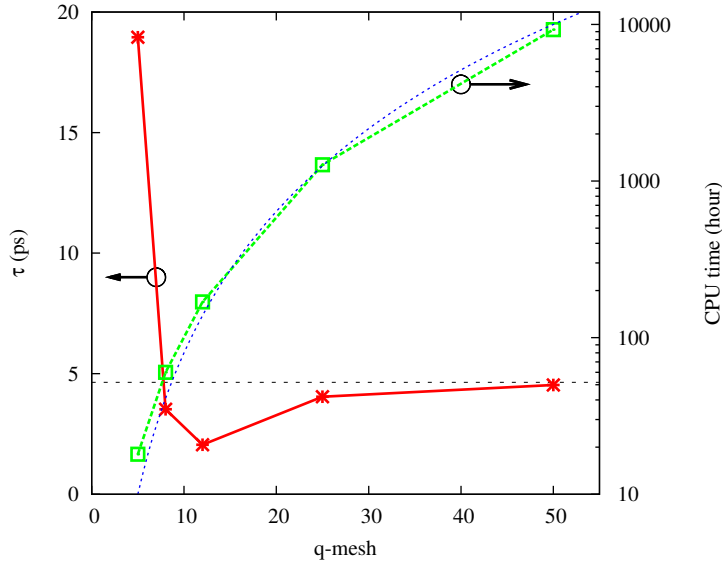


Figure 3.4: Convergence of the sum (3.8) on the reciprocal space mesh (red) and corresponding CPU time (green). The number on the x-axis is the number of intervals from the zone centre to the zone boundary. The black dotted line is the LTO-phonon lifetime extrapolated at 0 K from experimental results [125]. The dashed blue line is a cubic fit of the CPU time dependence on \mathbf{q} density.

3.4.3 The two-phonon density of final states

Also called the *frequency-resolved final states spectrum*, the two-phonon density of (final) states (*2PhDOS*) is defined as:

$$\gamma(\omega_0) = \frac{\pi}{2\hbar^2} \sum_{\mathbf{q}, s_2, s_3} \left| V \begin{pmatrix} \mathbf{0} & \mathbf{q} & -\mathbf{q} \\ LO & s_2 & s_3 \end{pmatrix} \right|^2 \times (n^{s_2}(\mathbf{q}) + 1)(n^{s_3}(-\mathbf{q}) + 1) \delta(\omega^{LO}(\mathbf{0}) - \omega^{s_2}(\mathbf{q}) - \omega^{s_3}(-\mathbf{q})) \delta(\omega^{s_2,3}(\mathbf{q}) - \omega_0) \quad (3.19)$$

and shows the relative final states weight as a function of their energy ω_0 . It is worth

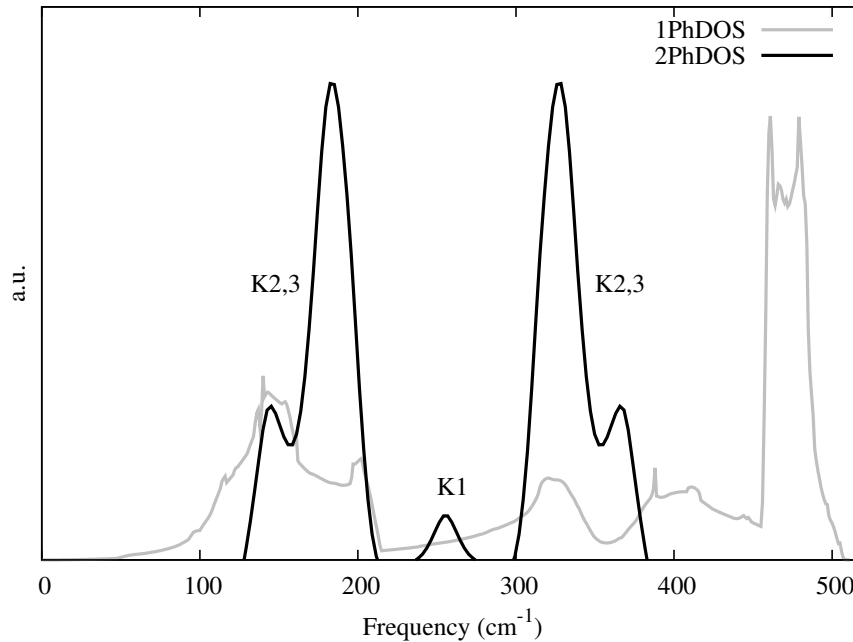


Figure 3.5: One- and two-phonon density of states in Silicon. $K1$, $K2$ and $K3$ stands for *first*, *second* and *third* Klemens states, respectively ($K2$ and $K3$ overlap the same energy range).

noting that the additional delta function in equation (3.19) can be completed with a mode label argument, so to be able to decouple the total weight of each single channel.

The $2PhDOS$ of Silicon is depicted in figure 3.5. As found elsewhere [153], the LTO-phonon decay in this case turns out to be led by the second and third Klemens channels rather than by the first Klemens channel, i.e. two final phonons of equal energy, which turns out to contribute very little compared to the two others; strictly opposite results can be found within the scalar anharmonic factor approximation and a simplistic picture of the phonon polarisation overlap [150].

3.4.4 Validation and commentary on DFPT for HCSC

The integration of the $2PhDOS$ gives the LTO-phonon lifetime in Si, plotted in figure 3.6 for different temperatures, for a mesh in reciprocal space of $50 \times 50 \times 50$ and a Gaussian width of 1 cm^{-1} . The *ab initio* calculation results reproduce extremely well the experimental measurements. For comparison, the LTO-phonon creation rate from two lower-energy phonons is also depicted on the same figure. It can be verified that this process is fairly negligible compared to the phonon decay.

Several remarks have to be drawn. Firstly, the LTO-phonon decay rate in Si appears to be correctly described by *only* three-phonon processes, neglecting higher orders. It is reasonable, at this point, to assume this would be the case for any semiconductors whose

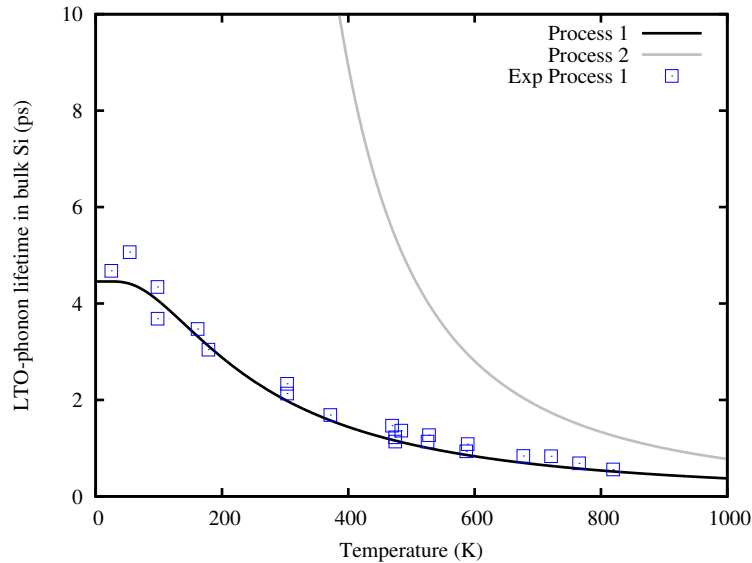


Figure 3.6: LO-phonon decay (process 1) and creation (process 2) in a three-phonon interaction in Silicon. Experimental data are reproduced from [125].

lifetime lays into the experimental range which most of known materials belong to. This is also to be related to a *large* density of final states, typically of the order of the Silicon one. Secondly, this approach shows how careful any attempt to build an analytical or mode-average model should be. The polarisation overlap and the anharmonic tensor remain the most hardly *ad hoc* estimable components. Finally, the computational effort required is an issue when investigating more-than-few atoms systems, since the ratio (*increasing CPU time due to higher number of valence electrons*)/(*reduction time due to smaller Brillouin Zone volume*) is, in every instance, an increasing function of the number of atoms.

3.5 Application to SiSn

SiSn is typically a well chosen case since, among the different semiconductors depicted in figures 2.6 and 2.7, more than the others, catches our attention due to its very small number of available final states. It is thus, from what has just been noted, a case state of a potential hot-carrier solar cell absorber for which we can perform a detailed analysis at a reasonable cost.

3.5.1 Two-phonon density of states

The phonon band structure of *SiSn* computed along high symmetry lines is depicted in figure 3.7, together with the one- and two-phonon densities of states. The latter has been split in two differently coloured parts in figure 3.7: the peaks corresponding to the Ridley states (green) had to be amplified by a factor of 10 so to be visible. The Klemens channels (red) are restricted to a corner of the reduced reciprocal space near the *X*-

point, and the Ridley channels are very few and restricted to the vicinity of the Γ -point. Each of these peculiar features can be explained by one intrinsic parameter. First, the high mass ratio between Sn and Si ($m_{Sn}/m_{Si} = 4.2$) is responsible for an uncommon wide band gap between the optic and the acoustic branches, leaving very few energetically allowed Klemens final states. The Zinc-Blende structure makes the acoustic phonon energy reaching its maximum on the LA-branch at the X -point. Secondly, the electronegativity difference between Si and Sn (0.06 in Pauling units) is among the lowest difference in the periodic table, leading to an extremely small LO-TO splitting (smaller than 3 cm^{-1}), fulfilling condition (ii) (section 1.4.2), so that the Ridley [88] states, involving one TO and one acoustic phonons (LA/TA), are confined in an extremely small volume near the Brillouin zone centre.

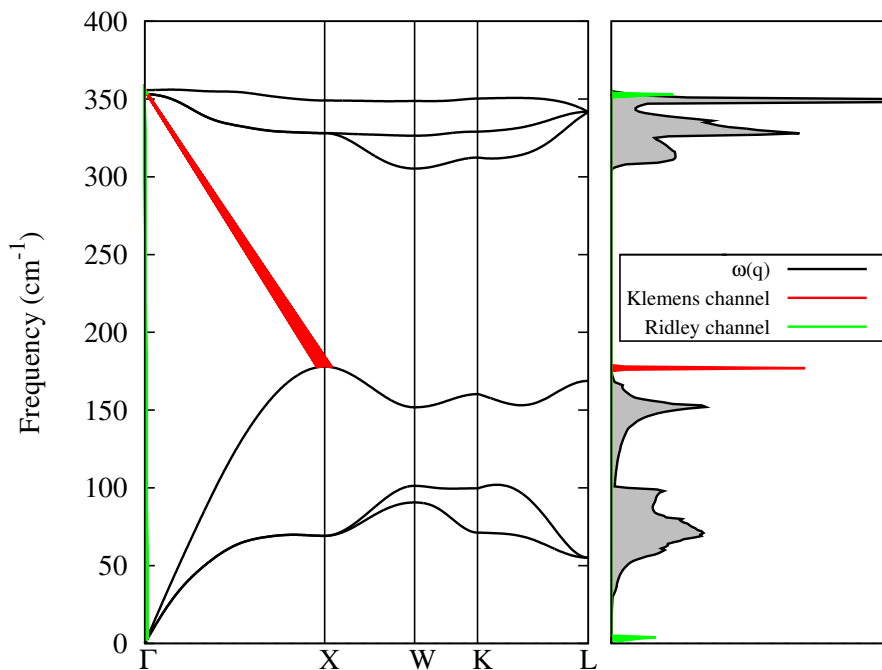


Figure 3.7: (Left) Phonon band structure of SiSn (black) and LO-phonon decays through Klemens and Ridley channels (red and green lines, respectively). (Right) One-phonon density of states of SiSn (dark line) and two-phonon density of states in a two-phonon decay involving one zone-centre LO phonon (red and green lines). The magnitude of the Ridley states in the two-phonon density of states are emphasised by a factor of 10 for clarity.

3.5.2 Lifetime of the LO-phonon: beyond the zone centre approximation

The two-phonon density of final states has been studied as a function of the LO-phonon wavevector. In the case of SiSn, the TPFS volume turns out to be extremely dependent on the wavevector compared to other semiconductors, as can be seen in figure 3.8-(a), in

which we also plotted the case of *Si* for comparison, for a momentum belonging to the ΓX axis. This is a direct consequence of the fact that the final states are close to the Brillouin zone edge (figure 3.7). While the volume is normalized to 1 for $\mathbf{q} = \mathbf{0}$, in the case of *SiSn* it primarily increases with the initial wavevector. This can be understood in the following manner: the volume of the TPFS resulting from Ridley decays undergoes an expansion in the first tenths of percents of ΓX , and although they are fewer than the Klemens states, the Ridley states have a non negligible contribution to the lifetime due to their high polarisation overlap value. This *Ridley volume* then quickly reaches zero above $\mathbf{q}=0.5\%$ of ΓX , and the volume of the TPFS resulting from Klemens channel ('Klemens states') keeps decreasing. Calculating the corresponding phonon lifetime would require to compute the anharmonic tensor for a triplet $\{ \mathbf{q}_{LO}, \mathbf{q}_2, \mathbf{q}_3 \}$ with $\mathbf{q}_{LO} \neq 0$, i.e. to get rid of the zone-centre approximation. In order to save computational time, the anharmonic tensor computed at $\mathbf{q}_{LO} = \mathbf{0}$ was used for all \mathbf{q} -dependent calculations: as the LO-phonon wavevector remains small compared to the Brillouin zone size, it is reasonable to make the assumption:

$$C_{p,p',p''}(\mathbf{0}, \mathbf{q}, -\mathbf{q}) \approx C_{p,p',p''}(\delta\mathbf{q}, \mathbf{q} + \delta\mathbf{q}_2, -\mathbf{q} + \delta\mathbf{q}_3) \quad (3.20)$$

given that $\delta\mathbf{q}_{2,3} \ll \mathbf{q}_{2,3}$ and $\delta\mathbf{q} = \delta\mathbf{q}_1 + \delta\mathbf{q}_2$. The corresponding phonon lifetime is depicted in figure 3.8-(b). Not only at $\mathbf{q} = \mathbf{0}$ the lifetime is already of 3.10^5 ps, but it reaches easily the microsecond range when its momentum is above 2% of the distance between Γ and the zone-boundary, that is five orders of magnitude above all the known values in most III-V and group-IV semiconductors [103]. The lifetime diverges so rapidly that it becomes computationally extremely demanding to calculate it for a momentum above 2.5% of $(\frac{2\pi}{a})$. Actually, above this limit, the volume of the Klemens states shrinks to zero, so that only the Ridley decays remain possible, and the corresponding TPFS volume is extremely small. It is worth noting that the small variation of the two-phonon final states density in Si induces indeed almost no change on the lifetime upon the momentum. To the very knowledge of the author, such a behaviour has never been reported in the literature.

3.5.3 Lifetime dependence on the LO-phonon reciprocal position

The LO-phonon lifetime was computed for every electronic cooling step of an electron belonging to the first conduction band. There is indeed, for each electronic position on a one-dimensional band, only one possible final state that satisfies energy and momentum conservation through a LO-phonon emission due to intravalley scattering. The lifetime of this unique phonon is computed and plotted as a coloured dot at the electron initial position on the band in figure 3.9, so that we visualize a band-curvature dependence of the eventual phonon lifetime. Because the exchange energy in the electron-phonon interaction from one electronic position is of the order of the electronic band derivative at this particular point, high quality band structure is required. It is thus computed within

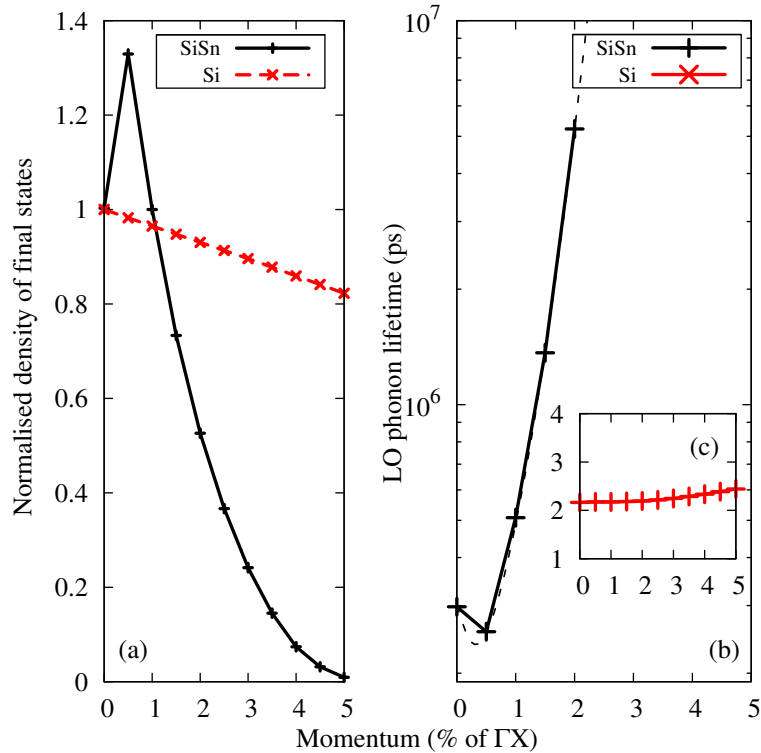


Figure 3.8: (a) Two-phonon final states density variation on initial LO-phonon momentum (belonging to ΓX), for Si and SiSn normalised to the value at the Γ -point. (b-c) Dependence of the LO-phonon lifetime upon its momentum, at 300 K.

G_0W_0 corrected PAW method (see appendix C).

The band structure shows a direct band gap of 0.88 eV at Γ , and two indirect band gaps at L and between Γ and X , of 0.82 and 0.94 eV respectively. This range of optic absorption threshold is favourable for a high conversion efficiency according to condition (iv). It clearly appears that the band curvature has a strong influence on the resulting LO-phonon lifetime in this compound. Thus it can be stated that, in SiSn, depending on the localisation of the electron on the energy surface, the lifetime of the eventual emitted LO phonon is *very* dependent on the flatness of the energy surface, in a three-phonon interaction scheme.

3.5.4 Eventual photovoltaic efficiency

Using the thermodynamic model derived by A. Le Bris and co-workers in reference [77], it is possible to estimate what would be the photovoltaic efficiency of a hot-carrier solar cell based on an absorber having the gap and the LO-phonon lifetime of SiSn, and for which the thermalisation would solely be limited by the LO-phonon decay. Such a material would have a thermalisation coefficient on the order of $10^{-4} W.cm^{-2}.K^{-1}$, leading to a conversion efficiency greater than 70% under 100 suns. The LO-phonon lifetime calculated in this work is thus the required value for a hot-carrier solar cell to operate *in the low concentration*

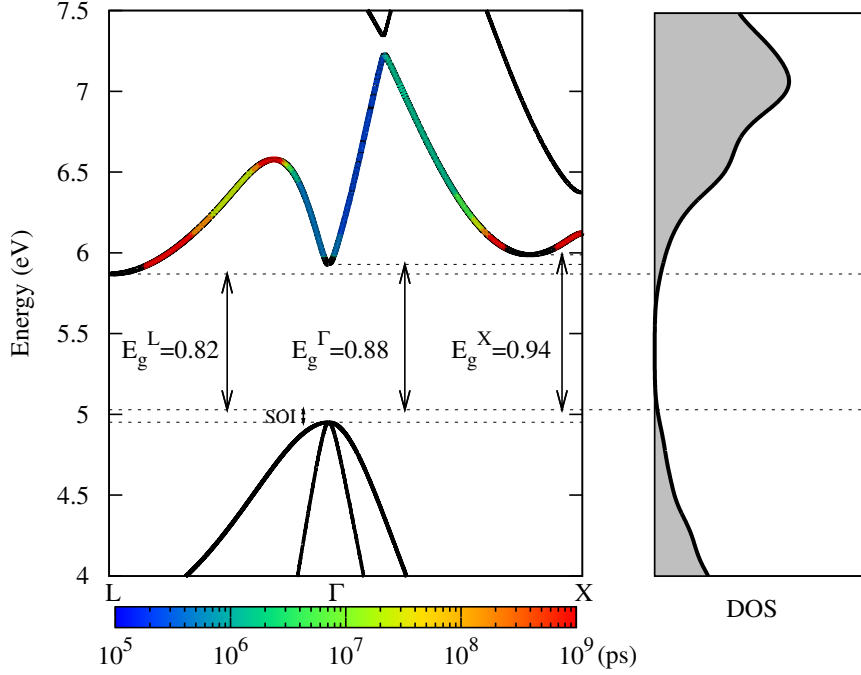


Figure 3.9: (Left) G_0W_0 corrected DFT calculated SiSn electronic band structure. The color of the first conduction band illustrates the corresponding LO phonon lifetime at 300 K via intra-valley scattering (see text). The slope remains black if no phonon fulfilling equations (2.14) and (2.15) is found. (Right) Electronic density of states.

regime with a steady-state hot-carrier population yielding very high conversion efficiency (twice the Shockley Queisser value under similar conditions), and constitutes a target for future hot-carrier absorber materials.

3.6 Towards higher orders-phonon processes

3.6.1 Previous discussions on four-phonon processes

In the Taylor expansion of the total energy (equation 2.2), one *naturally* supposes that the cubic term would be the leading of the non-harmonic ones [154, 155]. This intuitive hypothesis seems to be confirmed by the above-presented results on the LO-phonon lifetime dependence on temperature in Silicon (section (3.4.4)).

Yet, Silicon appears to be an exception: typically from 200 K for most materials studied with first principles calculations [104], an increasing divergence is observed between theoretical and experimental data that can reach 100% at 300 K, although it is important to note that the measured dependence on temperature is very dependent on the used experimental method. Assuming a non-negligible contribution of fourth-order (and greater) phonon scattering is then a legitimate hypothesis to explain this disparity. The development of conceptual tools to probe this mechanism turns nevertheless to be a complicated task: as a matter of fact, the number of publications having dealt with this issue is very

low. In addition, it is important to note that the observed discrepancy might be, in some cases, an artifact of taking anharmonic tensors as constant scalar values, as it is to be made explicit, and as it looks to be the case for instance between 200 K and 300 K in figure 3.2 for *AlAs* and *InP* where such an assumption was used.

In an essential article on the topic, M. Balkanski and co-workers [156] legitimated the necessity to take into account four-phonon processes, claiming that acoustic phonons absorption rate takes an increasing importance at high temperature because of their finite Bose-Einstein population number. Within the constant anharmonic tensors approximation for both third- and fourth-orders, they showed that an excellent fit of the LO-phonon lifetime dependence on temperature can be achieved in Silicon, the correction being effective from 200 K to 1200 K. The method was also used by G. P. Strivastava to achieve up to more than 1000 K fit on group-III Nitrides [126]. On the contrary, the results displayed in this work, in section (3.4.4), tends to conjure up that including third-order processes only is sufficient in Silicon to reproduce up to 800 K the experimental measurement, with no *ad hoc* assumption on the asymptotic value at 0 K. This suggests that the discrepancy in this case is caused by third-order taking anharmonic tensor as a constant scalar value. A. Debernardi also observed a divergence in III-V semiconductors, but using a third-order anharmonic tensor calculated *ab initio* within Density Functional Perturbation Theory [104]. In a more recent paper [137], he showed that, indeed, a fourth-order correction (computed by derivation through finite differences of the third-order tensor) allows a better agreement above 200K, and in particular, for the two above-mentioned cases, *AlAs* and *InP*. Unlike the case of *Si*, the necessity to include fourth-order processes in these materials does not seem to be a methodological artifact. It is worth noting that this correction induces no change in the asymptotic value at 0 K, which in all treated systems remains well reproduced within third-order interactions. This work turned also out to validate the intuitive feeling according to which fourth-order processes have a lower weight than third-order in the rate integral, since their contribution is calculated to be one order of magnitude lower for *AlAs* and *InP*, and even smaller for *GaAs* and *GaP*.

One may argue, though, that these considerations are of small importance from a hot-carrier solar cell point of view since it is not expected to work high above room temperature, and that third order seems to have always proven its efficiency up to room temperature. But this issue can however be expected to have a significant relevance in the peculiar case of *SiSn*, since the third-order conservation relations (2.14) and (2.15) are fulfilled in a very small reciprocal space volume, and higher-order terms may have a non-negligible weight in the rate integral, even at low temperature.

3.6.2 Estimation of the four-phonon processes contribution

In the same spirit of the third-order derivation of section (3.2.1), the fourth-order matrix element would take the form:

$$\begin{aligned}
V \begin{pmatrix} \mathbf{0} & \mathbf{q}_2 & \mathbf{q}_3 & \mathbf{q}_4 \\ LO & s_2 & s_3 & s_4 \end{pmatrix} &= \sum_{\substack{I,J,K,L \\ \alpha,\beta,\gamma,\delta}} \left(\frac{\hbar^4}{16NM_I M_J M_K M_L \omega^{LO}(\mathbf{0}) \omega^{s_2}(\mathbf{q}_2) \omega^{s_3}(\mathbf{q}_3) \omega^{s_4}(\mathbf{q}_4)} \right)^{\frac{1}{2}} \\
&\times \left[\sum_{l',l'',l'''} \frac{\partial^4 E_{tot}}{\partial u_{I,\alpha}^{l'} \partial u_{J,\beta}^{l''} \partial u_{K,\gamma}^{l'''} \partial u_{L,\delta}^{l''''}} e^{i(\mathbf{q}_2 \cdot \mathbf{R}^{l'} + \mathbf{q}_3 \cdot \mathbf{R}^{l''} + \mathbf{q}_4 \cdot \mathbf{R}^{l''''})} \right] \\
&e_{I,\alpha}(\mathbf{0}, LO) e_{J,\beta}(\mathbf{q}_2, s_2) e_{K,\gamma}(\mathbf{q}_3, s_3) e_{L,\delta}(\mathbf{q}_4, s_4)
\end{aligned} \tag{3.21}$$

where the factor between squared brackets is the fourth-order anharmonic tensor. This term is evaluated within the delicate approximation of a scalar anharmonic tensor, using the frozen phonon approach [157, 158]: the total energy is computed within DFT, at equilibrium and for a displaced atom corresponding to an LO-mode in the [111] direction (see appendix G). The found coupling constant is $96 \text{ eV} \cdot \text{\AA}^{-4}$, which is of the same order of magnitude than for Silicon ($135 \text{ eV} \cdot \text{\AA}^{-4}$). Once again, this represents a rough approximation, since it is known to be \mathbf{q} -dependent, and, in particular, the weight of the channels involving a near-zone centrer optic phonon was demonstrated to decrease linearly with its wavevector [104]. Hence, the final result must not be taken as anything but an order of magnitude of the fourth-order correction. The sum is performed on all three-phonon final states fulfilling energy and momentum conservation rules to reach the related scattering time τ_4 . Considering that the decays either in three or four phonons are independent, the total lifetime is calculated via the Matthiessen's rule [102]:

$$\frac{1}{\tau_{tot}} = \frac{1}{\tau_3} + \frac{1}{\tau_4} \tag{3.22}$$

where τ_3 is the lifetime through a three phonon process. The results are displayed on figure 3.10, for a zone center LO-phonon. The four-phonon processes are found to have a significant contribution at any temperature, although it does *not* change the order of magnitude of the lifetime computed considering only three-phonon processes (see table 3.2). Above 300K , the latter appears to have a lower influence than the four-phonon decays. This is explained by the increasing weight of the four-phonon processes that include, in addition to the LO-phonon, the annihilation of already existing acoustic phonons (for instance, referring to section (3.2.1), an $a_{LO}(\mathbf{0})a_{LA}(\mathbf{q}_2)a_{s_3}^\dagger(-\mathbf{q}_3)a_{s_4}^\dagger(\mathbf{q}_4)$ process), whose occupation number increases with the temperature. Through the Matthiessen's rule, it is obvious that the relevance of the four-phonon correction is dependent on the decay rate through three-phonon processes only: it does not bring, for instance, any significant correction in the case of Silicon. These results on SiSn, an archetype of an *a priori*

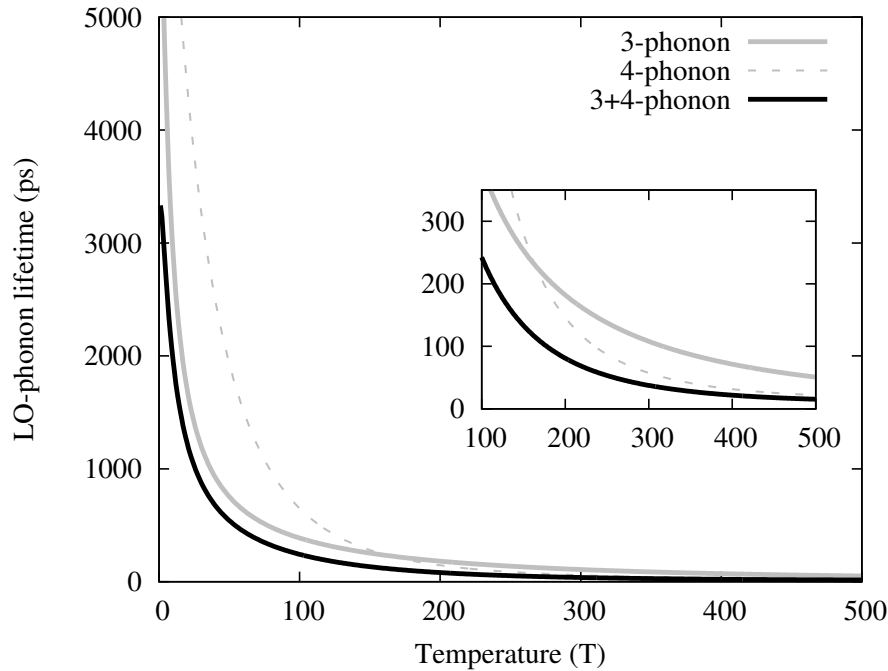


Figure 3.10: LO-phonon lifetime in SiSn considering three-phonon processes (grey solid line), four-phonon processes (grey dashed line), and both (black solid line).

Temperature (K)	τ_3	τ_4	τ_{tot}
200	182	146	81
300	108	57	38
400	71	32	22
500	51	22	15

Table 3.2: Particular LO-phonon lifetime in *SiSn* at particular temperatures, considering three- or four-phonon processes only (τ_3 and τ_4 respectively), or both contributions (τ_{tot}). All values are in picoseconds.

good candidate from a phononic band structure point of view, although based on a crude approximation, rises the question of the possibility to ever find a material exhibiting a lifetime of the order of 100 *ps* above room temperature.

3.6.3 Consecutive three-phonon processes

In a recent study, A. Dyson and B. K. Ridley [159] claimed that, in a two-phonon decay, the bare one-step phonon lifetime might be different from the one measured experimentally if the two final phonons have themselves a lifetime of the same order of magnitude than the initial phonon: in this case, an effective lifetime of the following form would be relevant:

$$\tau^* = \tau(1 + B) = \tau(1 + A_0)[(\bar{n}_2 - n_0)\tau_1 + (\bar{n}_1 - n_0)\tau_2] \quad (3.23)$$

where τ is the bare phonon lifetime in a three-phonon process, $(\tau)^{-1} = A_0(1 + \bar{n}_1 + \bar{n}_2)$, \bar{n}_1 and \bar{n}_2 are the Bose-Einstein occupation number at thermodynamic equilibrium of the two final phonons of the first decay. The authors stated that for a small deviation from the latter, the correction B must be positive.

Determining whether or not it brings substantial changes in the previous results in SiSn requires to compute the lifetime of the two final phonons. Considering that the Ridley channels contribute very little to the total rate in this case, we focus on the Klemens states decay (figure 3.11 and 3.12). The two final LA-phonon are close to the zone edge,

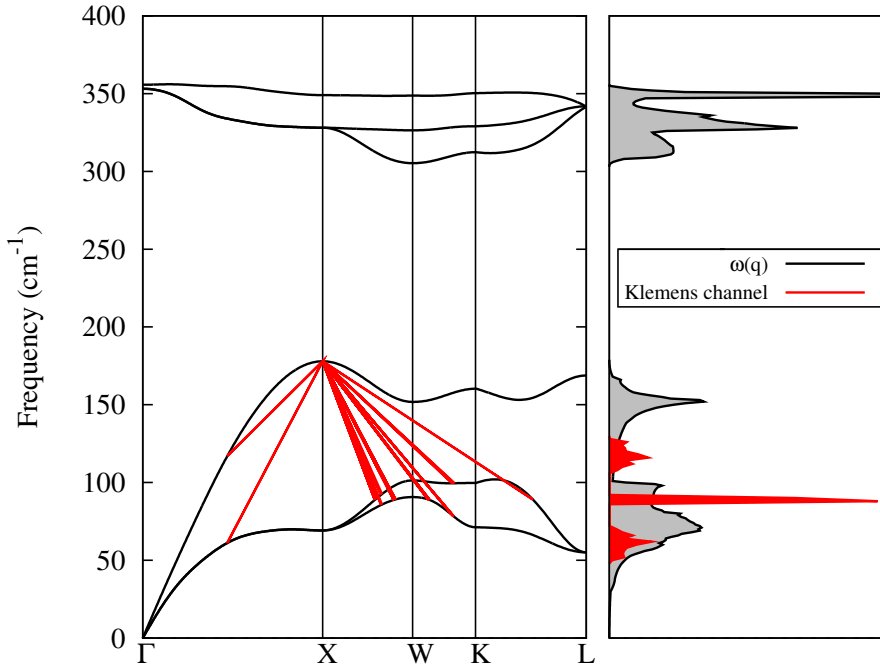


Figure 3.11: 2D picture of the two-phonon final states of the X -zone-edge LA-phonon decay through Umklapp processes in SiSn.

so that the near-zone-centre approximation used in section (3.5.2) to compute the third-order anharmonic tensor is not reasonable anymore. Oppositely, thanks to band folding, the choice of an appropriate supercell would make these states *appear at the zone-centre*. This band folding introduces ghost channels but, as said in (3.2.3), working within DFPT prevents them from artificially contributing to the decay rate. A third-order calculation is thus performed, for a four-atom tetragonal cell, using the same computational criteria as the one used in the Zinc-Blende structure, the only exception being the \mathbf{q} -points mesh, set to $18 \times 25 \times 25$ to respect reciprocal space commensuration. As can be seen on figures 3.11 and 3.12, the large number of final states allows to work within the zone-centre approximation, and the dependence of the LA-phonons lifetime on their wavevector can be assumed to be negligible. In addition, it should be mentioned that available two-phonon final states can be found for the LA-phonons only by taking into account Umklapp

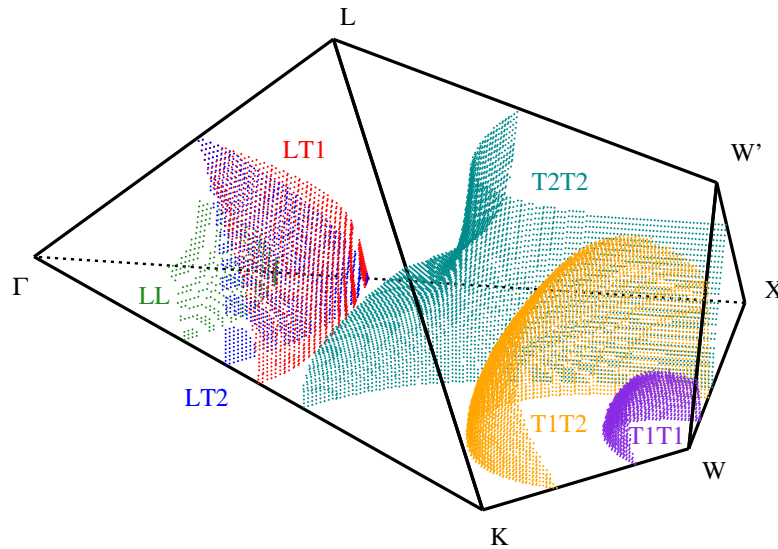


Figure 3.12: 3D pictures of the two-phonon final states of the X -zone-edge LA-phonon decay through Umklapp processes in SiSn. The channels classification is as follows: LL : LA+LA, $LT1$: LA+TA1, $LT2$: LA+TA2, $T1T1$: TA1+TA1, $T1T2$: TA1+TA2, $T2T2$: TA2+TA2.

processes [102], so that the momentum conservation rule writes:

$$\mathbf{q}_2 + \mathbf{q}_3 + \mathbf{Q} = \mathbf{0} \quad (3.24)$$

with $\mathbf{Q} = (1, 0, 0)$. Umklapp processes have not been included so far, consistently with L. Paulatto and co-workers results [124] showing that they do not contribute to the decay of a phonon having a wavevector close to $\mathbf{0}$.

The LA-lifetime is found to be 1.3 ps in the low temperature limit, and 0.2 ps at 300 K. In such conditions, the correction in the effective lifetime described above is infinitely small. This is consistent with A. Dyson and B. K. Ridley's analysis according to which Klemens final states would have a negligible contribution compared to the Ridley final states because of the lower sum of Bose-Einstein occupation numbers in the latter. However, and once again, the Ridley channels contribute so little in the first place to the total two-phonon decay rate in the case of SiSn that they cannot be relevantly included in this two-step decay.

3.6.4 Crystal symmetry and higher-order anharmonic tensors

As said previously, the *ab initio* determination of the anharmonic contributions is a very demanding task, and no implementation exists above third order. However, in the

spirit of finding at least an approximate expression that may work as a small corrective perturbation, it is worth noting that all the elements of the n^{th} -order anharmonic tensor are in theory not required, depending on the crystal symmetry. We denote this tensor element $\phi_{\alpha_1 \dots \alpha_n}^{I_1 l_1 \dots I_n l_n}$ as:

$$\phi_{\alpha_1 \dots \alpha_n}^{I_1 l_1 \dots I_n l_n} = \frac{\partial^n E_{tot}}{\partial u_{\alpha_1}^{I_1 l_1} \dots \partial u_{\alpha_n}^{I_n l_n}} \quad (3.25)$$

where I, l, α label the atom, unit cell and coordinate. It was demonstrated by G. Leibfried

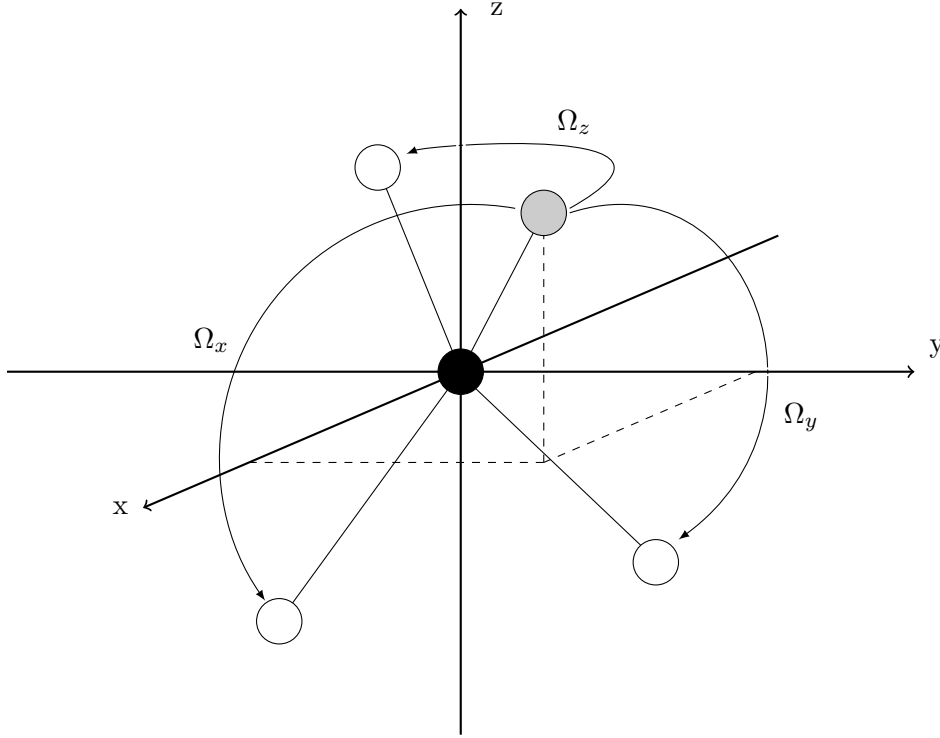


Figure 3.13: Invariant rotation matrices Ω in the tetrahedral environment. The index (x,y,z) stands for the axis around which the rotation is performed.

and W. Ludwig [160] that it has to be invariant under symmetry operations that depend on the crystal structure, in particular:

$$\sum_{\alpha'_1 \dots \alpha'_n} \phi_{\alpha'_1 \dots \alpha'_n}^{I_1 l_1 \dots I_n l_n} \Omega_{\alpha'_1 \alpha_1} \dots \Omega_{\alpha'_n \alpha_n} = \phi_{\alpha_1 \dots \alpha_n}^{I_1 l_1 \dots I_n l_n} \quad (3.26)$$

where $\Omega_{\alpha'_i \alpha_i}$ are the elements of a set of rotation matrices that transform the lattice into itself. The primed indices are the coordinates into which the unprimed coordinates are transformed. If we limit ourselves for now to the Zinc-Blende case, three rotation matrices ensue from the atomic tetrahedral environment, and write, as labelled in figure 3.13:

$$\Omega_x = \begin{pmatrix} 1 & 0 & 0 \\ 0 & -1 & 0 \\ 0 & 0 & -1 \end{pmatrix}; \quad \Omega_y = \begin{pmatrix} -1 & 0 & 0 \\ 0 & 1 & 0 \\ 0 & 0 & -1 \end{pmatrix}; \quad \Omega_z = \begin{pmatrix} -1 & 0 & 0 \\ 0 & -1 & 0 \\ 0 & 0 & 1 \end{pmatrix} \quad (3.27)$$

The eventual first condition leading to non zero matrix elements is $\alpha'_i = \alpha_i$, so that the sum is reduced to one single term:

$$\phi_{\alpha_1 \dots \alpha_n}^{I_1 l_1 \dots I_n l_n} \Omega_{\alpha_1 \alpha_1} \dots \Omega_{\alpha_n \alpha_n} = \phi_{\alpha_1 \dots \alpha_n}^{I_1 l_1 \dots I_n l_n} \quad (3.28)$$

Non-trivial solutions ($\phi_{\alpha_1 \dots \alpha_n}^{I_1 l_1 \dots I_n l_n} \neq 0$) are given for the product of the $\Omega_{\alpha_i \alpha_i}$ being equal to 1. Depending on the rotation matrix considered, these products are given in table 3.3 (n_x , n_y and n_z being the number of times x, y and z appear in the string $\alpha'_1 \dots \alpha'_n$), followed by the obvious (second) condition that leads to non-zero potential matrix element in each case. The possible $\{ n_x, n_y, n_z \}$ combinations depend on the derivative order n , since

	$\Omega_{\alpha_i \alpha_i}$ product	Unity condition
Ω_x	$(-1)^{n_y} (-1)^{n_z}$	$n_y + n_z$ even
Ω_y	$(-1)^{n_x} (-1)^{n_z}$	$n_x + n_z$ even
Ω_z	$(-1)^{n_x} (-1)^{n_y}$	$n_x + n_y$ even

Table 3.3: Lattice potential rotational invariance conditions for the tetrahedral environment. n_x , n_y and n_z are the number of times x, y and z appear in the string $\alpha'_1 \dots \alpha'_n$ of equation (3.26).

indeed $0 \leq n_x, n_y, n_z \leq n$, and $n_x + n_y + n_z = n$. For $n = 3$, the only solution is $\{ n_x = 1, n_y = 1, n_z = 1 \}$, while for $n = 4$ there are two, $\{ n_x = 4, n_y = 0, n_z = 0 \}$ and $\{ n_x = 2, n_y = 2, n_z = 0 \}$ (in accordance with what was found elsewhere by D. Vanderbilt and co-workers [157]), not to mention all the index permutations. This matrix analysis was used for instance to study the flexural phonons contribution to the three-phonon processes in Graphene [161], which reveals that only an even number of such phonons can be involved.

The required number of matrix element from an analytical point of view is indeed very low, and since it depends on the crystal structure, may be approximated in highly symmetrical directions [157]. In addition, what takes shape here is an inverse problem: *are there sets of rotational matrices, hence particular crystal structures, that induce a non-fulfillment of the invariance relations for $n \geq 4$?* A large phonon lifetime would be expected in such a crystal. However, this condition being not fulfilled in such a highly symmetric case as Zinc-Blende structure tends to suggest that there is no positive answer to this question.

3.7 Conclusions on LO phonon lifetime calculations for HCSC

Basic elements on phonon lifetime formalism and methodological details within Density Functional Perturbation Theory were recalled with Silicon as a case study.

3.7.1 SiSn features as references

This method was used to study the LO-phonon lifetime in *SiSn* in the Zinc-Blende crystal structure. Its stiff dependence on the initial LO-phonon wavevector was pointed

out and is a fundamentally new behaviour and is explained by the particular location of the two-phonon final states in the first Brillouin zone. As a consequence, Klemens channels might be acceptable in the aim of a more than 100 *ps* LO-phonon lifetime at 300K, provided the final states are located at the Brillouin-zone edges, and provided also the Ridley states lie close to the Brillouin zone centre. A subsequent analysis on the dependence of the two-phonon density variation upon the initial wavevector is required in each individual case to turn or not the *might be* into *are*. These features are, although bounded to, more accurate targets than simply macroscopic characters such as the atomic mass ratio or the electronegativity difference.

3.7.2 Limitations

This study also revealed that, despite its providing a full understanding of the mechanisms at stake, Density Functional Perturbation Theory may not be the most suitable method for routinely investigation of phonon lifetime in more than few atoms systems because of its strong computational time dependence on the number of valence electron within the pseudopotential method. Moreover, up to December 2014, no study was published on more-than-two-atom per cell systems [144, 104, 124].

If no elegant solution of the inverse problem derived in section (3.6.4) is found, it has been demonstrated why a detailed calculation is required to predict phonon lifetime in new materials. In addition, the borderline case of SiSn highlights the necessity of including more than three-phonon processes in the materials of interest for hot-carrier solar cell absorbers. This brings another severe limitation to the study of phonon lifetime since no fully *ab initio* derivation is nowadays available for this aim, and as it has been shown that even approximate higher-order corrections are difficult to handle. Yet, the approximate fourth-order correction already suggests that LO-phonon lifetime of the order of ~ 100 *ps* might be unlikely to reach in practice.

3.7.3 Towards other ways to hinder carrier cooling

As was pointed out in section (2.6.3), there is no reason to think, from our understanding, that the materials in which a hot-carrier effect was measured exhibit a long LO-phonon lifetime: this latter condition is once again, although *sufficient, not necessary* in a hot-carrier solar cell absorber.

The reason for low thermalisation rate in these materials might hence not be found in the phonon-phonon interaction, but one process ahead, in the carrier-phonon interaction. This will be the topic of the next chapter.

Chapter 4

Electron-phonon interaction

Contents

4.1	Dimensionality issue	88
4.1.1	Electron cooling in superlattices	88
4.1.2	Self-induced electric field and intraband scattering	89
4.1.3	[InAs] _n -[GaAs] _n	89
4.2	Directionally dependent electron-phonon interaction model . .	89
4.2.1	Electron-phonon coupling strength	90
4.2.2	Electron wave function	92
4.2.3	Electron evolution equations	93
4.3	Full-band cascade: practical implementation	93
4.3.1	Electronic band	93
4.3.2	Phonon polar field	94
4.3.3	Electronic cascade	94
4.3.4	Validation: bulk case	95
4.4	Effects of the superlattice size	96
4.4.1	Effect on the electric field	97
4.4.2	Effect on the electron-phonon interaction dimensionality	100
4.5	Conclusions on the electron-phonon interaction in superlattices	103
4.5.1	Approach and results	103
4.5.2	Approximations and subsequent limitations	103
4.5.3	Perspective on the hot-carrier effect in superlattices	103

4.1 Dimensionality issue

The energy loss rate reduction has been experimentally found to be systematically lower in 2D structure than in bulk materials, and, in the former, dependent on the electronic density only above a critical value of $\tilde{n}_c \approx 0.5 - 1.0 \cdot 10^{18} \text{cm}^{-3}$ (section 1.4.1.1). A distinction is made here between superlattices (thickness $\lesssim 40 \text{ \AA}$) and quantum wells (thickness $\gtrsim 40 \text{ \AA}$). This classification is justified, for instance in A. Nozik's review on hot carriers in quantum wells and quantum dots [14], as it corresponds to the thickness below which electronic bands throughout the materials allow carriers delocalisation, whereas quasi-bulk structures appear above in each sub-crystal. This critical thickness is of course dependent on the material atomic nature, and the value 40 \AA is no more than an order of magnitude. The dependence of the energy loss rate reduction in the superlattice range is not clear; in particular, the necessity to work within high concentration levels is not established [67, 14].

Multiple quantum wells no thicker than 10 nm were pointed out as candidates for hot-carrier solar cell absorber due to a combination of a low thermalisation coefficient and a short distance to travel for the carriers to the energy selective contacts [78, 79]. As their width belongs to this range, and because they remain less studied than quantum wells, superlattices are of potential interest from a hot-carrier solar cell point of view. The shortness of the thickness at stake allows first principle investigations, and makes affordable the reaching of a detailed picture of electronic scale phenomena, namely, in the present case, the electronic cooling. The aim here is not to reach a complete dynamical picture of a cooling hot carrier population [78], but rather to study the bare electron-phonon interaction in the limit of extremely thin superlattices, assuming no renormalisation of the quasi-particles self energy due to strong coupling effects [76].

4.1.1 Electron cooling in superlattices

In order to determine whether or not the superlattice size has an impact on electron cooling, a simulation of this latter process is performed for several superlattice thicknesses. A hot electron population is photogenerated by a photon beam, from the highest valence band to the first conduction band. In order to determine whether or not the superlattice size has an impact on electron cooling. No *ad hoc* assumption is made on the electronic and phononic band structures: as said previously, the relatively small size of the systems allows a full-band calculation of both. In particular, an *ab initio* calculation of the dispersion relation allows to consider the actual band folding and the accurate curvature modification. This is of particular importance since the exchange phonon energy is of the order of the electronic band derivative with respect to the electronic wavevector \mathbf{k} .

How dimensionality affects the electron-phonon interaction on this scale is however at this point still an open question, and a pragmatic and simple way to model it in superlattices has to be set.

4.1.2 Self-induced electric field and intraband scattering

It has been recalled that, below the intervalley energy threshold, the photoexcited hot electrons cool through intraband scattering, emitting LO-phonons (section 1.2). The electric field induced by the out-of-phase vibration of oppositely charged atoms (section 2.3.1.2) is responsible for the dominance of this particular electron-phonon interaction over the coupling with other modes [14].

All the materials studied in the previous chapters have in common to exhibit only one LO-phonon mode, i.e for any \mathbf{q} -vector close to $\mathbf{0}$, one inner cell out-of-phase atomic vibration mode whose polarisation is parallel to the direction of propagation. But the number of these phonon modes, so the number of modes with which an electron might couple to cool via intraband scattering, grows with the number of atoms (N_{at}) as $N_{at} - 1$. Depending on their eigenvector components, these modes may not induce an electric field of the same amplitude, so that the coupling between electrons and each of these phonons may be of different strength.

In addition, as the materials were in the Zinc-Blende crystal structure, the electric field was isotropic in the vicinity of the Brillouin zone centre. In the case of superlattices, or more generally nanostructured materials, symmetry breaking must be responsible for the electric field associated to each LO-mode to be anisotropic.

Finally, depending on the crystal structure, the electronic band structure is also not isotropic, even at the very bottom of the Γ -valley. This may have an impact on the phonons the electrons are allowed to couple with in order to fulfill energy and momentum conservation rules.

These are the key parameters our model must correctly include for the simplest study on the impact of dimensionality on the electronic cooling. How to compute them will be the centre of section (4.2).

4.1.3 $[\text{InAs}]_n$ - $[\text{GaAs}]_n$

InAs and *GaAs* are two III-V semiconductors that match the electronic criteria listed in section (1.4.2). *InAs*, in particular, has a deep Γ -valley (a high intervalley energy threshold) of more than 1 eV [162]. The chosen material is the superlattice $[\text{InAs}]_n$ - $[\text{GaAs}]_n$, thereafter referred to as $[\text{InGaAs}]_n$, and is simply a stack of n layers of *GaAs* on n layers of *InAs*. As an example, the unit cell is depicted in figure 4.1 for $n = 4$. The number of LO-modes in this type of structure grows with n as $4n - 1$.

4.2 Directionally dependent electron-phonon interaction model

The aim of this section is to discriminate the phonons, that photoexcited carriers are most likely to couple with, in the cooling process. The interaction rate must *allow* a dependence on dimensionality to appear. Following the Fermi Golden Rule, the transition

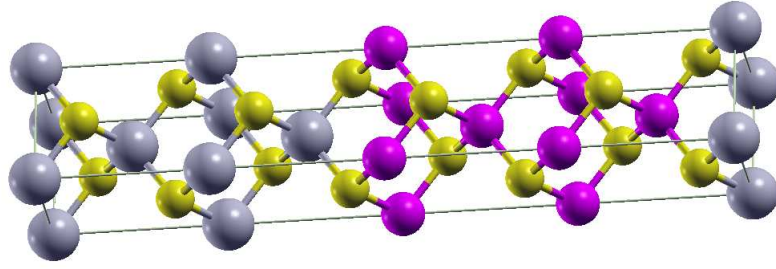


Figure 4.1: Crystal unit cell of $[InGaAs]_4$. In, Ga and As atoms are coloured in grey, pink and yellow respectively.

rate probability from one initial state i to the final state f is given by:

$$\Gamma = \frac{2\pi}{\hbar} \sum_f |\langle \Psi_f | M | \Psi_i \rangle|^2 \delta(E_f - E_i) \quad (4.1)$$

The matrix element and the electronic wavefunction Ψ is to be defined in the following subsections.

4.2.1 Electron-phonon coupling strength

Here is addressed the possibility to extend two well known bulk approaches for electron-LO-phonon interaction to the superlattice cases. The common starting point between the two is the existence of an electric field \mathbf{E} created by an LO-phonon.

4.2.1.1 The electrostatics picture

The definition of the electric induction writes:

$$\mathbf{D} = \mathbf{E} + 4\pi\mathbf{P} \quad (4.2)$$

where \mathbf{P} is the electric polarisation. Assuming no free charge in the system, and no magnetic effects, first and third reciprocal space Maxwell equations take the form:

$$i\mathbf{q} \cdot \mathbf{D} = 0 \quad (4.3)$$

$$\mathbf{q} \times \mathbf{E} = 0 \quad (4.4)$$

\mathbf{q} being the wavevector of the electromagnetic wave, that in our case is a LO-phonon making oppositely charged atoms oscillate. As $\mathbf{q} \neq \mathbf{0}$, equation (4.3) immediately leads to $\mathbf{E} = -4\pi\mathbf{P}$. The two assumptions differ in the choice of an appropriate polarisation.

4.2.1.2 Fröhlich coupling constant

Fröhlich approach [29] consists in setting the polarisation proportional to the atomic displacement:

$$\mathbf{P}_{\mathbf{q}} = eU\mathbf{u}_{\mathbf{q}} \quad (4.5)$$

where U is an *effective* atomic charge that accounts for electric screening of the ionic polarisation, as [163]:

$$U^2 = \frac{n\omega_{LO}^2}{4\pi} \left(\frac{1}{\epsilon_{\infty}} - \frac{1}{\epsilon_0} \right) \quad (4.6)$$

where the high frequency (ϵ_{∞}) and low frequency (ϵ_0) dielectric tensors are taken as scalar values. The subsequent matrix element M is expressed with the *Fröhlich coupling constant* α_F :

$$M^2 = \frac{4\pi\alpha_F\hbar(\hbar\omega_{LO})^{3/2}}{\sqrt{2m}} \quad (4.7)$$

$$\alpha_F = \frac{e^2}{\hbar} \left(\frac{m}{2\hbar\omega_{LO}} \right)^{1/2} \left(\frac{1}{\epsilon_{\infty}} - \frac{1}{\epsilon_0} \right) \quad (4.8)$$

This expression, as it was originally formulated, does not allow to study a directional dependence of the electron-phonon coupling. Expecting this interaction not to be isotropic in a superlattice, the sole study of this coupling constant is not sufficient. However, it may be stated that a tensorial form of equation (4.5) could be found by substituting the scalar part between parenthesis by a suitable vectorial expression such as $\left(\frac{1}{\mathbf{q}\cdot\epsilon_{\infty}\cdot\mathbf{q}} - \frac{1}{\mathbf{q}\cdot\epsilon_0\cdot\mathbf{q}} \right)$. Reaching an accurate value of the low frequency dielectric tensor is possible with the use of Time Dependent Density Functional Theory [164]. The assumption of an effective dielectric tensor and the use of ϵ_0 can be avoided when having the knowledge of the exact atomic displacement induced by a particular mode and the effective charges carried by the atoms, which Density Functional Perturbation theory alone allows.

4.2.1.3 Born-Huang effective charges and electric field

In what we will call the *Born and Huang approach*, the idea is rather to decouple, at the beginning, the electronic and ionic contribution to the polarisation, \mathbf{P}_{el} and \mathbf{P}_{ion} , as [165]:

$$\mathbf{P}_{el} = \chi_{\infty}\mathbf{E} \quad (4.9)$$

$$\mathbf{P}_{ion} = \frac{4\pi e}{\Omega} \sum_I \mathbf{Z}_I^* \mathbf{u}_I \quad (4.10)$$

where χ_{∞} is the electronic susceptibility tensor, that is assumed \mathbf{q} -independent considering the materials of interest [100]. \mathbf{Z}_I^* is called the Born-Huang effective charge [26] and is the bare charge (i.e. in the absence of field) carried by atom I . Finally, \mathbf{u}_I is the displacement vector of atom I , which in the case of no external forces is simply the eigenvector related

to a specific phonon mode. The induction can thus be written:

$$\mathbf{D} = \epsilon_\infty \mathbf{E} + \frac{4\pi e}{\Omega} \sum_I \mathbf{Z}_I^* \mathbf{u}_I \quad (4.11)$$

with $\epsilon_\infty = 1 + 4\pi\chi_\infty$. Making use of equations (4.3) and (4.4), an expression is reached for the electric field [99]:

$$\mathbf{E} = -\frac{4\pi e}{\Omega} \sum_I \frac{\mathbf{q}(\mathbf{q} \cdot \mathbf{Z}_I^* \mathbf{u}_I)}{\mathbf{q} \cdot \epsilon_\infty \cdot \mathbf{q}} \quad (4.12)$$

The elegance of this formulation is to carry an explicit directional dependence on \mathbf{q} , both in the ionic contribution (numerator) and in the electronic screening (denominator). In addition, using the appropriate eigenvector \mathbf{u} , it is possible to calculate \mathbf{E} for any phonon mode. The matrix element in the interaction rate is hence just defined proportional to the \mathbf{q} -dependent electric field amplitude $\mathbf{E} \equiv |\mathbf{E}|$. Born effective charges and the dielectric tensor are computed *ab initio* within DPFT [113, 165]. The agreement between the experimental and calculated LO-TO splitting witnessed in chapter 2 (section (2.3.1.2), figures 2.6 and 2.7) makes trustable the computed values for any III-V material.

4.2.2 Electron wave function

It is very convenient, and still relevant in the superlattice regime, to assume the electronic wave functions to be Bloch functions [98]:

$$|\Psi_{n,\mathbf{k}}\rangle = e^{i\mathbf{k}\cdot\mathbf{r}} |\mathbf{u}_{n,\mathbf{k}}\rangle \quad (4.13)$$

where n is the branch label and \mathbf{k} is the electronic wavevector, and $\mathbf{u}_{n,\mathbf{k}}$ a periodic function having the lattice periodicity. Hence, the overlap factor in the Fermi Golden Rule equation (4.1) can be written:

$$|\langle \Psi_f | M | \Psi_i \rangle|^2 = \left| \langle e^{i(\mathbf{k}-\mathbf{q})\cdot\mathbf{r}} | M | e^{i\mathbf{k}\cdot\mathbf{r}} \rangle \right|^2 \cdot I_{Bloch}^2(\mathbf{k} - \mathbf{q}, \mathbf{k}) \quad (4.14)$$

where $I_{Bloch}^2(\mathbf{k} - \mathbf{q}, \mathbf{k}) = |\langle \mathbf{u}_{n',\mathbf{k}-\mathbf{q}} | \mathbf{u}_{n,\mathbf{k}} \rangle|^2$, the overlap of the Bloch functions periodic parts. Assuming the electron always remains on the same conduction band (the lowest one), n' is set equal to n . Although it is tantalising to assume that this overlap factor has always to be of the order of 1, it was shown by E. Tea [48] that this is a crude approximation, except for electrons at the very the bottom of the Γ -valley, and that the expression given by W. Fawcett [166] is much more relevant:

$$I_{Bloch}^2(\mathbf{k}, \mathbf{k}') = \frac{(\sqrt{1 + \alpha E_{\mathbf{k}}}\sqrt{1 + \alpha E_{\mathbf{k}'}} + \alpha\sqrt{E_{\mathbf{k}}E_{\mathbf{k}'}} \cos\theta_{\mathbf{k},\mathbf{k}'})^2}{(1 + 2\alpha E_{\mathbf{k}})(1 + 2\alpha E_{\mathbf{k}'})} \quad (4.15)$$

where \mathbf{k}' in our particular case is $\mathbf{k} - \mathbf{q}$, $\theta_{\mathbf{k},\mathbf{k}'}$ is the angle between wavevectors \mathbf{k} and \mathbf{k}' , and α is the non-parabolicity coefficient.

4.2.3 Electron evolution equations

The electronic transition from one reciprocal position $\{E_i, kx_i, ky_i, kz_i\}$ (labelled i) to another $\{E_{i+1}, kx_{i+1}, ky_{i+1}, kz_{i+1}\}$ ($i+1$) must obviously follow energy and momentum conservation rules (equations (4.16) and (4.17)). A deterministic picture is adopted by the addition of a third conservation rule (equation (4.18)): among the multiple possible final states fulfilling energy and momentum conservation rules, only the one that corresponds to the highest interaction rate is retained at each iteration.

$$\mathbf{k}^{i+1} + \mathbf{q} = \mathbf{k}^i \quad (4.16)$$

$$E^{i+1} + \hbar\omega(\mathbf{q}) = E^i \quad (4.17)$$

$$\Gamma_{i \rightarrow i+1} - \max(\Gamma_{i \rightarrow i'+1}) = 0 \quad (4.18)$$

This model differs from a Monte Carlo method since the path from one electronic position to the bottom of the conduction band is unique within equation (4.18) assumption: electrons follow an extremal path in the \mathbf{k} -space, and it has been verified that choosing a Gaussian form instead of a Dirac form for this equation introduces no change in the results.

4.3 Full-band cascade: practical implementation

How to compute the phonon band structure on an arbitrary fine mesh has been recalled in chapter 2. Taking bulk GaAs and InAs as illustrating examples, a brief computational methodology is given concerning the required electronic energy dispersion relation $E(\mathbf{k})$, and the mode-dependent electric field dispersion relation $\mathbf{E}(\mathbf{q})$.

4.3.1 Electronic band

How to choose the appropriate reciprocal mesh is not trivial since the electronic and phononic dispersions in energy are very different. Considering the example of an electron photoexcited just below the intervalley threshold, so around $1 \sim eV$, or $\sim 8000 \text{ cm}^{-1}$, above the conduction band minimum in InAs. The LO-phonon energy being $\sim 230 \text{ cm}^{-1}$, the number of cooling steps for such a hot electron would be of the order of 35. The hot electron would have an initial \mathbf{k} -vector whose norm would be of the order of $\sim 0.2 \cdot 10^{10} \text{ m}^{-1}$, which gives an average exchange wavevector of $\sim 5 \cdot 10^7 \text{ m}^{-1}$. Hence, a step of 10^7 m^{-1} ($\sim 0.1\%$ of the size of the Brillouin zone) is required for a trustable reproduction of the cooling steps.

Calculations were done within Density Functional Theory using the Projector Augmented Wave method (*PAW*) [167] as implemented in the VASP package [5]. Since an accurate description of the band structure is required, the HSE06 hybrid functional was chosen (details are displayed in appendix D). Wannier functions extrapolation [168, 169, 170]

was used to avoid the first principle computation of such a \mathbf{k} -space mesh: electronic bands, just as phonon bands, incidentally, are smooth functions of \mathbf{k} (\mathbf{q} , respectively), and such an extrapolation has proven to be very trustable [170]. The found gaps at high symmetry points are gathered in table 4.1 and 4.2 for GaAs and InAs respectively.

	$\Gamma_v^6 - \Gamma_c^6$	$\Gamma_v^6 - X_c^6$	$\Gamma_v^6 - L_c^6$
This work	1.35	2.10	1.74
Adachi	1.42	1.90	1.71

Table 4.1: Band parameter in GaAs. The comparison is made with S. Adachi's results [171].

	$\Gamma_v^6 - \Gamma_c^6$	$\Gamma_v^6 - X_c^6$	$\Gamma_v^6 - L_c^6$
This work	0.29	2.25	1.54
[171]	0.35	1.37	1.08
[172]	0.37	2.28	1.53

Table 4.2: Band parameters in InAs. The comparison is made with S. Adachi's [171] and J. R. Chelikowsky's results. A discussion on the discrepancy with [171] is given in appendix D.

4.3.2 Phonon polar field

Born effective charges \mathbf{Z}^* and dielectric tensor ϵ_∞ are computed within density functional perturbation theory (section (2.3)). In figure 4.2 is depicted the variation of the LO-phonon induced electric field norm, as defined by equation (4.12), as a function of the \mathbf{q} -vector in the vicinity of the zone center, for GaAs and InAs. As expected, the field amplitude is smaller in InAs than in GaAs, what is experimentally suggested (and found with DFPT) by the smaller LO-TO splitting in InAs than in GaAs. As expected also, considering the variation of the LO-TO-splitting variation in figure 2.4, \mathbf{E} is a decreasing function of \mathbf{q} , and this is a direct consequence of the phase evolution of the atomic displacement vector. From this sole point of view, one would expect the exchanged wavevector to be asymptotically close to $\mathbf{0}$ since the field takes its highest value. What prevent the electrons to behave so is the energy and momentum conservation rules, as electrons and phonons cannot just exchange energy.

4.3.3 Electronic cascade

The principle of the electronic cascade is illustrated in figure 4.3: an electron population is photogenerated, by a 6000 K black body-like photons beam, from the highest

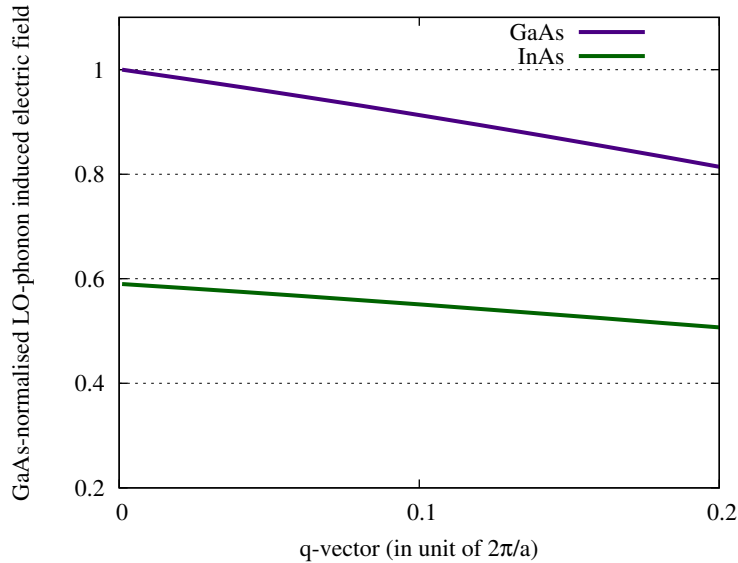


Figure 4.2: Electric field induced by the LO phonon mode along the $\Gamma - X$ direction in bulk GaAs and InAs. All values are normalised by $\mathbf{E}_{\mathbf{q}=\mathbf{0}}^{GaAs}$.

valence band (grey surface) to the lowest conduction band (coloured surface) to an initial energy-versus- \mathbf{k} position (black cross). The absorption coefficient is assumed to be energy-independent and equal to 1. A filter restricts the allowed energy of the incident photons in such a way that the excited carriers always remain below the intervalley energy threshold, so to focus on the intraband scattering. From this position, all final states satisfying conservation rules (4.16) and (4.17) are examined. The retained new position is the one that fulfills equation (4.18), i.e. corresponding to the highest rate:

$$\Gamma_{i \rightarrow i+1} = |\mathbf{E}|^2 \cdot I_{Bloch}^2(\mathbf{k}_i - \mathbf{q}_{i \rightarrow i+1}, \mathbf{k}_i) \delta(E_{i+1} - (E_i + \hbar\omega^{LO}(\mathbf{q}_{i \rightarrow i+1}))) \delta(\mathbf{k}_{i+1} - (\mathbf{k}_i + \mathbf{q}_{i \rightarrow i+1})) \quad (4.19)$$

This procedure is iterated, and the electrons then undergo a step-by-step cooling until they reach a minimum. We limit ourselves to the Γ -valley in direct band gap materials, so that this minimum is always the conduction band lowest energy point. A two-dimensional illustration of the cooling process is depicted in figure 4.3.

Statistics are performed on the emitted phonon wavevector \mathbf{q} , as well as on the angle of emission, on several thousands of cooling photogenerated electrons. The emission angles are labeled *in-plane* or *out-of-plane*, depending whether their dominant component belongs to the xy-plane or to the z-axis (i.e. the growing axis in the superlattice cases).

4.3.4 Validation: bulk case

As it is expected, an equal distribution of in-plane and out-of-plane emitted phonons is found in bulk GaAs and InAs. The $|\mathbf{q}|$ -resolved emission distribution for these two materials is depicted in figure 4.4. Concerning the peak position in GaAs, an excellent

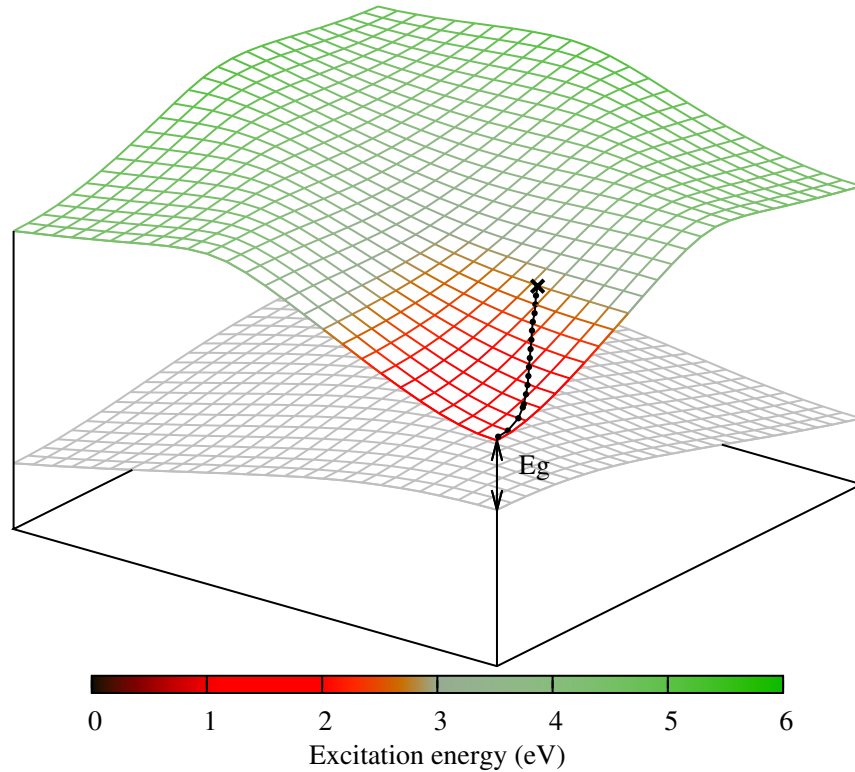


Figure 4.3: Two-dimensional picture of the electronic cooling implementation in GaAs (see text). The grey surface is the highest valence band, the coloured one is the lowest conduction band. The colour illustrates the required photon energy to promote an electron from the valence band to the conduction band at each point. Note that on this picture the space mesh variables have been reduced from $\{k_x, k_y, k_z\}$ to $\{k_x, k_y\}$, and that the actual energy surface is a function of *three* reciprocal coordinates. On this figure also, the mesh size is forty times larger than in the actual calculation, for clarity.

agreement is found with C. L. Collins and P. Y. Yu pioneer Monte Carlo work on hot-carrier cooling in this particular binary compound [24]. The shifted peak position for InAs compared to GaAs is a direct consequence of the stiffer band curvature in the Γ -valley.

4.4 Effects of the superlattice size

The cooling process described in (4.3.3) is set for $[\text{InGaAs}]_n$ superlattices. As the size of the stack grows with n as $0.6n$ (in nm), remaining in the superlattice range (~ 4 nm [14]) imposes *a priori* not to work with $n \gtrsim 7$. This statement is to be developed in the following.

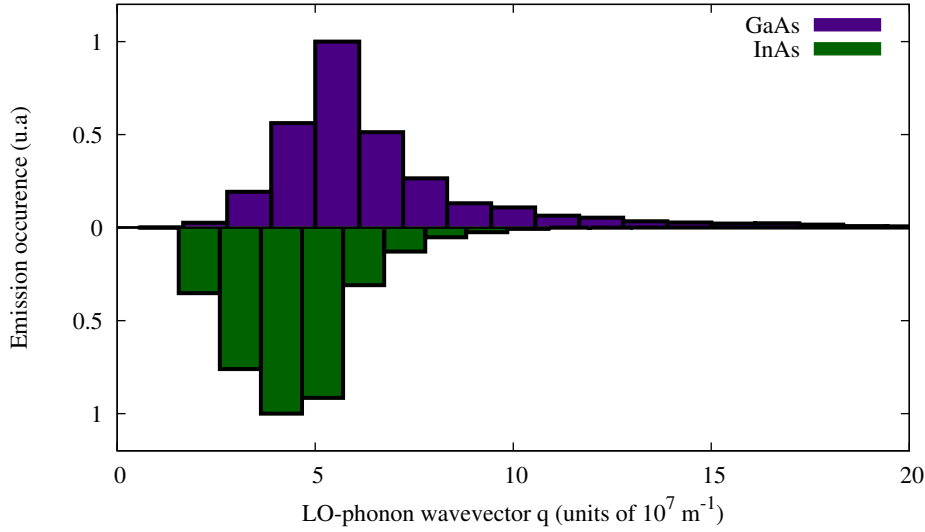


Figure 4.4: Emitted LO-phonon wavevector distribution in the cooling process for bulk GaAs and InAs.

4.4.1 Effect on the electric field

The influence of the confinement on the electric field along unequivalent directions is here investigated. We first discuss the definition of a reference in the in-plane direction (E_{\parallel}) to then compare the out-of-plane field with (E_{\perp}).

Reference setting

From $n = 1$ to 7, it appears that the phonon mode leading to the highest electric field corresponds to the highest energy branch, with \mathbf{q} belonging to the in-plane direction (E_{\parallel}). From an atomic displacement point of view, it is related to an out-of-phase vibration of all XAs ($X = In, Ga$) couples of atoms of the crystal. It can be reasonably assumed *a priori* that the eventual electric field has to be equal to the average of the bulk GaAs and InAs ones:

$$E_{th}^{[InGaAs]_n} = (E_{\parallel}^{GaAs} + E_{\parallel}^{InAs})/2 \quad (4.20)$$

For this reason, the in-plane electric field (E_{\parallel}) plotted in figure 4.5 is normalised by E_{th} and compared to unity. Up to $n = 6$, the deviation is lower than 4 %, and reaches 5.5 % for $n = 7$. Interestingly, the rough limit in width between superlattice and quantum well lies between $n = 6$ and $n = 7$, and, for $n \geq 8$, this particular phonon mode does not exist anymore: the highest electric fields are in these cases induced by *bulk like* modes, i.e. all $Ga - As$ ((respectively $In - As$) couples vibrating out-of-phase while all $In - As$ (respectively $Ga - As$) couples are fixed.

The conclusion is that above $n = 6 - 7$, the material is no longer a superlattice but a multi quantum-well, both pseudo-bulk regions having localised electronic and phononic band structures. In this regime, the real-space localisation of the photogenerated electron

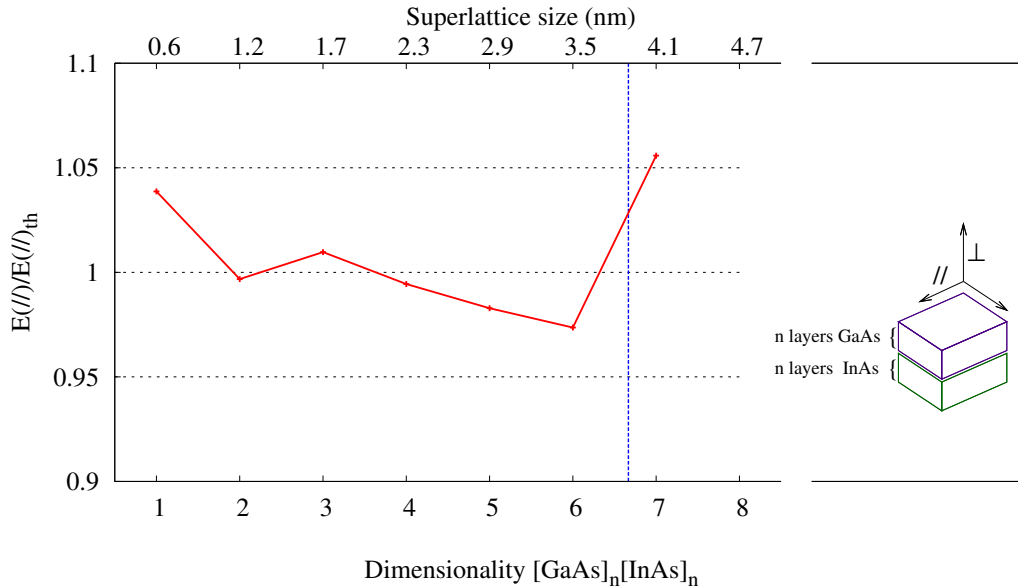


Figure 4.5: Relative electric field induced by the in-plane all-couples-in-phase vibration mode (number (6) in figure 4.7) upon dimensionality. The reference value E_{th} is the exact average of bulk GaAs and InAs (see text). The blue dashed line indicates the (rough) separation between superlattices and quantum wells *from a phonon point of view* (4.1).

has to be taken into account, and the current model of electronic cooling on a single band structure is no longer valid. We then limit the study up to $n=7$.

Electric field screening

In figure 4.6 are plotted the electric fields norm associated with each LO-mode *in the growing axis direction* (z) upon n , normalised by the in-plane value. For each depicted mode, the labelling number refers to the atomic displacements drawn in figure 4.7. At a given n , the actual number of components to plot is $4n - 1$, but are depicted only those whose norm is greater than 5 % of the reference value (because of the deviation compared to the theoretical value, depicted in figure 4.5, 5% is assumed to be the systematic error on \mathbf{E}). Identification of atomic displacements may appear subjective, since no atom is never really unmoving. Thus, the label " \mathbf{E}_\perp Bulk GaAs", for instance, has to be understood as "*Ga-As couples vibrate out-of-phase as they would do in bulk GaAs while the In-As couples have a displacement amplitude fairly negligible compared to the formers*".

On the in-plane direction, in addition to the *all-atoms-vibrating-in-phase* mode discussed previously, only one exhibits a non-negligible field (red triangles), and corresponds to all in-phase Ga-As couples vibrating out-of-phase with all In-As couples (label (1) in figure 4.7). This mode equivalent in the growing direction is plotted using blue triangles, and does not exist above $n = 2$.

The mode equivalent to the one studied in figure 4.5 in the z -direction (label (6)) is plotted

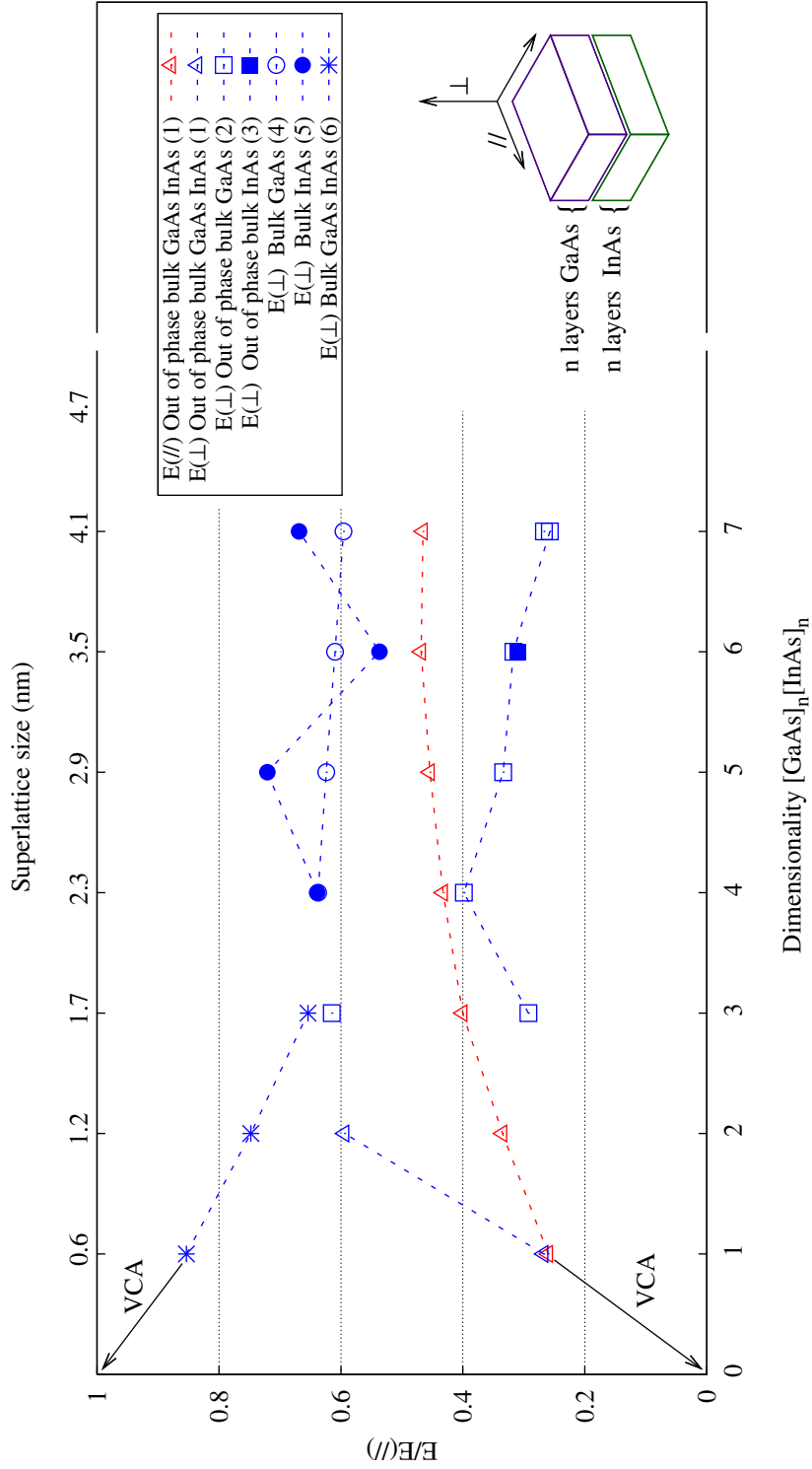


Figure 4.6: LO-modes induced electric field in $[InGaAs]_n$ superlattice normalized by the in-plane GaAs-InAs bulk value. An illustration of the atomic displacements associated with each depicted mode is drawn in figure 4.7. The label VCA highlights the virtual crystal approximation limit.

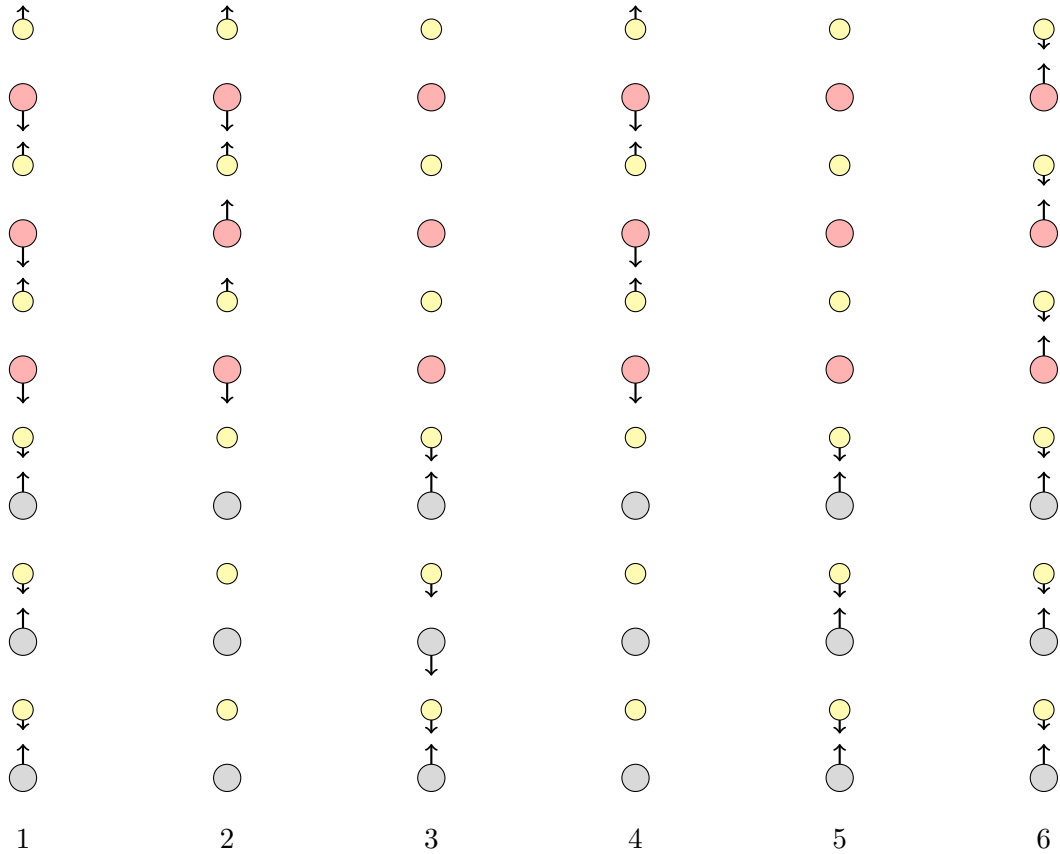


Figure 4.7: Atomic displacement associated with the modes label on figure 4.6. In, Ga and As atoms are coloured in grey, pink and yellow respectively.

with blue stars. From $n = 4$, this mode disappears and "splits" into two quasibulk modes (open and filled blue circles).

It is satisfying to notice, from the perspective of validating the model, that in the limit of the virtual crystal approximation (VCA), i.e. a bulk XAs crystal with X an imaginary atom having an average character of In and Ga , the ratio E/E_{\perp} seems to get close to unity for mode (6) (bulk XAs LO-mode vibration), and the ratio E/E_{\parallel} to 0 for mode (1) (neutral pair of atoms out-of-phase vibration).

At all n -orders, the in-plane all-couples-in-phase mode appears to dominate from an electric field point of view.

4.4.2 Effect on the electron-phonon interaction dimensionality

The influence of the above results on the electron-phonon scattering rate and on the electronic cooling is investigated through statistics performed on the emission angle. To decorrelate anisotropy effect on the cooling process from the increasing, with the dimensionality n , of the band stiffness in the z -direction, a simulation is also performed at each n assuming an isotropic field having a similar \mathbf{q} -dependence as the one observed in the bulk cases (figure 4.2). A 2-dimensional example of cooling in both cases is depicted in

figure 4.8 for InGaAs₁. This reduced picture gives a visual first indication of the field

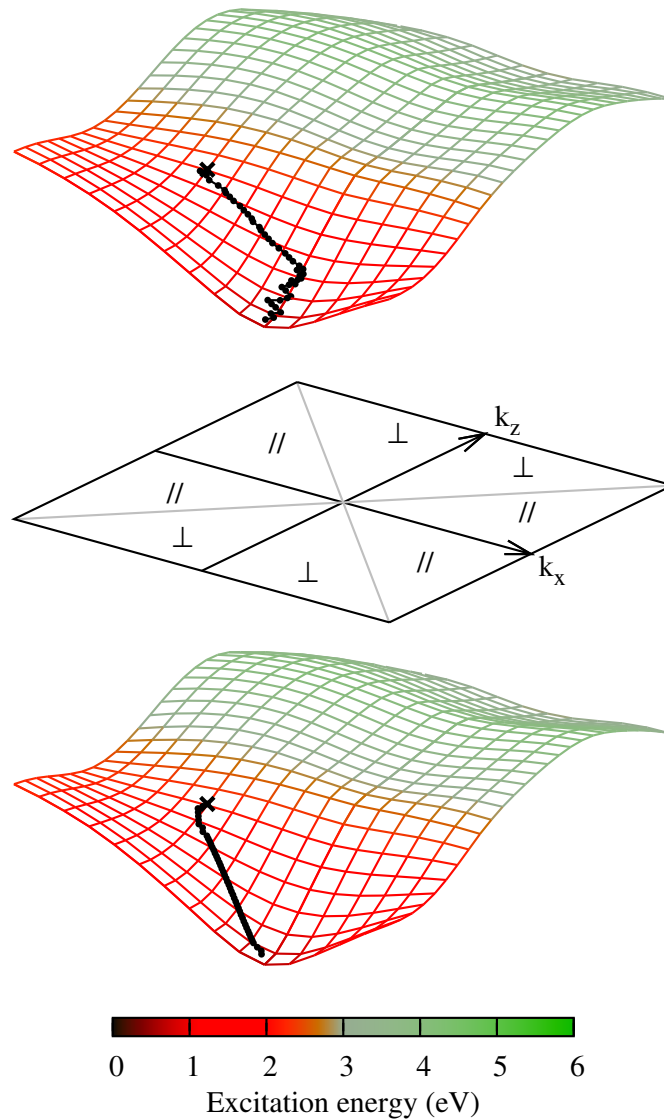


Figure 4.8: Two-dimensional picture of the electronic cooling implementation in InGaAs₁ considering the actual (top) or a bulk like (bottom) LO-induced electric field. The colour of the lowest conduction band illustrates the required photon energy to promote an electron from the valence band at each point. The plane between the two plots indicate the plane axis (k_x) and the growing axis (k_z) as well as the emission angles nomenclature. Note that on this picture the space mesh variables have been reduced from $\{k_x, k_y, k_z\}$ to $\{k_x, k_y\}$, and that the actual energy surface is a function of *three* reciprocal coordinates. On this figure also, the mesh size is forty times larger than in the actual calculation, for clarity.

anisotropy effect on the interaction dimensionality: the electron seems to "move" more parallel to the in-plane axes when the actual electric field is used. The interaction extremal path differs from the topological one, and the number of cooling steps is larger.

Figure 4.9 allows a quantitative analysis by displaying the phonon emission angle statistics upon the dimensionality n . They are labelled *in-plane* if this component is dominant over the z -direction, and *out-of-plane* in the opposite situation. In the trivial case of bulk GaAs and InAs, the distribution of in-plane/out-of-plane phonons is found to be 50 %/50 %, with a systematic error of $\lesssim 1\%$. The results in the case of an artificial isotropic field is depicted using dashed line. The proportion of emitted in-plane phonons is much larger for

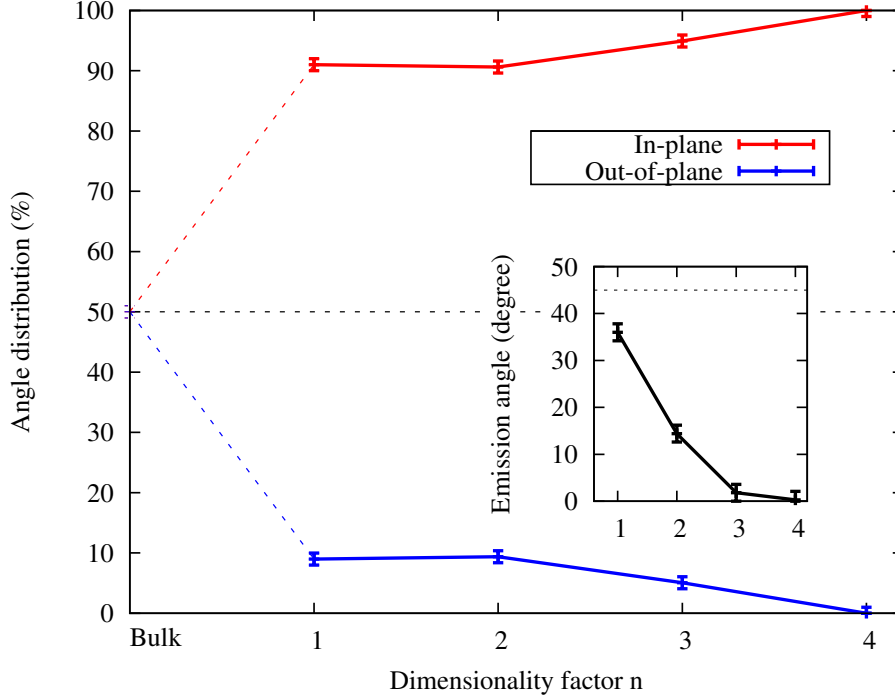


Figure 4.9: Proportion of emitted phonons having a dominant in-plane (red) or out-of-plane (blue) component, upon the dimensionality factor n . The dotted black line highlights the asymptotic bulk case. The inset shows the variation upon n of the phonon cone of emission angle.

all n than the out-of-plane ones. This distribution is of $91 \pm 1\%/9 \pm 1\%$ for $n = 1$ and 2 and $95 \pm 1\%/5 \pm 1\%$ for $n = 3$. From $n = 4$, not only is the electric field anisotropy responsible for the dimensionality effect on the interaction rate: the stiffness of the band structure in the growing direction forbids energy (4.16) and momentum (4.17) conservation rules along the extremal topological path, so that the electrons are forced to move more and more along the in-planes directions, and the above-mentioned ratio is of $100 \pm 1\%/0 \pm 1\%$.

While in the bulk case phonon emission angle can have any value between 0° and 90° (in an irreducible picture), this is not the case in InGaAs_n , as a reduction of the emission cone angle is observed. Its value at each n is plotted in the inset of figure 4.9. The asymptotic bulk case (45°) is plotted with a dashed line for comparison. The systematic precision is 1.8° . The emission cone is closing with increasing n , and reaches $0^\circ \pm 1.8^\circ$ at $n = 4$. As the in-plane distribution becomes considerably dominant, it can be stated that in the superlattice range, the electron cloud interacts mainly with a 2D-phonon population.

4.5 Conclusions on the electron-phonon interaction in superlattices

4.5.1 Approach and results

A model was derived to study the influence of dimensionality on the electron-LO-phonon interaction in thin superlattices. This model intended to allow a directional dependence of this interaction, as well as having not to make any *ad hoc* assumptions on the electronic nor on the phononic band structures. The latter are fully computed using first principle techniques. The electron-phonon interaction is related to the coupling between the hot electron and the macroscopic electric field induced by the LO-phonon atomic vibrations.

For all superlattice sizes, this electric field highest value is associated with an in-plane wavevector. The subsequent consequence on the electron-phonon interaction is that electrons interact mainly with a two-dimensional population of phonons. Although calculations did not allow to check this hypothesis, the above results lead to the reasonable conjecture that, within the superlattice range, the electron density required to significantly increase the average electron temperature T_C is lower than in bulk materials.

4.5.2 Approximations and subsequent limitations

Although reasonable, the above conjecture must be received cautiously. This model does not allow a *dynamical* description of the electronic cooling, as the interaction rates are not calculated in absolute, but compared one to another, in a deterministic picture: the expected result is a cooling time-averaged trend. In addition, it has been explained why the model is not valid anymore aside from the thin superlattice typical size systems. As shown by K. Leo and co-workers [70, 71], the electron and phonon densities two-dimensionality match in the quantum well range.

Although it has no influence on the electron-phonon interaction dimensionality, it is worth noting that neither the density dependent electron-electron interaction nor the phonon reabsorption were included in this study.

4.5.3 Perspective on the hot-carrier effect in superlattices

K. Leo and co-workers [70] introduced a parameter (α) to evaluate the critical electronic density from which the energy loss rate is reduced to less than half the low density limit ($\alpha \geq 2$). It includes LO-phonon reabsorption, and takes the form:

$$\alpha = 1 + \frac{n_{elec} \tau_{LO}}{n_{LO} \tau_{e-LO}} \quad (4.21)$$

where n_{elec} and n_{LO} are respectively the electronic and the LO-phonon densities, τ_{e-LO} and τ_{LO} being the electron-LO-phonon interaction time and LO-phonon lifetime. The expression for the critical electronic density as defined just above is then $\tilde{n}_{elec} = n_{LO} \cdot \tau_{e-LO}/\tau_{LO}$. Working with multiquantum wells systems, K. Leo and co-workers assumed their electron and phonon populations to be 2D, so that n_{elec} and n_{LO} are not dependent on the system size, and the only leverage to increase α is the enhancement of the LO-phonon lifetime. From what precedes, a 3D-dependence of both the electronic and LO-phonon densities on the cell size appears to be relevant within the superlattice range.

The discussion is focused on n_{LO} , as the restriction on the phonon emission angle reduces the phonon density more than the bare confinement due to Brillouin zone flattening would: *from bulk to superlattice well, within the current approximations, the phonon population becomes two-dimensional "more quickly" than the electron population.* Within the first assumption of a constant electron-phonon scattering time, the critical density \tilde{n}_{elec} could be computed simply by a reciprocal space integration of the emitted phonon distribution, so to observe its variation upon the superlattice dimensionality factor n .

Conclusion

Main results

In this thesis, the hot-carrier solar cell concept has been investigated from a phononic point of view. More precisely, the phonon-phonon and the electron-phonon bottlenecks, both critical for carrier cooling hindering, and related, in the energy range considered, to the LO-phonon, have been analysed.

The LO-phonon decay was studied, in a first part, through computation of the two-phonon final states in various bulk semiconductors. Density Functional Perturbation Theory was used for this aim, as it allows high precision calculations of the phonon dispersion. The frequently mentioned *large atomic mass ratio* feature, responsible for a gap in the phonon band structure that prevents LO-phonon decay through two acoustic phonons, was shown *not* to be sufficient for limiting the final states number, as the importance of the less cited *low LO-TO splitting* criterion was found non-negligible. One material, *SiSn* in the Zinc-Blende crystal structure, gathers both requirements.

The more than commonly used *zone-centre approximation* was tested to the limit. It was found to be extremely relevant, except when it does not: the case of *SiSn*, which exhibits the singular feature of all two-phonon final states being located close to the Brillouin zone boundary, is an example of this assumption failure. In such cases, the actual LO-phonon wavevector is decisive for its lifetime. To the very knowledge of the author, this behaviour has never been reported before.

As nanostructuring has been thought to be suitable for phonon gap opening in the band structure, *group-IV* and *III-V* superlattices and dots, of various sizes, were studied. It was shown that even if gaps may open indeed in the growing direction, they *does not* appear in the one-phonon density of states because of the band structure integration over the entire reciprocal space. It led to the conclusion that bulk material should be preferred for large phonon gap seeking.

Although large enough phonon gaps might be rare in relevant absorber candidates, it was pointed out that such a feature is *sufficient* but *not necessary*, as the hot-carrier effect has been measured in materials where large phonon gaps are absent.

The peculiar case of *SiSn* discovered in chapter 2, was investigated in more details by

calculating the LO-phonon lifetime *ab initio* within Density Functional Perturbation Theory. This is achieved through computation of the third order anharmonic tensor, which turned out to be a computationally demanding task, suggesting that Density Functional Perturbation Theory may not be suitable for routinely lifetime computation. This emphasised the necessity to perform a step-by-step selection of the potential candidate, starting with the two-phonon final states study, as performed in chapter 2.

The unusual dependence of the two-phonon density of final states on the initial phonon wavevector induces a stiff variation of the lifetime upon this particular parameter, and is found to be orders of magnitude greater than the common range every known semiconductors belong to. Considering how small the number of final states in a two-phonon decay is, a discussion was conducted on the possibility to reach higher order phonon processes. An average fourth-order anharmonic contribution to the LO-phonon decay was determined. It brought a correction on the LO-phonon lifetime: although not changing its order of magnitude, it brings significative change to the eventual value.

The amplitude of the rough fourth-order correction rises the question of the eventuality to ever find a material exhibiting a several tens of picoseconds LO-phonon lifetime at room temperature. However, and once again, the *long* LO-phonon lifetime being a *sufficient* but *not necessary* condition for hot-carrier effect witnessing, and since, from this chapter results, there is no reason to think that the materials in which such a hot-carrier effect was measured showed a long phonon lifetime, its origin might be found in another process, namely the electron-phonon interaction.

The electron-phonon bottleneck dependence on dimensionality was investigated in the intermediate region between bulk and quantum well that is the superlattice range. A model was proposed for the electron-phonon intraband interaction based on the LO-phonon self-induced electric field to be directional-dependent. The cooling process of hot electrons was studied in several sized $[InAs]_n - [GaAs]_n$ superlattice, n being the number of atomic layers.

The field anisotropy induces a stronger electron interaction with in-plane phonons, for any n . This suggests that within the superlattice range, the electrons mainly interact with a 2-dimensional phonon bath, which is of considerable importance for hot-carrier solar cell, since the electronic density required to enhance a hot-carrier effect might be reduced compared to bulk materials. These results call for development.

Perspectives

Numerical physics can be either philosophical, i.e. going from experimental fact to mind conceptualisation and theorisation, or, oppositely, metaphysical, so from pure mind production to an attempt to describe *a posteriori* measured results. From this point of view, the second and third chapters of this thesis are philosophical: based on measured

phonon properties and their theorisation, predictions are made on new materials. From our understanding, they allow the reasonable statement according to which finding a material exhibiting a LO-phonon lifetime *sufficiently* long, in a hot-carrier solar cell perspective, is unlikely.

What logically follows is the investigation of the carrier-phonon interactions. The fourth chapter, a modest step toward this topic, is rather metaphysical, as we formulate a model based on mind feelings and intuitions, pushing the stair-like electronic cooling picture to the limit. This work hopefully gave enough intriguing results to stimulate the research on thin superlattices for hot-carrier solar cell, and in particular from an experimental point of view. Developed models for practical results to rely on should include stronger coupling effect than what was done in this work: even if it was stated that hot-carrier solar cells practical achievement should be correlated to a better understanding of the Physics of phonons, the concept of bare phonon might not be relevant at the end, as it is said to occur, for instance, in quantum dot solar cells, by the necessity of renormalising phonon self-energy through phonon-plasmon interaction.

In June 2014, in an article published in Physical Review Letters, M. Bernardi and co-workers [173] presented new tools for cooling dynamics comprehension: a full *ab initio* study of the hot electrons behaviour during the first picosecond after photoexcitation was demonstrated, including first principles calculations of electron-electron and electron-phonon interactions within Density Functional Theory and Many-Body Perturbation theory [174, 175]. The electronic lifetime at any $\{E, \mathbf{k}\}$ could be determined, as can be seen on figure 4.10. It is highly probable that new elements concerning the electron-phonon

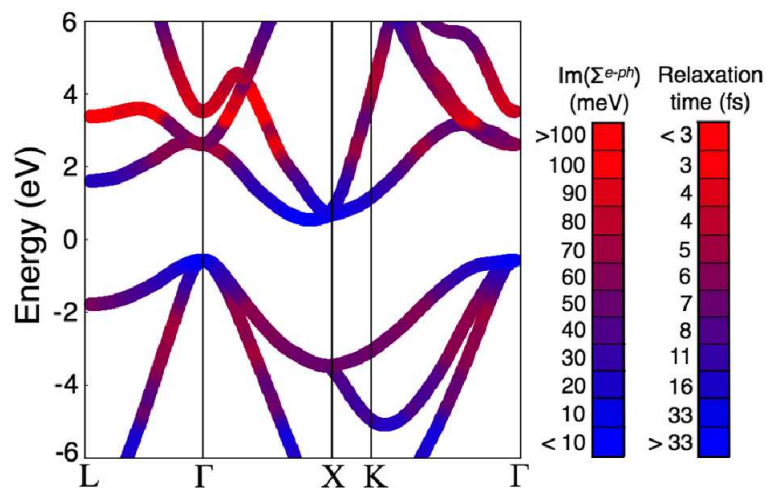


Figure 4.10: The band structure of Si, together with a colour map of electron-phonon self-energy imaginary part. Reproduced from [173].

interactions competition discussed in the first chapter will be revealed in the coming years,

and that the feasibility of *electronic band engineering* will be addressed. As is stated in the conclusion, this work "*paves the way to ab initio studies of hot carriers in materials for renewable energy*".

Appendix A

Elements of Density Functional Theory

Within Density Functional Theory (*DFT*), the total energy is written as a functional of the electronic density $n(\mathbf{r})$ as [176]:

$$E(\{\mathbf{R}\}) = T_0[n(\mathbf{r})] + \frac{e^2}{2} \int \frac{n(\mathbf{r})n(\mathbf{r}')}{|\mathbf{r} - \mathbf{r}'|} d\mathbf{r}d\mathbf{r}' + \int V_{\{\mathbf{R}\}} n(\mathbf{r}) d\mathbf{r} + E_N(\{\mathbf{R}\}) + E_{xc}[n(\mathbf{r})] \quad (\text{A.1})$$

$\psi_n(\mathbf{r})$ being related to the electronic density through:

$$n(\mathbf{r}) = 2 \sum_{n=1}^{N/2} |\psi_n(\mathbf{r})|^2 \quad (\text{A.2})$$

The first term in equation (A.1) is the kinetic energy of the non-interacting electrons having $n(\mathbf{r})$ as a ground state density:

$$T_0[n(\mathbf{r})] = -2 \frac{\hbar^2}{2m} \sum_{n=1}^{N/2} \int \psi_n^*(\mathbf{r}) \frac{\partial^2 \psi_n(\mathbf{r})}{\partial \mathbf{r}^2} d\mathbf{r} \quad (\text{A.3})$$

The second term is the *Hartree energy*, or the classical Coulomb electronic interaction energy expressed as a function of $n(\mathbf{r})$. $V_{\{\mathbf{R}\}}$ the external potential acting on the electrons, which, in the case of a bare Coulombic potential due to the nuclei, is $\sum_I v_I(\mathbf{r} - \mathbf{R}_I)$, with $v_I(\mathbf{r} - \mathbf{R}_I) = -Z_I e^2 / |\mathbf{r} - \mathbf{R}_I|$, I labelling the ions. The fourth term is the interaction between the nuclei. Finally, $E_{xc}[n(\mathbf{r})]$ is the *exchange-correlation* energy, that gather all the many-body effects. The essence of research in DFT is the derivation of a relevant expression for $E_{xc}[n(\mathbf{r})]$. Kohn-Sham orbitals are obtained by solving Kohn-Sham

Schrödinger-like equation:

$$H_{SCF} \psi_n(\mathbf{r}) \equiv \left(-\frac{\hbar^2}{2m} \frac{\partial^2}{\partial \mathbf{r}^2} + V_{SCF}(\mathbf{r}) \right) \psi_n(\mathbf{r}) = \epsilon_n \psi_n(\mathbf{r}) \quad (\text{A.4})$$

where the effective potential, referring to Kohn-Sham energy (A.1), is:

$$V_{SCF}(\mathbf{r}) = V_{\{\mathbf{R}\}} + e^2 \int \frac{n(\mathbf{r}')}{|\mathbf{r} - \mathbf{r}'|} d\mathbf{r}' + v_{xc}(\mathbf{r}) \quad (\text{A.5})$$

with $v_{xc}(\mathbf{r}) \equiv \delta E_{xc} / \delta n(\mathbf{r})$ the exchange-correlation potential. The expression of the force related to this energy is obtained derivating $E(\{\mathbf{R}\})$ with respect to the ionic position \mathbf{R}_I . In addition to the derivative of the third and the fourth term comes another term from the dependence of the total energy upon the electronic density:

$$\mathbf{F}_I^{DFT} = - \int n(\mathbf{r}) \frac{\partial V_{\{\mathbf{R}\}}(\mathbf{r})}{\partial \mathbf{R}_I} d\mathbf{r} - \frac{\partial E_N(\{\mathbf{R}\})}{\partial \mathbf{R}_I} - \frac{\delta E(\{\mathbf{R}\})}{\delta n(\mathbf{r})} \frac{\partial n(\mathbf{r})}{\partial \mathbf{R}_I} \quad (\text{A.6})$$

Because the total energy of the system is extremal for the ground state density, the last term vanishes and the latter equation matches exactly the generalised force expression (equation (2.24)).

Appendix B

Elements of Density Functional Perturbation Theory

In this appendix are given computational details related to the calculation of the phonon dispersion relation within Density Functional Perturbation Theory (*DFPT*). Ground state calculations were performed within Density Functional Theory (*DFT*) as implemented in the Quantum Espresso package [6], using the Local-Density Approximation (*LDA*) plane-wave pseudopotential method for exchange and correlation energy. Norm-conserving pseudopotentials generated within the Troullier-Martins formalism [177] were used. The Brillouin zone integration over the electronic states was performed using the special k -point Monkhorst-Pack method [178] on a shifted $6 \times 6 \times 6$ grid. A systematic accuracy of $0.1 \text{ meV} \cdot \text{atom}^{-1}$ on the ground state total energy was reached for all studied materials so to ensure a precision on the phonon band structure of the order of 1 cm^{-1} [157]. The interatomic force constants were determined within DFPT using the *grid method* [179] on a $8 \times 8 \times 8$ mesh (so equivalent to a direct real space force constant calculation in a 1024-atom supercell), that leads to 29 special \mathbf{q} -point for the Zinc-Blende crystal structure, and then Fourier-extrapolated on a much finer mesh (section (2.4.1.2)). To show the reliability of the calculation, some of the computed phonon frequencies are gathered in table B.1 and compared to experimental data whenever they exist. The accordance is also displayed in the insets of figures 2.6 and 2.7.

	Γ_{LO}	Γ_{TO}	X_{LO}	X_{TO}	X_{LA}	X_{TA}	L_{LO}	L_{TO}	L_{LA}	L_{TA}
GaAs	294	275	242	258	226	79	267	241	212	62
([114])	(293)	(271)	(240)	(256)	(225)	(82)	(263)	(242)	(207)	(63)
AlAs	396	358	389	330	213	97	366	345	210	72
([107, 132])	(400)	(362)	(385)	(333)	(225)	(104)			(205)	(79)
GaSb	238	231	212	209	162	58	221	203	157	46
([131])		(230)	(211)	(211)	(167)	(57)	(217)	(204)	(154)	(45)
AlSb	338	328	341	292	162	66	324	312	152	52
([133])	(346)	(326)	(340)	(293)	(153)	(68)	(320)	(306)	(148)	(54)
GaP	408	374	372	363	259	107	373	368	240	83
([130])	(405)	(368)	(372)	(357)	(254)	(104)	(372)	(359)	(314)	86
InP	355	315	331	322	195	70	335	318	178	56
([128, 129])	(353)	(307)	(329)	(322)	(193)	(66)	(339)	(318)	(166)	53
Si	509	509	406	455	406	140	408	485	372	108
([99])	(515)	(515)	(411)	(449)	(411)	(147)	(411)	(488)	(378)	(113)
SiC	964	788	983	758	632	365	833	763	613	269
([135])	(970)	(789)					(834)	(765)	(609)	(267)

Table B.1: Computed phonon frequencies at high symmetry points Γ , X and L . All values are in cm^{-1} . The experimental references are given between parenthesis.

Appendix C

SiSn electronic band structure

The electronic band structure of SiSn was determined using G_0W_0 correction [180, 181] on top of a Density Functional Theory (DFT) calculation using the Projector Augmented Wave method (PAW) [167] as implemented in the VASP package [5].

The differences in energy between Γ -, L - and X -valley as a function of the inclusion of the d -states in the valence are gathered in table C.1. The inclusion of d -states in the valence within the pseudopotential approximation appears to have only a soft influence in PAW . In addition, the G_0W_0 correction clearly appears to be \mathbf{k} -point-dependent, so that a scissor shift is not a relevant correction. There are qualitative agreements between the two sets of results: the direct band gap at Γ is close to 1 eV, and the X -valley appears to be at least 0.1 eV above the two others. The PAW method is thus used to compute the band structure since it has a low dependence on the inclusion of d -states. The spin-orbit coupling is taken as a first order perturbation taken from DFT , as a gap-closing constant of 0.1 eV.

Method	$\Gamma_c - \Gamma_v$	$L_c - \Gamma_v$	$X_c - \Gamma_v$
PAW	0.36	0.43	0.78
$PAW + G_0W_0$	1.04 (+0.68)	0.93 (+0.50)	1.10 (+0.32)
PAW_d	0.40	0.44	0.77
$PAW_d + G_0W_0$	0.98 (+0.58)	0.92 (+0.48)	1.14 (+0.37)

Table C.1: G_0W_0 corrections comparison on the valley ordering. These results do not include the spin-orbit coupling corrections applied on the band structure calculation. The values are in eV.

Appendix D

DFT calculation using hybrid functional

Predicting the electronic properties of Zinc-Blende InX III-V materials ($X = N, P, As, Sb$) from first principle calculations had been a remaining issue until the use of hybrid functional by G. Kresse and his co-workers [182]. In addition to the lack of inversion symmetry, consubstantial with the Zinc-Blende crystal structure, and the spin-orbit coupling that splits the threefold-degenerate highest valence band into a split-off, a light hole and a heavy hole bands, the interaction between semicore d -electrons from the Indium atom creates shallow bands close to the valence band region. For this reason, it is well known now that these d -states have to be treated as valence states within the pseudopotential approximation, and that one should take into account the spin-orbit coupling in the calculations [183].

The band structure of $InAs$ within several approximations is depicted on figure D.1. The first conduction band energy level at the Γ , X and L points are compared to two references: S. Adachi's work [184, 171] on $Ga_xIn_{1-x}As_ySb_{1-y}$ band gap extrapolation (referred as (1)), and J. R. Chelikowsky's and M. L. Cohen's one [172] with the use of an empirical non-local pseudopotential method (referred as (2)). Despite their extremely similar results on the band gap (0.35 eV (1) and 0.37 eV (2)), the values $X_c^6 - \Gamma_v^6$ and $L_c^6 - \Gamma_v^6$ show a large discrepancy, respectively 0.91 eV and 0.45 eV. Unfortunately, no experimental data exist for these parameters.

The simple Density Functional theory (DFT) calculation (red line) gives a "negative" band gap, as could be expected since it is small (< 0.5 eV) in $InAs$, and systematically lowered within DFT. The $PBE0$ (blue line) and $HSE06$ (grid solid line) hybrid method differ by the introduction of a function in the latter that screens the long-range part of the Hartree-Fock interaction, the amount of the latter incorporated in the exchange-correlation energy being the same in both methods [185]. The $PBE0$ method obviously leading to much less accurate results in this case, we focus on the $HSE06$ one. This latter approximation leads to an excellent agreement with the results of (2) on the three high symmetry points, when

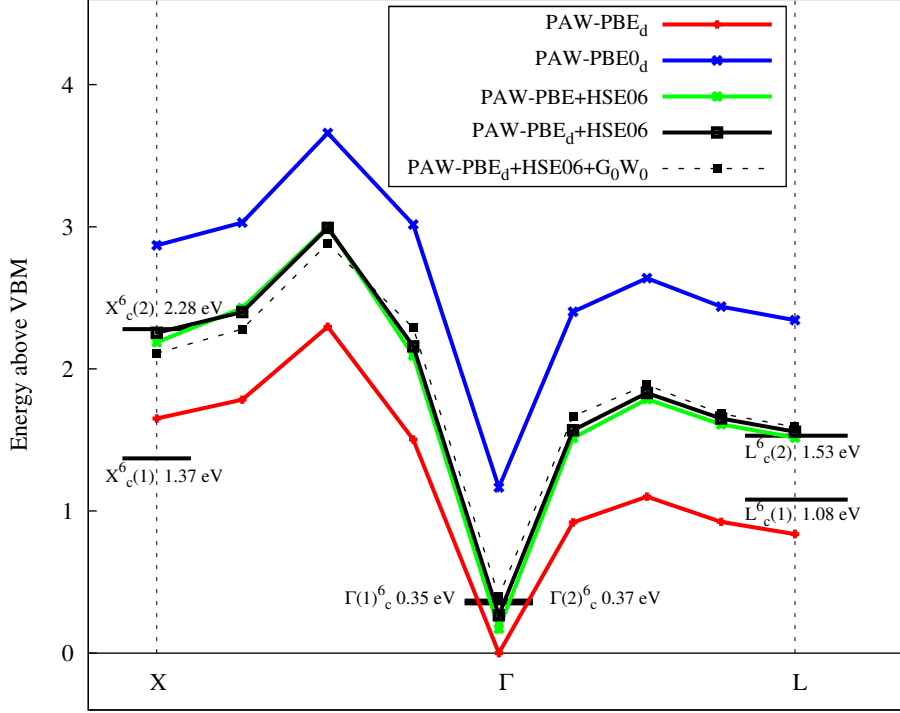


Figure D.1: InP band structure within several approximations for the exchange-correlation energy functional. The reference values are reproduced from S. Adachi's [171] (1) and J. R. Chelikowsky's and M. L. Cohen's work [172] (2).

indeed the d-states are included in the valence (black solid line), while the band gap is 0.1 eV lower if they are omitted (green solid line). The found values are recalled in table D.1. The addition of a G_0W_0 correction does not bring substantial improvement (black dashed line), so that it is not used in the subsequent calculations.

	$\Gamma_v^6 - \Gamma_c^6$	$\Gamma_v^6 - X_c^6$	$\Gamma_v^6 - L_c^6$
This work	0.29	2.25	1.54
(1) [171]	0.35	1.37	1.08
(2) [172]	0.37	2.28	1.53

Table D.1: Band parameters of InAs.

Appendix E

Transferability of the interatomic force constants

The transferability of the force constants is here checked for *Si/Ge* and *GaSb/AlSb*. The region of interest in both cases is the acoustic one (see chapter 2). Getting back to equation E.1 to be solved (section 2.1.2):

$$\sum_{J,\beta} \left[\frac{C_{I,\alpha;J,\beta}(0,l')}{\sqrt{M_I M_J}} - \omega^2 \delta_{IJ} \delta_{\alpha\beta} \right] u_{J,\beta}^{(0)} e^{i\omega t} = 0 \quad (\text{E.1})$$

where I and J label the atoms, α and β the coordinates, the idea of the *mass approxima-*

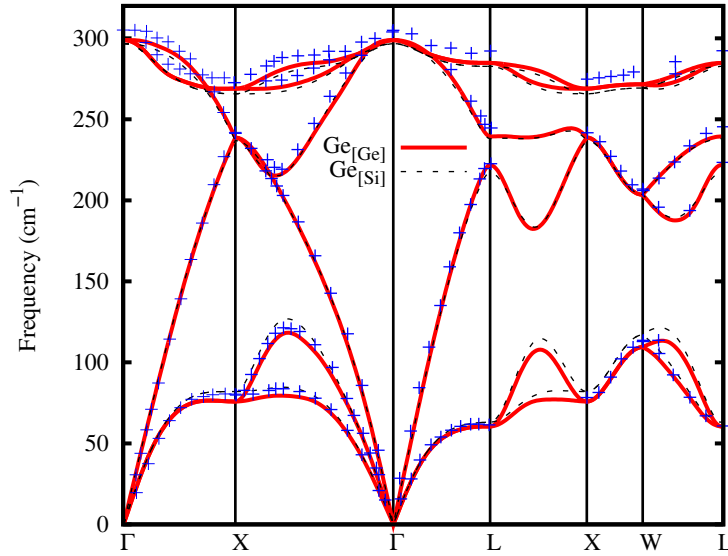


Figure E.1: Transferability of the force constant from *Si* to *Ge*. The Ge band structure has been calculated using the force constant of *Ge* (red solid line) and *Si* (black dashed line), and is compared to experimental values reproduced from [186] (blue crosses).

tion is to use the real space interatomic force constant $C_{I,\alpha;J,\beta}$ calculated for one material (A) to compute the band structure of another (B), simply inserting the appropriate atomic

masses M in the above equation. From a ball-and-spring model point of view, this is equivalent to assume that the springs stiffness is equal in both materials, and that only the balls mass changes. In figure E.1 are plotted the Ge phonon band structures computed using the interatomic force constant of Ge and Si , respectively label $Ge_{[Ge]}$ and $Ge_{[Si]}$. In figure E.2 are plotted the $AlSb$ phonon band structures computed using the interatomic force constant of $AlSb$ and $GaSb$, respectively label $AlSb_{[AlSb]}$ and $AlSb_{[GaSb]}$. The largest observed discrepancy between $B_{[B]}$ and $B_{[A]}$ is 8 cm^{-1} in the case of Si/Ge , and 10 cm^{-1} for $GaAs/AlSb$. This result agrees with the statement according to which the mass ap-

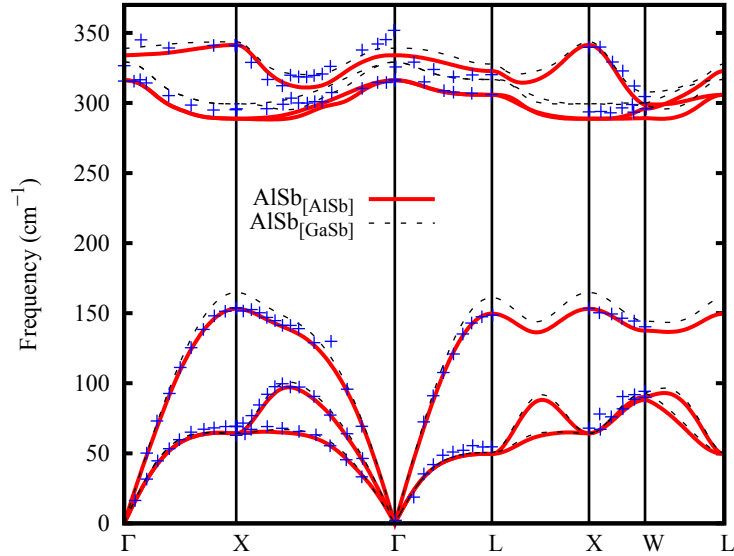


Figure E.2: Transferability of the force constant from $GaSb$ to $AlSb$. The $AlSb$ band structure has been calculated using the force constant of $AlSb$ (red solid line) and $GaSb$ (black dashed line), and is compared to experimental values reproduced from [99] (blue crosses).

proximation is satisfactorily accurate when the two materials differ by their cations, as it has been for instance verified in $GaAs/AlAs$ compared to $GaAs/GaSb$ [99].

Appendix F

Conservation rules Gaussian width

The need for an error function comes from that we have no knowledge of an analytical form for the iso-energy surface defined by energy and momentum conservation rules:

$$\hbar\omega_{\mathbf{q}_2}^{s_2} + \hbar\omega_{\mathbf{q}_3}^{s_3} - \hbar\omega^{LO} = 0 \quad (\text{F.1})$$

which is the reason for which we substitute the Dirac delta function in the rate equation (3.8) by a *tolerance* numerical function $\tilde{\delta}(\omega)$:

$$\tilde{\delta}(\omega) = \frac{1}{\sigma\sqrt{2\pi}} e^{-\left(\frac{\omega - \omega^{LO}}{2\sigma^2}\right)^2} \quad (\text{F.2})$$

where $\omega = \hbar\omega_{\mathbf{q}_2}^{s_2} + \hbar\omega_{\mathbf{q}_3}^{s_3}$. By taking a Gaussian form for $\tilde{\delta}$, the closer to 0 the sum $\hbar\omega_{\mathbf{q}_2}^{s_2} + \hbar\omega_{\mathbf{q}_3}^{s_3} - \hbar\omega^{LO}$, the more the three-phonon process contributes in the rate integral. The tolerance parameter σ is to be determined. Values reported in the literature are of the order of 1 cm^{-1} [125, 104, 124].

The LO-phonon lifetime in Silicon was computed for several \mathbf{q} -independent trial σ values and reported on figure F.1. Over two orders of magnitude (10^{-1} to 10^1) the computed lifetime does not sharply depend on the trial σ values: from 4.22 ps for $\sigma = 0.1 \text{ cm}^{-1}$, it passes through an extremum (4.56 ps for $\sigma = 1 \text{ cm}^{-1}$) and ends at 4.44 ps for $\sigma = 10^1 \text{ cm}^{-1}$. A larger discrepancy compared to experiment is found for $\sigma = 10^{-2}$ (8.8 ps). The value $\sigma = 1 \text{ cm}^{-1}$ was retained for the rate integral calculation in chapter 3.

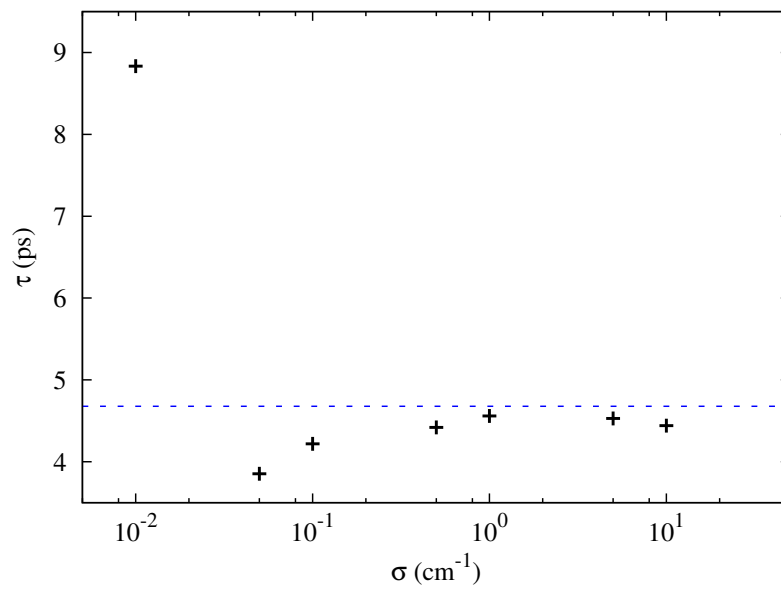


Figure F.1: Dependence of the computed LO -phonon lifetime on the Gaussian width in equation (F.2) in Silicon at 0K. The experimental value (dashed blue line) is reproduced from [125].

Appendix G

Average fourth-order phonon-phonon coupling constant

The simplest approach to reach an average fourth-order anharmonic constant is to compute the total energy of the system, when the atoms are in their equilibrium positions, and when they are displaced by Δu according to a LO vibration mode (typically, 0.04 Å in the [111] direction [158]). The energy difference is written $\Delta E(u)$, and the constant would simply be $\Delta E(u)/(\Delta u)^4$. Call it *simple model*.

We instead use the approach of D. Vanderbilt and co-workers [157], which consists in computing $\overline{\Delta E} \equiv [\Delta E(u) + \Delta E(-u)]/2$ to eliminate the odd term, and then plot $\overline{\Delta E}/u^2$ versus u^2 , the slope of the curve giving the fourth derivative of the total energy (see figure G.1) The values obtained using both methods are gathered in table G.1.

	Si	SiSn
<i>simple model</i>	125	82
Vanderbilt [157]	135	96

Table G.1: Fourth-order anharmonic coupling constants obtained with different computational methods (see text). All values are in $eV \cdot \text{Å}^{-4}$.

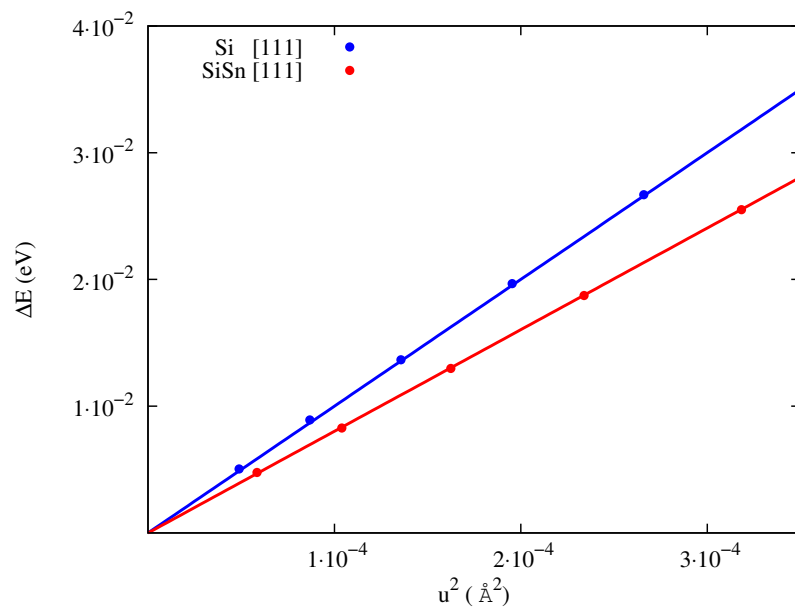


Figure G.1: Energy distortion ΔE as a function of the displacement u along the [111] direction for Si and SiSn.

Résumé en français

Introduction

Il est d'usage, dans les premières pages d'une thèse de doctorat ayant trait à l'énergie solaire, d'y trouver un long plaidoyer en faveur de l'exploitation des sources d'énergies renouvelables. Sautant ce préambule, je commencerai à m'attacher directement à ce sujet ô combien passionnant qu'est le photovoltaïque de future génération. Une analyse de la nécessité de diversifier notre production d'énergie peut par exemple être trouvée dans la revue de A. Luque [1]. A ce jour, la question n'est en effet plus "*Le photovoltaïque fonctionne-t-il ?*", mais plutôt "*A quel rendement maximum pouvons-nous prétendre*". La *limite de Shockley-Queisser* [2], théorisée il y a plus de cinquante ans, et selon laquelle le rendement maximal d'une cellule à simple jonction p-n ne peut excéder 31%, n'est désormais plus un objectif suffisamment ambitieux compte tenu des progrès réalisés. L'heure est plutôt aux technologies de troisième génération, parmi lesquelles figure la cellule solaire à porteurs chauds (*HCSC*).

Imaginée en 1982 par R. T. Ross et A. J. Nozik [3], cette cellule possède un rendement maximum théorique de l'ordre de la limite thermodynamique [4]. Son mode de fonctionnement est *simple*, et joue sur le principe premier du gain photovoltaïque, se concentrant sur la séparation des charges électriques. Le fossé, de moins en moins profond, qui nous sépare de la réalisation concrète d'un tel dispositif se caractérise dans notre manque de connaissance ou de compréhension de certains phénomènes physiques fondamentaux. D'elles découle pourtant la capacité de choisir les matériaux adéquats pour l'implémentation des HCSC. Cependant, il est à noter que l'engouement pour la recherche sur ce type de cellules semblent suivre celui pour les technologies photovoltaïques en général (figure 1). Il est raisonnable de s'attendre à de sérieux progrès dans les prochaines années.

Ces problématiques sont principalement liées aux mécanismes de perte d'énergie des porteurs de charges (souvent réduits aux seuls *électrons*, les trous ayant un comportement symétrique). Ces derniers cèdent ainsi, après avoir été photogénérés, leur excès d'énergie cinétique au réseau cristallin sous la forme de quanta vibrationnels, appelés *phonons* ; c'est un cas particulier de l'*interaction électron-phonon*. Le processus inverse, l'absorption de phonon, est également possible, pourvu que ces pseudo-particules ne se décomposent pas,

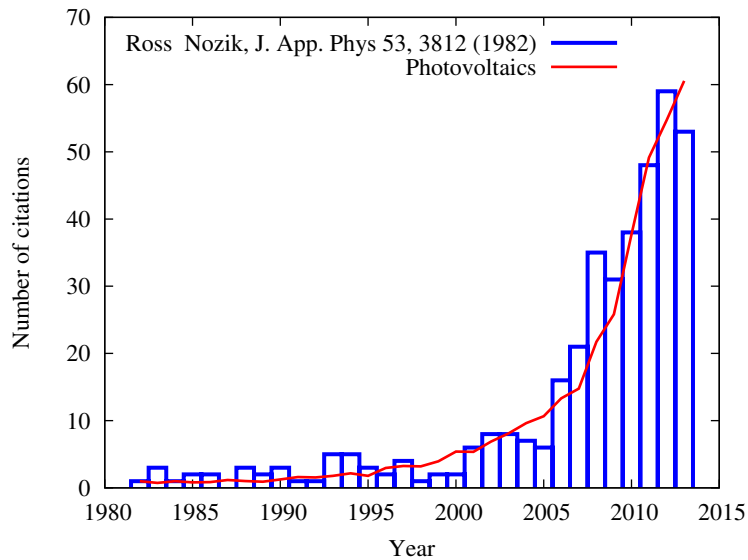


Figure 1: Nombre de publications scientifiques par an citant l'article original de R. T. Ross et A. J. Nozik qui introduisit le concept de cellules photovoltaïques (bleu), et variation relative du nombre de publications ayant trait aux technologies photovoltaïques en général (rouge).

entre temps, en d'autres phonons; il est alors question d'*interaction phonon-phonon*.

S'attaquer à ce type de problématique requiert donc des outils rendant compte des interactions fondamentales à l'échelle sub-nanométrique. Il devient alors possible de comprendre les phénomènes relatifs à l'effet porteurs chauds tels qu'il est mesuré, puis de prédire son existence sous certaines conditions bien identifiées. Les méthodes de simulation dites *ab initio* ont en ce sens prouvé leur efficacité ainsi que leur précision, et l'augmentation constante de la puissance de calcul disponible rend leur utilisation de plus en plus standard, en plus d'élargir leur domaine d'application.

La recherche d'un rendement toujours plus élevé est moteur de l'innovation dans le domaine du photovoltaïque en général. Les cellules à porteurs chauds sont en ce sens un but ultime. La difficulté réside en ce que, par notre volonté de freiner le refroidissement des porteurs, nous cherchons à exalter un comportement presque contre nature.

Plan de l'étude

Cette thèse est divisée en quatre chapitres. Ayant un but explicatif et une visée prédictive, les études sont menées numériquement, utilisant des techniques de calculs *ab initio*. Le premier chapitre s'attache à fixer le contexte de l'étude, allant du concept général de photovoltaïque de troisième génération vers les problématiques phononiques spécifiques aux cellules à porteurs chauds. Dans un second temps, la décomposition du phonon LO

est étudié en terme d'états finaux à deux phonons disponibles. Une discussion est menée sur les critères de sélection de candidats pour le matériaux absorbeurs. Le troisième chapitre pousse l'analyse un cran plus loin, par l'étude du temps de vie du phonon LO dans un matériau spécifique mis en lumière dans le chapitre précédent. Une discussion est menée sur la possibilité d'évaluer la contribution des ordres de décomposition supérieurs à trois, et sur l'atteignabilité des critères phononiques jugés *suffisants* pour exalter l'effet porteur chaud. Dans le dernier chapitre, une étude exploratoire de l'interaction électron-phonon dans les super-réseaux est proposée. Un modèle reliant la constante de couplage au champ électrique induit par le phonon LO est proposé, et la dimensionalité des populations électroniques et phononiques en jeu est examinée.

Seuls les résultats principaux sont rappelés dans ce résumé. Les détails méthodologiques et bibliographiques peuvent être trouvés dans la version anglaise du manuscrit.

La cellule solaire à porteurs chauds

La cellule de Ross et Nozik fait partie des cellules photovoltaïques dites de *troisième génération*, parmi lesquels figurent également les cellules à multijonctions et à bandes intermédiaires, pour ne citer que les concepts les plus répandus. Ces technologies sont conçues pour palier la nature polychromatique de la lumière, adaptant les niveaux d'énergies de l'absorbeur de façon à les rendre résonants à plusieurs longueurs d'onde, et partant toujours du principe que la population d'électrons photogénérés est extraite au niveau d'énergie de conduction le plus bas. Celle imaginée par Ross et Nozik il a maintenant plus de trente ans (figure 2), au contraire, a pour ambition d'extraire les porteurs non encore à l'équilibre thermique avec le réseau cristallin, bien au dessus du bas de la bande de conduction. Le gain en voltage correspond ainsi à la différence entre l'énergie d'extraction et le bas de la bande de conduction

Comprendre son fonctionnement implique au préalable de définir le simple concept de "*porteur chaud*". Dans un article traitant du refroidissement des porteurs de charge, S. A. Lyon en donne cette définition :

Nous appelons "porteurs chauds" des électrons, ou des trous, ayant une énergie cinétique bien supérieure à l'énergie thermique moyenne du réseau cristallin, notée kT_L . Ces porteurs ne forment pas en général une distribution à l'équilibre, de sorte que "chauds" n'implique pas que l'on puisse en définir une température. [19]

Il s'avère en fait que les porteurs équilibrent entre eux leur excès d'énergie cinétique dans les premières dizaines de femtosecondes suivant leur excitation, et qu'une température peut être définie au delà de ce temps critique [20, 21]. Ce processus est appelé *thermalisation*, et est bien distinct de celui de *refroidissement* [14], détaillé plus loin. Notre définition de "porteurs chauds" sera donc une version *thermalisée* de celle de S. A. Lyon, c'est à dire

une population à l'équilibre thermique ayant une énergie supérieure à celle de l'énergie de bande interdite (*gap*).

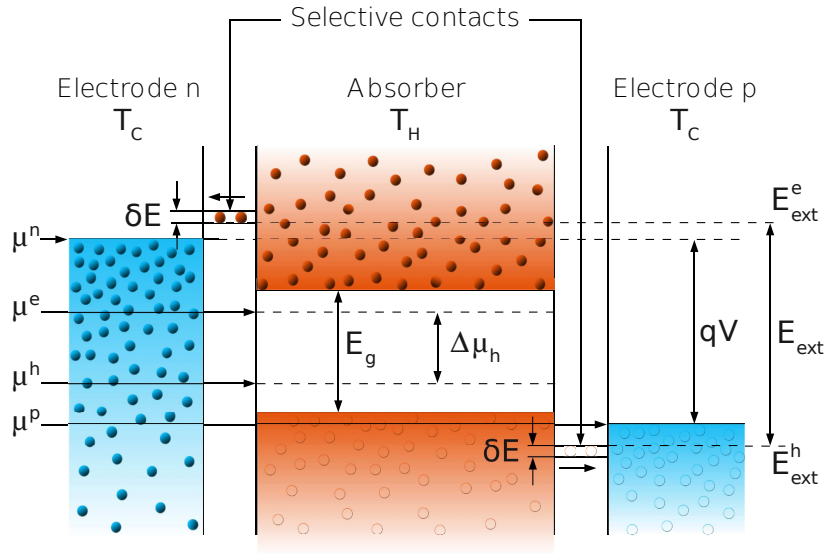


Figure 2: Principe du fonctionnement de la cellule solaire à porteurs chauds. Les électrons/trous sont extraits à une énergie $E_{ext}^{e/h}$ via des contacts sélectifs en énergie de largeur δE . Le gain en voltage par rapport à une extraction au bas de la bande conduction est $E_{ext} - qV$. Reproduit depuis [7].

Refroidissement des porteurs et problématiques phononiques

La tendance selon laquelle l'énergie moyenne des porteurs tend à décroître dans le temps est appelé *refroidissement*, et est reliée à une multitude de phénomènes complexes, notamment des transitions intervallée et intravallée, ainsi que les processus Auger et d'ionisation par impact (voir figure 3). Dans la suite nous prendrons seulement l'exemple des électrons, dans un matériau à *gap* direct, mais il est à noter que les trous ont un comportement similaire, bien que couvrant une plus petite gamme d'énergie du fait de leur plus grande masse effective. Il a été empiriquement démontré que si, après avoir été photogénéré, un électron se trouve au dessus du seuil de transition intervallée (ligne en pointillé sur la figure 3), alors il rejoindra avec une très grande probabilité une vallée satellite, et perdra peu à peu son excès d'énergie cinétique d'abord via des transitions inter et intravallées satellites [30, 31]. Il ne rejoindra la vallée Γ qu'une fois au plus bas de celles-ci. La perte d'énergie se poursuit alors par transition intravallée, via l'émission, dans le cas d'un semiconducteur polaire, d'un phonon LO, soit un mode de vibration correspondant à un déplacement des atomes en opposition de phase les uns par rapport aux autres. Le phénomène inverse, *i.e.* l'absorption d'un tel phonon, est également possible, de sorte que le ratio *emission/absorption* influence le temps global de refroidissement des porteurs [48]. L'*effet porteurs chauds* est caractérisé par un temps de refroidissement global au moins de l'ordre de 1 ns [62].

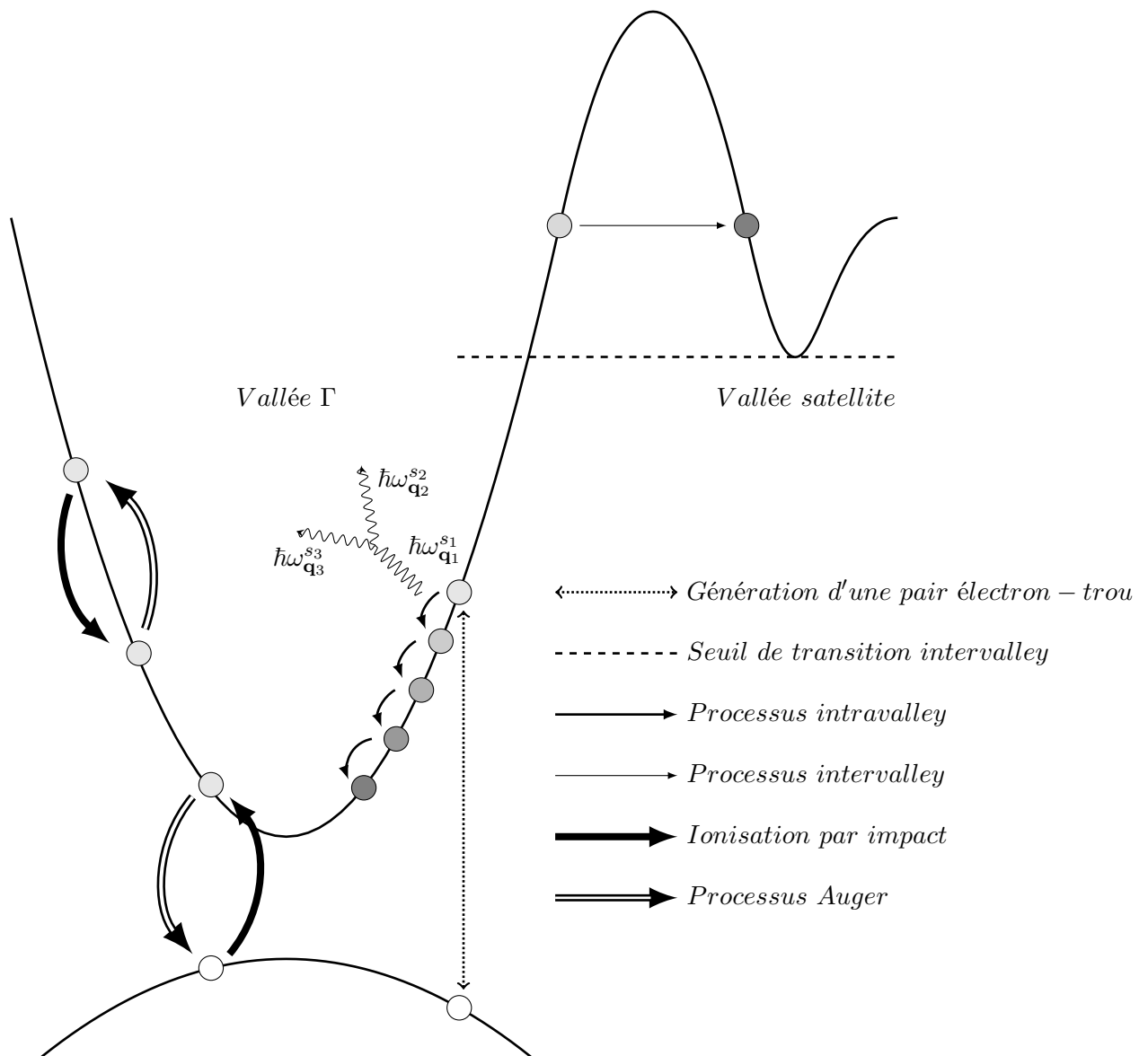


Figure 3: Processus de refroidissement des porteurs chauds.

Au premier ordre, les phonons sont des modes propres, ayant une stabilité infinie dans le temps. Là encore, le rapport à l'expérience conduit à la nécessité d'aller au delà de cette approximation, afin de rendre compte, par exemple, de la finitude de la conductivité thermique [102]. Ainsi, le phonon LO émit lors du refroidissement n'est pas stable, et se décompose, typiquement entre une en quelques picosecondes dans la plupart des semiconducteurs, en d'autres phonons de plus basse énergie. La vitesse à laquelle une population de porteurs chauds revient à l'équilibre thermique du réseau est ainsi très dépendante du temps de vie du phonon LO [48].

La discussion précédente fait apparaître deux axes de travail pour exalter l'effet porteurs

chauds : écranter l'interaction electron-phonon LO d'une part, et travailler avec un absorbeur dans lesquels le temps de vie du phonon LO est au minimum un ordre de grandeur plus long qu'il ne l'est en moyenne dans les matériaux dans lesquels il a été mesuré, soit typiquement de l'ordre de 100 *ps*.

Techniques *ab initio*

L'analyse des propriétés phononiques des matériaux se voulant prédictive, le choix de la méthode s'est portée sur la théorie de la fonctionnelle densité perturbée (*DFPT*), telle qu'implémentée dans la suite de codes Quantum Espresso [99, 97, 110]. Cet outil a prouvé son efficacité dans la compréhension d'un grand nombre problématiques liées aux vibrations du réseau cristalin, parmi lesquels, l'étude des modes mous et des transitions de phase sous pressions [115] ; les phonons dans les super-réseaux [116], les alliages [117], et les nanostructures de type graphene [118] et fullerene [119] ; les propriétés vibrationnelles des défauts [120] ; les modes de surface [121] ; les propriétés thermodynamiques dans l'approximation quasi-harmonique [122] ; l'analyse du tensor Raman [123] ; et finalement, le temps de vie des phonons dans les semiconducteurs via la dérivée troisième de l'énergie totale par rapport aux déplacements atomiques [104, 124].

Malheureusement, le temps de calcul requis varie avec le nombre d'atomes N_{at} selon N_{at}^α , $\alpha \sim 3 - 4$, ce qui limite dans la pratique la taille des systèmes à environ 100 atomes. Cela correspond, par exemple, à une maille cubiques de silicium de volume $1,3 \times 1,3 \times 1,3 \text{ nm}^3$, ou à une feuille carrée de graphene de surface $1,6 \times 1,6 \text{ nm}^2$.

Etats finaux à deux phonons

La décomposition du phonon LO peut être décrite au premier ordre par son annihilation et la création de deux autres phonons. Ce processus doit évidemment respecter les règles de conservation du vecteur d'onde $\mathbf{q}_2 + \mathbf{q}_3 = \mathbf{q}_1$ et de l'énergie $\hbar\omega_{\mathbf{q}_2}^{s'} + \hbar\omega_{\mathbf{q}_3}^{s''} = \hbar\omega_{\mathbf{q}_1}^s$, $\hbar\omega_{\mathbf{q}}^s$ étant l'énergie du phonon de vecteur d'onde \mathbf{q} et d'index de branche s . Dans notre cas, $\mathbf{q}_1 \sim \mathbf{0}$ et $s \equiv LO$. Les paires de phonons "2" et "3" vérifiant ces relations sont les *états finaux* de décomposition. Le principe de l'ingénierie phononique consiste à travailler sur la structure de bande phononique, par choix des atomes dans la maille cristalline ou nanostructuration, de sorte que les deux relations précédentes soient vérifiées pour le plus petit nombre possible d'états finaux. Pour les besoins de l'analyse, nous classerons les canaux de décomposition en deux familles : les canaux Ridley d'une part, dans le cas où les phonons finaux sont tous les deux des phonons acoustiques, et les canaux Ridley, pour lesquels l'un des phonons finaux est un acoustique et l'autre un optique (figure 4).

Une description simple des modes de vibrations dans un cristal permet de mettre en

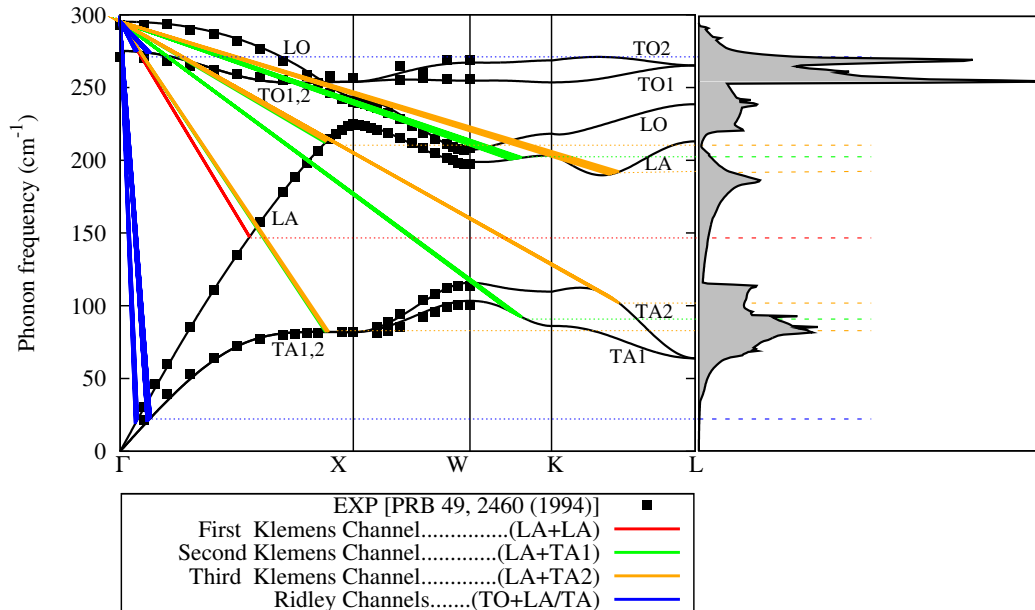


Figure 4: Décomposition du phonon de centre de zone dans GaAs. Les traits de couleurs guident le regard et relient le phonon LO initial (en haut à gauche) aux deux phonons finaux. Les points expérimentaux (carrés pleins noirs) sont reproduits d'après [107].

évidence une forte dépendance de la largeur des bandes interdites phononiques au ratio des masses atomiques. Une étude des états finaux à deux phonons a donc été menée, dans un premier temps, sur une gamme de semiconducteurs binaires appartenant aux groupes III-V et IV-IV.

Matériaux massifs

Cette étude a révélé la singularité du matériau SiSn en structure Zinc-Blende. Le fort ratio des masses entre le silicium et l'étain engendre un gap entre les régions acoustiques et optiques presque suffisamment large pour interdire complètement les canaux Klemens : les quelques états disponibles sont alors confinés au bord de la zone de Brillouin près du point X. Il a aussi été mis en évidence que le critère souvent omis selon lequel le gap entre les branches LO et TO doit être aussi petit que possible est tout aussi critique que celui d'un grand ratio des masses atomiques, et ce dans un double intérêt : le nombre de canaux finaux de Ridley n'en est que plus réduit, et le poids des états finaux dans le processus global de décomposition, qui décroît linéairement avec \mathbf{q} [104], en est d'autant plus faible puisque ces états sont alors confinés proche du centre de la zone de Brillouin. Cet argument a trouvé un écho expérimental particulier avec le cas d'InN. Ayant d'abord été présenté comme un potentiel excellent candidat de par sa structure de bande interdisant strictement les canaux Klemens [82, 80], une étude Raman a ensuite montré que le grand nombre d'états finaux dû au fort écart entre les bandes LO et TO ramenait le temps de vie à des valeurs très en dessous des premières estimations [85, 86].

Nanostructures

Une étude similaire est menée sur des super-réseaux et des boîtes quantiques, de type Si/Ge et GaSb/AlSb, l'accent étant mis cette fois sur l'apparition ou non de gaps dans la densité d'états de phonon. Il est mis en évidence, pour les super-réseaux, que le (ou les gaps) qui peuvent s'ouvrir à cause de la rupture de symétrie suivant l'axe de croissance n'occupe pas la même position en énergie dans toutes les directions de l'espace réciproque, et de fait, n'apparaît pas dans la densité d'états totale. L'analyse des boîtes quantiques met aussi en évidence que le grand nombre de degrés de liberté dans des structures aussi complexes rend très difficile l'ajustement de ces gaps. Ces résultats rejoignent ceux d'autres travaux [83, 109] selon lesquels un gap *suffisant* serait obtenu à condition de se restreindre à des boîtes ayant un volume de 1 nm^3 tout au plus, et dont le ratio des masses entre les atomes de la boîte et de la matrice serait de 7, au minimum.

Ces résultats tendent à faire penser que la recherche de gap dans les structures de bande de phonons a plus de chance d'aboutir en se limitant aux matériaux bulks. SiSn est en ce sens un exemple intéressant, et a servi d'exemple lors de l'investigation du calcul du temps de vie du phonon LO par la DFPT, détaillée dans le chapitre 3.

Taux de décomposition et temps de vie du phonon LO

L'analyse mise en place au chapitre précédent agit comme un filtre, et permet de n'avoir à mener l'étude complète du temps de vie du phonon LO que sur un nombre très restreint de matériaux. En effet, son calcul via des méthodes *ab initio*, nommément ici, la DFPT, est très couteuse en temps de calcul et augmente avec le cube du nombre d'électrons de valence dans l'approximation des pseudopotentiels. Il requiert entre autres la détermination de la dérivée troisième de l'énergie totale par rapport au déplacement atomique, le *tenseur anharmonique du troisième ordre*. Une analyse des états finaux dans les super-réseaux montre que la connaissance de cette quantité est primordiale pour éliminer des canaux dits "fantôme", plus généralement pour déterminer le poids précis de chacun des canaux lors de l'intégration de tous les processus possible, c'est à dire, enfin, pour être prédictif sur la valeur absolue du temps de vie, et non simplement sur sa dépendance en température.

La particularité de SiSn par rapport aux autres semiconducteurs étudiés est double : en plus d'une densité d'états finaux à deux phonons très réduite, ceux-ci sont confinés aux bords de la zone de Brillouin (figure 5). Une approximation systématiquement utilisée dans l'étude de la décomposition du phonon LO issu du refroidissement électronique est de considérer son vecteur d'onde comme nul. Alors qu'il est vérifié que cette approximation est pertinente pour tous les autres matériaux étudiés, il est montré qu'elle n'est pas valable dans le cas de SiSn : le nombre d'états finaux, et donc le temps de vie, se révèlent être très dépendant du vecteur d'onde initial.

Compte tenu du très faible nombre d'états finaux à deux phonons accessibles, une dis-

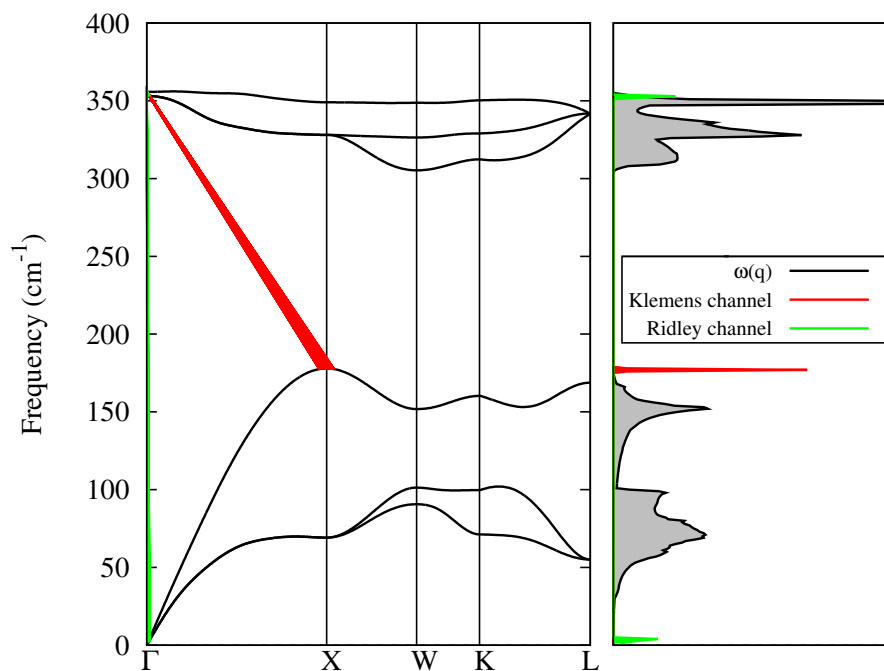


Figure 5: Gauche : structure de bande de SiSn (noir) et décomposition du phonon LO via les canaux de Klemens (rouge) et Ridley (vert). Droite : densités d'états à un phonon (noir) et à deux phonons (rouge et vert). L'amplitude des pics correspondant aux états Ridley (verts) a été multipliée par 10 pour des raisons de lisibilité.

cussion est menée sur la possibilité d'évaluer la contribution des décompositions de l'ordre supérieur, c'est à dire impliquant au total quatre phonons. Un tenseur anharmonique du quatrième ordre moyen est évalué, et le temps de vie associé à ces deux processus, ainsi qu'au processus total, est reporté sur la figure 6. La contribution du quatrième ordre, bien que délicate à manipuler, apparaît comme loin d'être négligeable, sans pour autant changer complètement l'ordre de grandeur du résultat final : le temps de vie du phonon LO est de respectivement 38 ou 108 ps à 300 K, suivant que sont incluses ou pas les contributions du quatrième ordre. Il convient d'insister sur le fait que la correction du quatrième ordre n'est qu'approximative, et que compte tenu des variations des tenseurs du troisième ordre, notamment au voisinage de Γ , est probablement légèrement surévaluée.

SiSn représentant, d'un point de vue de la densité d'états finaux à deux phonons, un cas presque idéal, ces résultats tendent à faire penser non seulement que se limiter à vouloir supprimer les canaux de décomposition au troisième ordre n'est pas suffisant, mais plus généralement que trouver un matériau ayant les caractéristiques décrites plus haut, *i.e.* un temps de vie de l'ordre de 100 ps, est une tâche dont la réalisation pratique peut être remise en question.

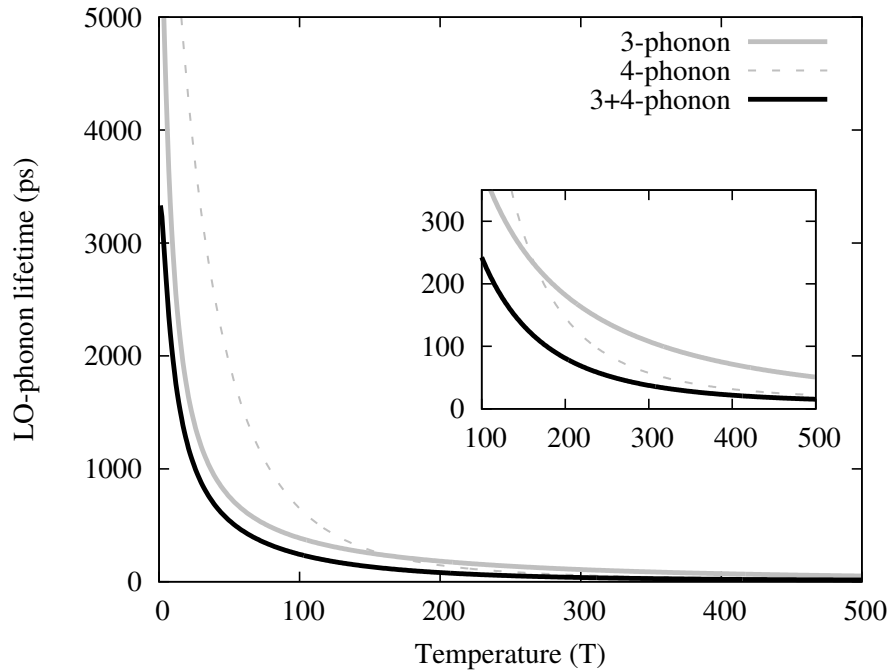


Figure 6: Temps de vie du phonon LO dans SiSn calculé en prenant en compte les processus à trois phonons seulement (trait plein gris), à quatre phonons seulement (trait gris en pointillé), ou la somme de ces deux processus (trait plein noir).

Cependant, il est fondamental de noter que dans l'état actuel de notre compréhension de ces mécanismes, il n'y a aucune raison de penser que les phonons LO dans les matériaux dans lequel un ralentissement du refroidissement des porteurs a été mesuré [68, 54] présentent de tels temps de vie. La longueur de ce dernier est ainsi une condition *suffisante* mais *non nécessaire* à l'exaltation de l'effet porteur chaud.

Interaction électron-phonon dans les super-réseaux

Une étude de l'interaction électron-phonon LO est menée dans le domaine intermédiaire entre le bulk et les puits quantiques que constituent les super-réseaux. Il se caractérisent par une périodicité dans une direction inférieure à environ 40 Å, longueur caractéristique qui dépend évidemment du matériau en question. La relative petite taille de la cellule primitive permet une approche *ab initio*. Le modèle mis en place relie la constante de couplage au champ électrique macroscopique induit par le phonon LO, et permet de rendre compte de sa variation en fonction du vecteur d'onde du phonon échangé : cela donne accès à une étude de l'interaction électron-phonon résolue en angle. Le système choisi est le super-réseau $[InAs]_n[GaAs]_n$.

L'étude consiste à laisser une population d'électrons chauds refroidir via des proces-

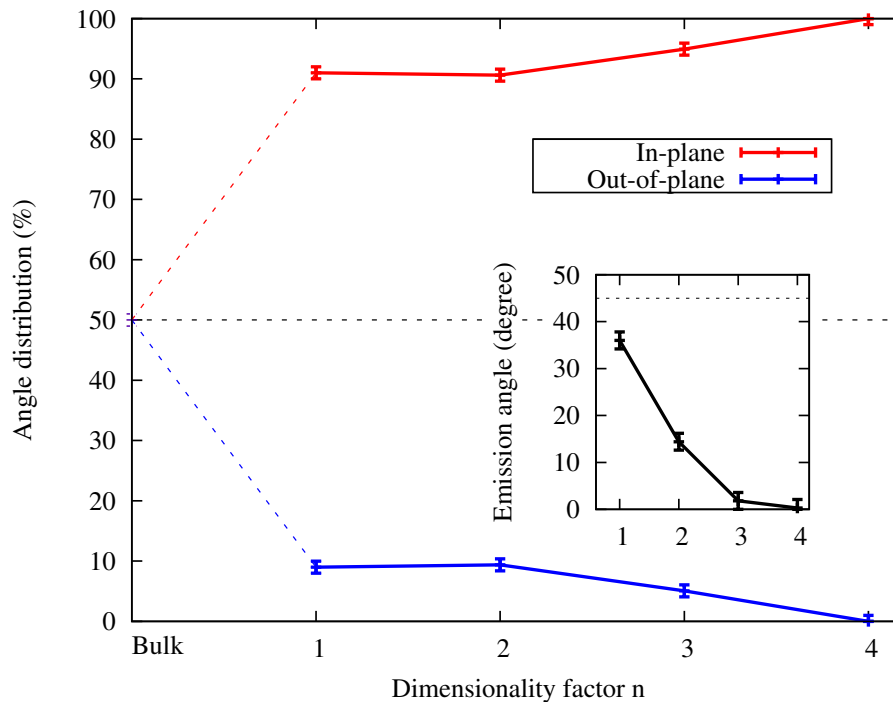


Figure 7: Proportion de phonons émis ayant une composante dans le plan (rouge) et perpendiculaire au plan (bleu), en fonction du facteur de dimensionnalité n . La ligne en pointillé noire représente le comportement bulk. La variation du cône d'émission en fonction de n est tracé sur la figure en insertion.

sus intrabandes, de sorte que le phonon échangé à chaque interaction corresponde au couplage le plus fort : il s'agit d'une approche déterministe, ne cherchant à décrire qu'un comportement global, et se concentrant sur la dimensionnalité des interactions.

L'analyse des modes de vibrations LO amène à fixer la limite haute de n à 7, de sorte à ne pas basculer dans la gamme de taille des puits quantiques. Celle sur les angles d'émissions indique que, pour tout n , plus de 90% des phonons émis lors du refroidissement ont une composante perpendiculaire dominante, alors qu'elle est de 50% dans le cas bulk (figure 7). De plus, l'angle du cône d'émission de ces phonons par rapport à l'axe de croissance du super-réseau décroît quand n augmente, et est calculé proche de 0° pour $n \geq 4$.

Conclusions générales et perspectives

Cette thèse s'est concentrée sur les problématiques liées aux phonons dans les cellules solaires à porteurs chauds, et en particulier celles relatives au phonon-LO, dont il a été rappelé qu'elles sont fortement liées à celle du refroidissement des porteurs.

La décomposition du phonon LO a d'abord été étudiée en terme d'états finaux finaux

disponibles. La pertinence de certains critères dans la recherche de candidats absorbeurs a été ré-affirmé. Il a également été montré que la recherche de gaps dans la densité d'états de phonons est plus pertinente dans les matériaux bulk que dans les nanostructures, même de taille subnanométrique.

L'étude s'est poursuivie avec le calcul du temps de vie du phonon LO dans un matériau présentant des caractéristiques particulières du point de vue des critères déterminés au chapitre précédent, SiSn dans la phase cubique face centrée. La nécessité d'un calcul *ab initio* pour palier le caractère non-prédictif voire faussant de certaines approximations très répandues a été démontré. Il s'est avéré que, dans un processus à trois phonons, ce temps de vie est très dépendant du vecteurs d'onde du phonon LO initial, comportement jusqu'alors jamais observé dans aucun autre matériau. La question d'inclure dans le taux de décomposition total des processus à plus de trois phonons a été posée : une correction a été apportée en estimant la contribution des interactions à quatre phonons, et a révélé la difficulté pratique de trouver des matériaux dont le phonon LO auraient un temps de vie intrinsèque de l'ordre de 100 ps. Cependant, il est à noter que ce dernier point est une condition *suffisante* mais *non nécessaire*. Ces résultats tendent à faire penser que l'écrantage de l'interaction électron-phonon est la raison première, voire exclusive, de l'exaltation de l'effet porteurs chauds dans certains matériaux.

Cette même interaction a été examinée à l'échelle des super-réseaux. Plus spécifiquement, elle s'est concentrée sur la relation entre dimensionalité de la cellule cristalline et celle des populations électroniques et phononiques interagissantes. Un modèle a été proposé en ce sens pour lier la constante de couplage au champ électrique induit par le phonon LO. Il a été mis en évidence que l'anisotropie de cette interaction, dûe à celle du champ électrique, conduit à ce que les électrons chauds se refroidissent principalement via leur interaction avec des phonons orientés perpendiculairement à l'axe de croissance du super-réseau, même pour des tailles de cellule pour lesquelles il est encore pertinent de considérer des populations d'électrons chauds tridimensionnels. Ce résultat est prometteur pour les HCSC, puisqu'il suggère que la densité électronique requise pour exalter un effet porteurs chauds serait dans ce cas réduite comparé au matériau bulk.

La physique numérique peut revêtir un caractère soit philosophique, c'est à dire allant des faits expérimentaux vers les conceptualisation et théorisation, soit à l'inverse métaphysique, ne tentant qu'*a posteriori* de décrire des vérités empiriques à partir de concepts *ex mente*. De ce point de vue, les deux premiers chapitres sont substantiellement philosophique : d'une théorisation de la décomposition du phonon LO, expérimentalement suggérée, des prédictions ont été faites sur un matériau nouveau. Notre compréhension actuelle de ces phénomènes nous amène à penser que la découverte d'un matériau présentant les critères définis comme suffisant pour exalter l'effet porteur chaud est improbable.

De là suit logiquement l'examen de l'interaction porteur-phonon. La modeste introduction initiée dans le quatrième chapitre a elle un caractère plus métaphysique, en ce que la formulation du modèle a une forte composante intuitive et que les supports expérimentaux sont rares. Il est à souhaiter que ces quelques premiers résultats seront suivis d'études plus approfondies sur la pertinence des super-réseaux pour les HCSC.

De nouveaux outils d'analyse numérique des problématiques porteurs chauds ont été introduits par M. Bernardi *et al.* en juin 2014, dans un article publié dans la prestigieuse revue *Physical Review Letters* [173] : un calcul dynamique du refroidissement des électrons chauds dans le silicium est mené, incluant des calculs complètement *ab initio* de toutes les interactions électron-électron et électron-phonon. Un des résultats marquants est l'obtention du temps de vie des porteurs résolu en énergie et en vecteur d'onde (figure 8). Il y a fort à parier qu'un nouveau niveau de compréhension des interactions

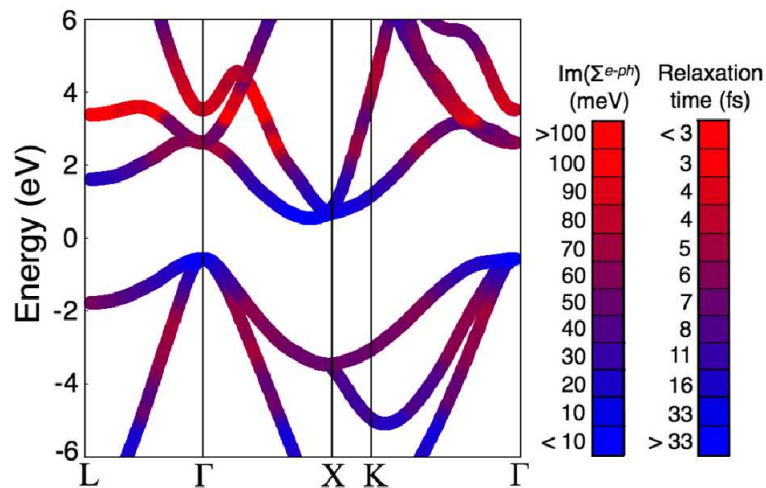


Figure 8: Structure de bande de Si. La couleur représente la partie imaginaire de la self-énergie de l'élément de matrice électron-phonon. Reproduit depuis [173].

électron-phonon discutées dans le premier chapitre sera atteint dans les prochaines années, et que la possibilité d'une *ingénierie de bandes électroniques* sera envisagée. Pour citer les derniers mots de l'introduction, cette étude "*ouvre la voie aux études ab initio des porteurs chauds dans les matériaux pour les énergies renouvelables*".

Bibliography

- [1] A. Luque, “Will we exceed 50% efficiency in photovoltaics ?,” *Journal of Applied Physics*, vol. 110, no. 3, pp. 031301–031301, 2011.
- [2] W. Shockley and H. J. Queisser, “Detailed balance limit of efficiency of p-n junction solar cells,” *Journal of applied physics*, vol. 32, no. 3, pp. 510–519, 1961.
- [3] R. T. Ross and A. J. Nozik, “Efficiency of hot-carrier solar energy converters,” *J. Appl. Phys.*, vol. 53, p. 3813, 1982.
- [4] P. Würfel and U. Würfel, *Physics of solar cells: from basic principles to advanced concepts*. John Wiley & Sons, 2009.
- [5] G. Kresse and J. Furthmüller, “Efficient iterative schemes for ab initio total-energy calculations using a plane-wave basis set,” *Physical Review B*, vol. 54, no. 16, p. 11169, 1996.
- [6] P. Giannozzi, S. Baroni, N. Bonini, M. Calandra, R. Car, C. Cavazzoni, D. Ceresoli, G. L. Chiarotti, M. Cococcioni, I. Dabo, A. D. Corso, S. de Gironcoli, S. Fabris, G. Fratesi, R. Gebauer, U. Gerstmann, C. Gougoussis, A. Kokalj, M. Lazzeri, L. Martin-Samos, N. Marzari, F. Mauri, R. Mazzarello, S. Paolini, A. Pasquarello, L. Paulatto, C. Sbraccia, S. Scandolo, G. Sclauzero, A. P. Seitsonen, A. Smogunov, P. Umari, and R. M. Wentzcovitch, “Quantum espresso: a modular and open-source software project for quantum simulations of materials,” *Journal of Physics: Condensed Matter*, vol. 21, no. 39, p. 395502, 2009.
- [7] A. L. Bris, *Etude de faisabilité de dispositifs photovoltaïques À porteurs chauds: conception, modélisation, caractérisation*. PhD thesis, Ecole Centrale Paris, 2011.
- [8] Y. Takeda and T. Motohiro, “Intermediate-band-assisted hot-carrier solar cells using indirect-bandgap absorbers,” *Progress in Photovoltaics: Research and Applications*, vol. 21, no. 6, pp. 1308–1318, 2013.
- [9] E. D. Jackson, “Areas for improvement of the semiconductor solar energy converter,” in *Transactions of the Conference on the Use of Solar Energy*, vol. 5, pp. 122–126, 1955.
- [10] A. Marti and G. L. Araújo, “Limiting efficiencies for photovoltaic energy conversion in multigap systems,” *Solar Energy Materials and Solar Cells*, vol. 43, no. 2, pp. 203–222, 1996.

- [11] M. A. Green, “Third generation photovoltaics: Ultra-high conversion efficiency at low cost,” *Progress in Photovoltaics: Research and Applications*, vol. 9, no. 2, pp. 123–135, 2001.
- [12] F. Dimroth, M. Grave, P. Beutel, U. Fiedeler, C. Karcher, T. N. B. Tibbits, E. Oliva, G. Siefer, M. Schachtner, A. Wekkeli, A. W. Bett, R. Krause, M. Piccin, N. Blanc, C. Drazek, E. Guiot, B. Ghyselen, T. Salvetat, A. Tauzin, T. Signamarcheix, A. Dobrich, T. Hannappel, and K. Schwarzburg, “Wafer bonded four-junction GaInP/GaAs/GaInAsP/GaInAs concentrator solar cells with 44.7% efficiency,” *Progress in Photovoltaics: Research and Applications*, vol. 22, no. 3, pp. 277–282, 2014.
- [13] G. Conibeer, “Third-generation photovoltaics,” *materialstoday*, vol. 10, November 2007.
- [14] A. J. Nozik, “Spectroscopy and hot electron relaxation dynamics in semiconductor quantum wells and quantum dots,” *Annual review of physical chemistry*, vol. 52, no. 1, pp. 193–231, 2001.
- [15] G. Conibeer and A. Willoughby, *Solar Cell Materials: Developing Technologies*. John Wiley & Sons, 2014.
- [16] A. Martí, E. Antolin, C. R. Stanley, C. D. Farmer, N. López, P. Diaz, E. Cánovas, P. G. Linares, and A. Luque, “Production of photocurrent due to intermediate-to-conduction-band transitions: a demonstration of a key operating principle of the intermediate-band solar cell,” *Physical Review Letters*, vol. 97, no. 24, p. 247701, 2006.
- [17] A. Shalav, B. S. Richards, and M. A. Green, “Luminescent layers for enhanced Silicon solar cell performance: up-conversion,” *Solar Energy Materials and Solar Cells*, vol. 91, no. 9, pp. 829–842, 2007.
- [18] C. Andriamiadamanana, A. Ferrier, L. Lombez, A.-L. Joudrier, N. Naghavi, P. Ghenuche, N. Bardou, J.-L. Pellouard, S. Collin, F. Pelle, and J.-F. Guillemoles, “Plasmonic enhancement of up-conversion in ultrathin layers,” in *SPIE OPTO*, pp. 825608–825608, International Society for Optics and Photonics, 2012.
- [19] S. A. Lyon, “Spectroscopy of hot carriers in semiconductors,” *Journal of luminescence*, vol. 35, no. 3, pp. 121–154, 1986.
- [20] J. F. Young, T. Gong, P. M. Fauchet, and P. J. Kelly, “Carrier-carrier scattering rates within nonequilibrium optically injected semiconductor plasmas,” *Physical Review B*, vol. 50, no. 4, p. 2208, 1994.
- [21] A. Othonos, “Probing ultrafast carrier and phonon dynamics in semiconductors,” *J. Appl. Phys.*, vol. 83, pp. 1789–1830, February 1998.
- [22] J. Rodière, *Caractérisation optoélectronique d’absorbeurs pour les cellules photovoltaïques à porteurs chauds*. PhD thesis, Université Pierre et Marie Curie, 2014.

- [23] I. Tamm, "Über die quantentheorie der molekularen lichtzerstreuung in festen körpern," *Zeitschrift für Physik*, vol. 60, no. 5-6, pp. 345–363, 1930.
- [24] C. L. Collins and P. Y. Yu, "Generation of nonequilibrium optical phonons in GaAs and their application in studying intervalley electron-phonon scattering," *Physical Review B*, vol. 30, no. 8, p. 4501, 1984.
- [25] R. Ulbrich, "Energy relaxation of photoexcited hot electrons in GaAs," *Physical Review B*, vol. 8, no. 12, p. 5719, 1973.
- [26] M. Born, K. Huang, M. Born, M. Born, G. Physicist, and G. Britain, *Dynamical theory of crystal lattices*. Clarendon Press Oxford, 1956.
- [27] B. K. Ridley, *Quantum Processes in Semiconductors*. Oxford University Press Inc., New York, fourth ed., 1999.
- [28] S. Zollner, S. Gopalan, and M. Cardona, "Microscopic theory of intervalley scattering in GaAs: k-dependence of deformation potentials and scattering rates," *Journal of Applied Physics*, vol. 68, no. 4, pp. 1682–1693, 1990.
- [29] H. Fröhlich, "Electrons in lattice fields," *Advances in Physics*, vol. 3, no. 11, pp. 325–361, 1954.
- [30] D. N. Mirlin, I. J. Karlik, L. P. Nikitin, I. I. Reshina, and V. F. Sapega, "Hot electron photoluminescence in GaAs crystals," *Solid State Communications*, vol. 37, no. 9, pp. 757–760, 1981.
- [31] D.-S. Kim and P. Y. Yu, "Hot-electron relaxations and hot phonons in GaAs studied by subpicosecond Raman scattering," *Physical Review B*, vol. 43, no. 5, p. 4158, 1991.
- [32] R. G. Ulbrich, J. A. Kash, and J. C. Tsang, "Hot-electron recombination at neutral acceptors in GaAs: A cw probe of femtosecond intervalley scattering," *Physical review letters*, vol. 62, no. 8, p. 949, 1989.
- [33] J. Shah, B. Deveaud, T. C. Damen, W. T. Tsang, A. C. Gossard, and P. Lugli, "Determination of intervalley scattering rates in GaAs by subpicosecond luminescence spectroscopy," *Physical review letters*, vol. 59, no. 19, p. 2222, 1987.
- [34] D. N. Mirlin, I. Y. Karlik, and V. F. Sapega, "Intervalley Γ -X scattering rate in Gallium Arsenide crystals," *Solid state communications*, vol. 65, no. 3, pp. 171–172, 1988.
- [35] S. Zollner, S. Gopalan, and M. Cardona, "Intervalley deformation potentials and scattering rates in Zinc-Blende semiconductors," *Applied physics letters*, vol. 54, no. 7, pp. 614–616, 1989.
- [36] S. Zollner, S. Gopalan, and M. Cardona, "Effective intervalley deformation potentials in the description of time-resolved and hot-electron luminescence," *Solid state communications*, vol. 76, no. 7, pp. 877–879, 1990.
- [37] S. Zollner, S. Gopalan, and M. Cardona, "Intervalley scattering times from the rigid-pseudion method," in *Semi-DL tentative*, pp. 78–85, International Society for Optics and Photonics, 1990.

- [38] S. Zollner, S. Gopalan, and M. Cardona, "Short-range deformation-potential interaction and its application to ultrafast processes in semiconductors," *Semiconductor Science and Technology*, vol. 7, no. 3B, p. B137, 1992.
- [39] J. L. Birman, M. Lax, and R. Loudon, "Intervalley-scattering selection rules in III-V semiconductors," *Physical Review*, vol. 145, no. 2, p. 620, 1966.
- [40] J. Sjakste, V. Tyuterev, and N. Vast, "Ab initio study of Γ -X intervalley scattering in GaAs under pressure," *Physical Review B*, vol. 74, no. 23, p. 235216, 2006.
- [41] J. Sjakste, V. Tyuterev, and N. Vast, "Intervalley scattering in GaAs: ab initio calculation of the effective parameters for Monte Carlo simulations," *Applied Physics A*, vol. 86, no. 3, pp. 301–307, 2007.
- [42] J. Sjakste, N. Vast, and V. Tyuterev, "Ab initio method for calculating electron-phonon scattering times in semiconductors: application to GaAs and GaP," *Physical review letters*, vol. 99, no. 23, p. 236405, 2007.
- [43] P. G. Klemens, "Anharmonic decay of optical phonons," *Physical Review*, vol. 148, no. 2, p. 845, 1966.
- [44] E. Tea, H. Hamzeh, and F. Aniel, "Hot carriers relaxation in highly excited polar semiconductors: hot phonons versus phonon-plasmon coupling," *J. Appl. Phys.*, vol. 110, no. 113108, 2011.
- [45] P. Lugli and S. M. Goodnick, "Nonequilibrium longitudinal-optical phonon effects in GaAs-AlGaAs quantum wells," *Physical review letters*, vol. 59, no. 6, p. 716, 1987.
- [46] P. Lugli, P. Bordone, S. Gualdi, P. Poli, and S. M. Goodnick, "Hot phonons in quantum wells systems," *Solid-state electronics*, vol. 32, no. 12, pp. 1881–1885, 1989.
- [47] P. Langot, N. D. Fatti, D. Christofilos, R. Tommasi, and F. Vallée, "Femtosecond investigation of the hot-phonon effect in GaAs at room temperature," *Phys. Rev. B*, vol. 54, November 1996.
- [48] E. Tea, *Résolution de l'Equation de Transport de Boltzmann par une approche Monte Carlo (Full-Band), application aux Cellules Solaires à Porteurs Chauds et aux composants ultra-rapides*. Supervisor : F. aniel, Université Paris-Sud 11, Paris, December 2011.
- [49] S. Barman and G. P. Strivastava, "Lifetime of nonequilibrium zone-center longitudinal optical phonons in Zinc-Blende materials," *Appl. Phys. Lett.*, vol. 81, no. 18, 2002.
- [50] A. L. Bris and J.-F. Guillemoles, "Hot carrier solar cells: achievable efficiency accounting for heat losses in the absorber and through contacts," *Appl. Phys. Lett.*, vol. 97, p. 113506, 2010.
- [51] C. Hu, *Hot carrier effects*, vol. 18. 1989.
- [52] E. Takeda, C. Y.-W. Yang, and A. Miura-Hamada, *Hot-carrier effects in MOS devices*. Academic Press, 1995.

- [53] A. J. Nozik, "Quantum dot solar cells," *Physica E: Low-dimensional Systems and Nanostructures*, vol. 14, no. 1, pp. 115–120, 2002.
- [54] Y. Rosenwaks, M. C. Hanna, D. H. Levi, D. M. Szmyd, R. K. Ahrenkiel, and A. J. Nozik, "Hot-carrier cooling in GaAs: Quantum wells versus bulk," *Phys. Rev. B*, vol. 48, no. 19, p. 14675, 1993.
- [55] P. Würfel, A. S. Brown, T. E. Humphrey, and M. A. Green, "Particle conservation in the hot-carrier solar cell," *Prog. Photovolt: Res. Appl.*, vol. 13, pp. 277–285, February 2005.
- [56] Y. Takeda, T. Ito, T. Motohiro, D. König, S. Shrestha, and G. Coonibeer, "Hot-carrier solar cell operating under practical conditions," *J. Appl. Phys.*, vol. 105, p. 074905, 2009.
- [57] A. L. Bris, J. Rodiere, C. Colin, S. Collin, J.-L. Pelouard, R. Esteban, M. Laroche, J.-J. Greffet, and J.-F. Guillemoles, "Hot carrier solar cells: Controlling thermalization in ultrathin devices," *Photovoltaics, IEEE Journal of*, vol. 2, no. 4, pp. 506–511, 2012.
- [58] C. Delerue and M. Lannoo, *Nanostructures: Theory and Modelling*. Springer, 2004.
- [59] L. L. Chang, L. Esaki, and R. Tsu, "Resonant tunneling in semiconductor double barriers," *Applied Physics Letters*, vol. 24, no. 12, pp. 593–595, 1974.
- [60] S. Yagi and Y. Okada, "Fabrication of resonant tunneling structures for selective energy contact of hot-carrier solar cell based on III–V semiconductors," in *Photovoltaic Specialists Conference (PVSC), 2010 35th IEEE*, pp. 001213–001216, IEEE, 2010.
- [61] J. A. R. Dimmock, D. Stephen, M. Kauer, K. Smith, and J. Heffernan, "Demonstration of a hot-carrier photovoltaic cell," *Progress in Photovoltaics: Research and Applications*, vol. 22, no. 2, pp. 151–160, 2014.
- [62] J. Wu and Z. M. Wang, *Quantum Dot Solar Cells*. 2013.
- [63] G. J. Conibeer, C.-W. Jiang, D. König, S. Shrestha, T. Walsh, and M. A. Green, "Selective energy contacts for hot-carrier solar cells," *Thin Solid Films*, vol. 516, no. 20, pp. 6968–6973, 2008.
- [64] D. König, D. Hiller, M. Zacharias, S. Michard, and C. Flynn, "Static hot carrier populations as a function of optical excitation energy detected through energy selective contacts by optically assisted IV," *Progress in Photovoltaics: Research and Applications*, 2013.
- [65] A. Delamarre, *Développement de nouvelles méthodes de caractérisation optoélectroniques des cellules solaires*. PhD thesis, Paris 6, 2013.
- [66] J. F. Ryan, R. A. Taylor, A. J. Turberfield, A. Maciel, J. M. Worlock, A. C. Gosard, and W. Wiegmann, "Time-resolved photoluminescence of two-dimensional hot carriers in GaAs-AlGaAs heterostructures," *Physical review letters*, vol. 53, no. 19, p. 1841, 1984.

- [67] A. J. Nozik, C. A. Parsons, D. J. Dunlavy, B. M. Keyes, and R. K. Ahrenkiel, "Dependence of hot carrier luminescence on barrier thickness in GaAs/AlGaAs superlattices and multiple quantum wells," *Solid State Communications*, vol. 75, pp. 297–301, 1990.
- [68] W. S. Pelouch, R. J. Ellingson, P. E. Powers, and C. L. Tang, "Comparison of hot-carrier relaxation in quantum wells and bulk GaAs at high carrier densities," *Phys. Rev. B*, vol. 45, p. 3, 1992.
- [69] J. Shah, B. K. Ridley, S. D. Sarma, W. Pötz, P. Kocevar, A. P. Jauho, F. Rossi, R. Brunetti, C. Jacoboni, S. M. Goodnick, P. Lugli, I. C. Kizilyalli, K. Hess, W. H. Knox, J. F. Ryan, M. C. Tatham, R. A. Höpfel, S. Juen, M. Heiblum, U. Sivan, N. Yokoyama, and E. R. Brown, *Hot Carriers In Semiconductor Nanostructures: Physics and Applications*. Harcourt Brace Jovanovich, 1992.
- [70] K. Leo, W. Rühle, and K. Ploog, "Hot-carrier energy-loss rates in GaAs/ $Al_xGa_{1-x}As$ quantum wells," *Physical Review B*, vol. 38, no. 3, p. 1947, 1988.
- [71] W. W. Rühle, K. Leo, and E. Bauser, "Cooling of a hot electron-hole plasma in $Al_xGa_{1-x}As$," *Physical Review B*, vol. 40, no. 3, p. 1756, 1989.
- [72] J. Shah, A. Pinczuk, A. C. Gossard, and W. Wiegmann, "Energy-loss rates for hot electrons and holes in GaAs quantum wells," *Physical review letters*, vol. 54, no. 18, p. 2045, 1985.
- [73] C. V. Shank, R. L. Fork, R. Yen, J. Shah, B. I. Greene, A. C. Gossard, and C. Weisbuch, "Picosecond dynamics of hot-carrier relaxation in highly excited multi-quantum well structures," *Solid state communications*, vol. 47, no. 12, pp. 981–983, 1983.
- [74] K. Leo, W. Rühle, H. Queisser, and K. Ploog, "Reduced dimensionality of hot-carrier relaxation in GaAs quantum wells," *Physical Review B*, vol. 37, no. 12, p. 7121, 1988.
- [75] K. Leo, W. W. Rühle, H. J. Queisser, and K. Ploog, "Hot carrier cooling in GaAs quantum wells," *Applied Physics A*, vol. 45, no. 1, pp. 35–39, 1988.
- [76] M. E. Vallone, "Quantum well electron scattering rates through longitudinal optic-phonon dynamical screened interaction: an analytic approach," *Journal of Applied Physics*, vol. 114, no. 5, p. 053704, 2013.
- [77] A. L. Bris, L. Lombez, S. L. G., Boissier, P. Christol, and J.-F. Guillemoles, "Thermalisation rate study of GaSb-based heterostructures by continuous wave photoluminescence and their potential as hot carrier solar cell absorbers," *Energy & Environmental Science*, vol. 5, no. 3, pp. 6225–6232, 2012.
- [78] M. Neges, K. Schwarzburg, and F. Willig, "Monte Carlo simulation of energy loss and collection of hot charge carriers, first step towards a more realistic hot-carrier solar energy converter," *Solar energy materials and solar cells*, vol. 90, no. 14, pp. 2107–2128, 2006.

- [79] Y. Feng, S. Lin, M. Green, and G. Conibeer, “Effect of static carrier screening on the energy relaxation of electrons in polar-semiconductor multiple-quantum-well superlattices,” *Journal of Applied Physics*, vol. 113, no. 2, p. 024317, 2013.
- [80] G. J. Conibeer, D. König, M. A. Green, and J. F. Guillemoles, “Slowing of carrier cooling in hot-carrier solar cells,” *Thin Solid Films*, vol. 516, pp. 6948–6953, 2008.
- [81] Y. Yao, D. König, and M. Green, “Investigation of Boron Antimonide as hot-carrier absorber material,” *Solar Energy Materials and Solar Cells*, vol. 111, pp. 123–126, 2013.
- [82] J. W. Pomeroy, M. Kuball, H. Lu, W. J. Schaff, X. Wang, and A. Yoshikawa, “Phonon lifetimes and phonon decay in InN,” *Applied Physics Letters*, vol. 86, no. 22, pp. 223501–223501, 2005.
- [83] G. Conibeer, R. Patterson, L. Huang, J.-F. Guillemoles, D. König, S. Shrestha, and M. A. Green, “Modeling of hot-carrier solar cell absorbers,” *Solar Energy Materials & Solar Cells*, vol. 94, pp. 1516–1521, 2010.
- [84] R. Patterson, M. Kirkengen, B. P. Veetil, D. König, M. A. Green, and G. Conibeer, “Phonon lifetimes in model quantum dot superlattice systems with applications to the hot-carrier solar cell,” *Solar Energy Materials & Solar Cells*, vol. 94, pp. 1931–1935, 2010.
- [85] K. T. Tsen and D. K. Ferry, “Studies of electron–phonon and phonon–phonon interactions in InN using ultrafast Raman spectroscopy,” *Journal of Physics: Condensed Matter*, vol. 21, no. 17, p. 174202, 2009.
- [86] P. Aliberti, Y. Feng, S. K. S. ans M. A. Green, G. Conibeer, L. W. Tu, and P. H. Tseng, “Effect of non-ideal energy selective contacts and experimental carrier cooling rate on the performance of an indium nitride based hot carrier solar cell,” *Appl. Phys. Lett.*, vol. 99, p. 223507, 2011.
- [87] EU-PVSEC, ed., *Hot carrier solar cells: choice of materials for efficiency and abundance*, vol. 26, EU-PVSEC, September 2011.
- [88] B. K. Ridley, “The lo phonon lifetime in GaN,” *Journal of Physics: Condensed Matter*, vol. 8, no. 37, pp. L511–L513, 1996.
- [89] P. Carruthers, “Theory of thermal conductivity of solids at low temperatures,” *Reviews of Modern Physics*, vol. 33, no. 1, p. 92, 1961.
- [90] D. K. Ferry, “Decay of polar-optical phonons in semiconductors,” *Phys. Rev. B*, vol. 9, pp. 4277–4280, May 1974.
- [91] D. G. Cahill, W. K. Ford, K. E. Goodson, G. D. Mahan, A. Majumdar, H. J. Maris, R. Merlin, and S. R. Phillpot, “Nanoscale thermal transport,” *J. Appl. Phys.*, vol. 93, January 2003.
- [92] C. H. W. Barnes, J. M. Shilton, and A. M. Robinson, “Quantum computation using electrons trapped by surface acoustic waves,” *Phys. Rev. B*, vol. 62, no. 12, p. 8410, 2000.

- [93] G. Chen, T. Zeng, T. Borca-Tasciuc, and D. Sond, "Phonon engineering in nanostructures for solid-state energy conversion," *Materials Science and Engineering*, vol. A292, pp. 155–161, 2000.
- [94] D. Vashaee and A. Shakouri, "Electronic and thermoelectric transport in semiconductor and metallic superlattices," *J. Appl. Phys.*, vol. 95, February 2004.
- [95] D. Vashaee and A. Shakouri, "Thermionic power generation at high temperature using SiGe/Si superlattices," *J. Appl. Phys.*, vol. 101, March 2007.
- [96] L. Fara, *Advanced Solar Cell Materials, Technology, Modeling, and Simulation*. IGI Global, 2013.
- [97] S. Baroni, S. de Gironcoli, and A. D. Corso, "Phonons and related crystal properties from density-functional perturbation theory," *Rev. Mod. Phys.*, vol. 73, p. 515, April 2001.
- [98] C. Kittel and P. McEuen, *Introduction to solid state physics*, vol. 8. Wiley New York, 1976.
- [99] P. Giannozzi, S. D. Gironcoli, P. Pavone, and S. Baroni, "Ab initio calculation of phonon dispersions in semiconductors," *Physical Review B*, vol. 43, no. 9, p. 7231, 1991.
- [100] P. Y. Yu and M. Cardona, *Fundamentals of semiconductors*. Springer, 1996.
- [101] A. S. Henry and G. Chen, "Spectral phonon transport properties of Silicon based on molecular dynamics simulations and lattice dynamics," *Journal of Computational and Theoretical Nanoscience*, vol. 5, no. 2, pp. 141–152, 2008.
- [102] G. P. Strivastava, *The Physics Of Phonons*. Tayloer & Francis Group, 1990.
- [103] S. Barman and G. P. Strivastava, "Long-wavelength nonequilibrium optical phonon dynamics in cubic and hexagonal semiconductors," *Phys. Rev. B*, vol. 69, no. 235208, 2004.
- [104] A. Debernardi, "Phonon linewidth in III-V semiconductors from density-functional perturbation theory," *Phys. Rev. B*, vol. 57, no. 20, p. 12847, 1998.
- [105] A. Debernardi, C. Ulrich, K. Syassen, and M. Cardona, "Raman linewidths of optical phonons in 3C-SiC under pressure: First-principles calculations and experimental results," *Phys. Rev. B*, vol. 59, no. 10, p. 6774, 1999.
- [106] M. Canonico, C. Poweleit, J. Menedez, A. Debernardi, S. R. Johnson, and Y.-H. Zhang, "Anomalous lo phonon lifetime in AlAs," *Phys. Rev. Lett.*, vol. 88, p. 215502, 2002.
- [107] F. Vallée, "Time-resolved investigation of coherent LO-phonon relaxation in III-V semiconductors," *Phys. Rev. B*, vol. 49, no. 4, p. 2460, 1994.
- [108] G. Conibeer, R. C. M. Green and, E.-C. C. Y. Cho, C.-W. Jiang, T. Fangsuwannarak, E. Pink, Y. Huang, T. Puzzer, T. Trupke, B. Richards, A. Shalav, and K.-L. Lin,

- “Silicon nanostructures for third generation photovoltaic solar cells,” *Thin Solid Films*, vol. 511-512, pp. 654–662, 2006.
- [109] R. Patterson, *Phononic Modelling of Nanostructures for the Hot-Carrier Solar Cell*. Supervisor : D. conibeer, 2011.
- [110] P. Giannozzi and S. Baroni, “Density-functional perturbation theory,” in *Handbook of Materials Modeling*, pp. 195–214, Springer, 2005.
- [111] H. Hellmann, “Einführung in die Quantenchemie,” 1937.
- [112] R. P. Feynman, “Forces in molecules,” *Physical Review*, vol. 56, no. 4, p. 340, 1939.
- [113] X. Gonze, “Perturbation expansion of variational principles at arbitrary order,” *Physical Review A*, vol. 52, no. 2, p. 1086, 1995.
- [114] D. Strauch and B. Dorner, “Phonon dispersion in GaAs,” *J. P.*, vol. 2, pp. 1457–1474, 1990.
- [115] P. Pavone, S. Baroni, and S. de Gironcoli, “ α - β phase transition in tin: a theoretical study based on density-functional perturbation theory,” *Physical Review B*, vol. 57, no. 17, p. 10421, 1998.
- [116] B. Jusserand, F. Mollot, R. Planel, E. Molinari, and S. Baroni, “Atomic intermixing in short period GaAs/AlAs superlattices,” *Surface science*, vol. 267, no. 1, pp. 171–175, 1992.
- [117] K. Persson, M. Ekman, and G. Grimvall, “Dynamical and thermodynamical instabilities in the disordered $\text{Re}_x\text{W}_{1-x}$ system,” *Physical Review B*, vol. 60, no. 14, p. 9999, 1999.
- [118] J.-A. Yan, W. Y. Ruan, and M. Y. Chou, “Phonon dispersions and vibrational properties of monolayer, bilayer, and trilayer graphene: Density-functional perturbation theory,” *Physical Review B*, vol. 77, no. 12, p. 125401, 2008.
- [119] N. G. Szewacki, A. Sadrzadeh, and B. I. Yakobson, “B 80 Fullerene: an ab initio prediction of geometry, stability, and electronic structure,” *Physical review letters*, vol. 98, no. 16, p. 166804, 2007.
- [120] E. Molinari, S. Baroni, P. Giannozzi, and S. de Gironcoli, “Effects of disorder on the raman spectra of GaAs/AlAs superlattices,” *Physical Review B*, vol. 45, no. 8, p. 4280, 1992.
- [121] M. Lazzeri and S. de Gironcoli, “Ab initio study of Be (0001) surface thermal expansion,” *Physical review letters*, vol. 81, no. 10, p. 2096, 1998.
- [122] S. Baroni, P. Giannozzi, and E. Isaev, “Density-functional perturbation theory for quasi-harmonic calculations,” *Reviews in Mineralogy and Geochemistry*, vol. 71, pp. 3,39–58, 2010.
- [123] N. Vast and S. Baroni, “Effects of isotopic disorder on the Raman spectra of crystals: theory and ab initio calculations for Diamond and Germanium,” *Physical Review B*, vol. 61, no. 14, p. 9387, 2000.

- [124] L. Paulatto, F. Mauri, and M. Lazzeri, “Anharmonic properties from a generalized third-order ab initio approach: theory and applications to graphite and graphene,” *Physical Review B*, vol. 87, no. 21, p. 214303, 2013.
- [125] E. Haro-Poniatowski, J. L. Escamilla-Reyes, and K. H. Wanser, “Anharmonic calculations of the optical-phonon lifetime for crystals with the Diamond structure,” *Phys. Rev. B*, vol. 53, no. 18, p. 12121, 1996.
- [126] G. P. Srivastava, “Origin of the hor phonon effect in group-III nitrides,” *Phys. Rev. B*, vol. 77, no. 155205, 2008.
- [127] H. Hamzeh and F. Aniel, “Monte Carlo study of phonon dynamics in III-V compounds,” *J. Appl. Phys.*, vol. 109, p. 063511, 2011.
- [128] P. H. Borchers, G. F. Alfrey, A. D. B. Woods, and D. H. Saunderson, “Phonon dispersion curves in Indium Phosphide,” *Journal of Physics C: Solid State Physics*, vol. 8, no. 13, p. 2022, 1975.
- [129] A. Mooradian and G. B. Wright, “First order Raman effect in III-V compounds,” *Solid State Communications*, vol. 4, no. 9, pp. 431–434, 1966.
- [130] J. L. Yarnell, J. L. Warren, R. G. Wenzel, and P. J. Dean, “Neutron inelastic scattering,” *Vol. IIAEA, Vienna*, p. 301, 1968.
- [131] M. K. Farr, J. G. Traylor, and S. K. Sinha, “Lattice dynamics of GaSb,” *Physical Review B*, vol. 11, no. 4, p. 1587, 1975.
- [132] A. Onto, “Proceedings of the Tenth International Conference on the Physics of Semiconductors, Cambridge, Mass., 1970,” p. 107, 1970.
- [133] B. Monemar, “Fundamental energy gaps of AlAs and AlP from photoluminescence excitation spectra,” *Physical Review B*, vol. 8, no. 12, p. 5711, 1973.
- [134] D. Strauch, B. Dorner, K. Karch, S. Hunklinger, W. Ludwig, and G. Weiss, “Proceedings of the Third International Conference on Phonon Physics, Heidelberg, 1989,” 1990.
- [135] K. Kunc, M. Balkanski, and M. A. Nusimovici, “Lattice dynamics of several A_nB_{8-N} compounds having the Zinc-Blende structure. II. Numerical calculations,” *physica status solidi (b)*, vol. 72, no. 1, pp. 229–248, 1975.
- [136] F. Vallée and F. Bogani, “Coherent time-resolved investigation of LO-phonon dynamics in GaAs,” *Phys. Rev. B*, vol. 43, no. 14, p. 12049, 1991.
- [137] A. Debernardi, “Anharmonic effects in the phonons of III-V semiconductors: first principles calculations,” *Solid State Communications*, vol. 113, pp. 1–10, 2000.
- [138] B. Jusserand, D. Paquet, and A. Regreny, “"folded" optical phonons in GaAs $Ga_{1-x}Al_xAs$ superlattices,” *Physical Review B*, vol. 30, no. 10, p. 6245, 1984.
- [139] C. Colvart, T. A. Gant, M. V. Klein, R. Merlin, R. Fischer, H. Morkoc, and A. C. Gossard, “Folded acoustic and quantized optic phonons in (GaAl)As superlattices,” *Phys. Rev. B*, vol. 31, February 1985.

- [140] B. Jusserand, F. Alexandre, D. Paquet, and G. L. Roux, "Raman scattering characterization of interface broadening in GaAs/AlAs short period superlattices grown by molecular beam epitaxy," *Applied Physics Letters*, vol. 47, no. 3, pp. 301–303, 1985.
- [141] J. Sapriel and B. D. Rouhani, "Vibrations in superlattices," *Surface Science Reports*, vol. 10, no. 4, pp. 189–275, 1989.
- [142] V. Lemos, O. Pilla, and M. Montagna, "Direct observation of the acoustic gaps in Ge/Ge(x)Si(1-x) superlattices," *J. Raman Spectrosc.*, vol. 30, pp. 379–383, 1999.
- [143] H. D. Fuchs, C. H. Grein, R. I. Devlen, J. Kuhl, and M. Cardona, "Anharmonic decay time, isotopic scattering time, and inhomogeneous line broadening of optical phonons in Ge70, Ge76, and natural Ge crystals," *Physical Review B*, vol. 44, no. 16, p. 8633, 1991.
- [144] A. Debernardi, *Anharmonic Properties of Semiconductors from Density-Functional Perturbation Theory*. Supervisor : S. baroni, Scuola Internazionale Superiore di Studi Avanzati, Trieste, October 1995.
- [145] K. T. Tsen, J. G. Kiang, D. K. Ferry, and H. Morkoc, "Subpicosecond time-resolved Raman studies of lo phonons in GaN: Dependence on photoexcited carrier density," *Applied physics letters*, vol. 89, no. 11, pp. 112111–112111, 2006.
- [146] A. Dyson and B. K. Ridley, "Phonon-plasmon coupled-mode lifetime in semiconductors," *Journal of Applied Physics*, vol. 103, no. 11, p. 114507, 2008.
- [147] H. Bruus and K. Flensburg, *Many-body quantum theory in condensed matter physics*, vol. 198566336. Oxford University Press Oxford, 2004.
- [148] M. D. M. A. Stroschio, *Phonons in Nanostructures*. Cambridge University Press, 2005.
- [149] A. R. Bhatt, K. W. Kim, and M. A. Stroschio, "Theoretical calculation of longitudinal-optical-phonon lifetime in GaAs," *J. Appl. Phys.*, vol. 76, no. 6, 1994.
- [150] B. K. Ridley and R. Gupta, "Nonelectronic scattering of longitudinal-optical phonons in bulk polar semiconductors," *Phys. Rev. B*, vol. 43, no. 6, p. 4939, 1991.
- [151] A. Debernardi and S. Baroni, "Third-order density-functional perturbation theory: A practical implementation with applications to anharmonic couplings in Si," *Solid state communications*, vol. 91, no. 10, pp. 813–816, 1994.
- [152] P. Maly, A. C. Maciel, J. F. Ryan, and N. J. M. P. J. Walker, "Time-resolved Raman measurement of intervalley scattering in GaSb," *Semicond. Sci. Technol.*, vol. 9, pp. 719–721, 1994.
- [153] A. Debernardi, S. Baroni, and E. Molinari, "Anharmonic phonon lifetime in semiconductors from density-functional perturbation theory," *Phys. Rev. Lett.*, vol. 75, no. 9, p. 1819, 1995.

- [154] J.-M. Ziman, *Electrons and phonons: the theory of transport phenomena in solids*. Clarendon Press Oxford, UK, 2001.
- [155] J. Menéndez and M. Cardona, “Temperature dependence of the first-order Raman scattering by phonons in Si, Ge, and α -Sn: Anharmonic effects,” *Physical Review B*, vol. 29, no. 4, p. 2051, 1984.
- [156] M. Balkanski, R. F. Wallis, and E. Haro, “Anharmonic effects in light scattering due to optical phonons in Silicon,” *Phys. Rev. B*, vol. 28, no. 4, p. 1928, 1983.
- [157] D. Vanderbilt, S. G. Louis, and M. L. Cohen, “Calculation of anharmonic phonon couplings in C, Si, and Ge,” *Phys. Rev. B*, vol. 33, no. 12, p. 8740, 1986.
- [158] D. Alfè, “PHON: a program to calculate phonons using the small displacement method,” *Computer Physics Communications*, vol. 180, no. 12, pp. 2622–2633, 2009.
- [159] A. Dyson and B. K. Ridley, “The role of the products of the decay of optical phonons,” *Applied Physics Letters*, vol. 102, no. 4, p. 042108, 2013.
- [160] G. Leibfried and W. Ludwig, “Theory of anharmonic effects in crystals,” *Solid state physics*, vol. 12, pp. 275–444, 1961.
- [161] L. Lindsay, D. A. Broido, and N. Mingo, “Flexural phonons and thermal transport in Graphene,” *Physical Review B*, vol. 82, no. 11, p. 115427, 2010.
- [162] I. Vurgaftman, J. R. Meyer, and L. R. Ram-Mohan, “Band parameters for III–V compound semiconductors and their alloys,” *Journal of applied physics*, vol. 89, no. 11, pp. 5815–5875, 2001.
- [163] G. D. Mahan, *Many-particle physics*. Springer, 2000.
- [164] M. A. L. Marques and E. K. U. Gross, “Time-dependent density functional theory,” *Annu. Rev. Phys. Chem.*, vol. 55, pp. 427–455, 2004.
- [165] X. Gonze and C. Lee, “Dynamical matrices, born effective charges, dielectric permittivity tensors, and interatomic force constants from density-functional perturbation theory,” *Physical Review B*, vol. 55, no. 16, p. 10355, 1997.
- [166] W. Fawcett, A. D. Boardman, and S. Swain, “Monte Carlo determination of electron transport properties in Gallium Arsenide,” *Journal of Physics and Chemistry of solids*, vol. 31, no. 9, pp. 1963–1990, 1970.
- [167] P. E. Blöchl, “Projector augmented-wave method,” *Physical Review B*, vol. 50, no. 24, p. 17953, 1994.
- [168] N. Marzari and D. Vanderbilt, “Maximally localized generalized Wannier functions for composite energy bands,” *Physical review B*, vol. 56, no. 20, p. 12847, 1997.
- [169] I. Souza, N. Marzari, and D. Vanderbilt, “Maximally localized Wannier functions for entangled energy bands,” *Physical Review B*, vol. 65, no. 3, p. 035109, 2001.
- [170] A. A. Mostofi, J. R. Yates, Y.-S. Lee, I. Souza, D. Vanderbilt, and N. Marzari, “wannier90: a tool for obtaining maximally-localised Wannier functions,” *Computer Physics Communications*, vol. 178, no. 9, pp. 685–699, 2008.

- [171] S. Adachi, “Band gaps and refractive indices of AlGaAsSb, GaInAsSb, and InPAsSb: Key properties for a variety of the 2–4- μm optoelectronic device applications,” *Journal of applied physics*, vol. 61, no. 10, pp. 4869–4876, 1987.
- [172] J. R. Chelikowsky and M. L. Cohen, “Nonlocal pseudopotential calculations for the electronic structure of eleven Diamond and Zinc-Blende semiconductors,” *Physical Review B*, vol. 14, no. 2, p. 556, 1976.
- [173] M. Bernardi, D. Vigil-Fowler, J. Lischner, J. B. Neaton, and S. G. Louie, “Ab initio study of hot carriers in the first picosecond after sunlight absorption in silicon,” *Physical review letters*, vol. 112, no. 25, p. 257402, 2014.
- [174] F. Giustino, M. L. C. L, and S. G. Louie, “Electron-phonon interaction using Wannier functions,” *Physical Review B*, vol. 76, no. 16, p. 165108, 2007.
- [175] J. Noffsinger, F. Giustino, B. D. Malone, C.-H. Park, S. G. Louie, and M. L. Cohen, “EPW: A program for calculating the electron–phonon coupling using maximally localized Wannier functions,” *Computer Physics Communications*, vol. 181, no. 12, pp. 2140–2148, 2010.
- [176] W. Kohn and L. J. Sham, “Self-consistent equations including exchange and correlation effects,” *Physical Review*, vol. 140, no. 4A, p. A1133, 1965.
- [177] N. Troullier and J. L. Martins, “Efficient pseudopotentials for plane-wave calculations,” *Physical Review B*, vol. 43, no. 3, p. 1993, 1991.
- [178] H. J. Monkhorst and J. D. Pack, “Special points for Brillouin-zone integrations,” *Phys. Rev. B*, vol. 13, pp. 5188–5192, June 1976.
- [179] R. di Meo, A. D. Corso, P. Giannozzi, and S. Cozzini, “Calculation of phonon dispersions on the grid using Quantum ESPRESSO,” *Proc. COST School (Trieste)*, 2009.
- [180] G. Onida, L. Reining, and A. Rubio, “Electronic excitations: density-functional versus many-body Green’s-function approaches,” *Rev. Mod. Phys.*, vol. 74, p. 601, April 2002.
- [181] L. Hedin, “New method for calculating the one-particle Green’s function with application to the electron-gas problem,” *Phys. Rev.*, vol. 139, no. 3A, pp. A796–A823, 1965.
- [182] Y.-S. Kim, K. Hummer, and G. Kresse, “Accurate band structures and effective masses for InP, InAs, and InSb using hybrid functionals,” *Physical Review B*, vol. 80, no. 3, p. 035203, 2009.
- [183] M. Cardona, N. E. Christensen, and G. Fasol, “Relativistic band structure and spin-orbit splitting of Zinc-Blende-type semiconductors,” *Physical Review B*, vol. 38, no. 3, p. 1806, 1988.
- [184] S. Adachi, “Material parameters of $\text{In}_{1-x}\text{Ga}_x\text{As}_y\text{P}_{1-y}$ and related binaries,” *Journal of Applied Physics*, vol. 53, no. 12, pp. 8775–8792, 1982.

- [185] J. Heyd, G. E. Scuseria, and M. Ernzerhof, “Hybrid functionals based on a screened Coulomb potential,” *The Journal of Chemical Physics*, vol. 118, no. 18, pp. 8207–8215, 2003.
- [186] W. Weber, “Adiabatic bond charge model for the phonons in Diamond, Si, Ge, and α -Sn,” *Physical Review B*, vol. 15, no. 10, p. 4789, 1977.

Notations

a	Lattice parameter (\AA)
$C_{I,\alpha;J,\beta}(l,l')$	Second-order interatomic force constant matrix ($eV.\text{\AA}^{-2}$)
$C_{I,\alpha;J,\beta;K,\gamma}(l,l',l'')$	Third-order anharmonic tensor ($eV.\text{\AA}^{-3}$)
D	Electric induction ($C.m^{-2}$)
$D_{I,\alpha;J,\beta}(l,l')$	Dynamical matrix $eV.\text{\AA}^{-2}.(a.u.m.)^{-1}$
E	LO-phonon-induced macroscopic electric field ($V.m^{-1}$)
$e_{I,\alpha}$	Phonon eigenmode element
E	Electron energy (eV)
$E_e^{e(h)}xt$	Hot electron (holes) extraction energy (eV)
E_g	Band gap (eV)
E_{tot}	Crystal total energy (eV)
$\hbar\omega$	Phonon energy (cm^{-1})
I_{Bloch}	Bloch function periodic part overlap
I, J, K	Atom labels
k	Electronic wavevector (m^{-1})
l, l', l''	Atomic cell labels
n	Electronic density (cm^{-3})
\tilde{n}_c	Hot-carrier effect threshold electronic density (cm^{-3})
M_I	Atomic mass ($a.u.m.$)
N	Number of unit cell
N_{at}	Number of atoms
P	Dielectric polarisability ($C.m^{-2}$)
q	Phonon wavevector (m^{-1})
Q	Thermalisation factor ($W.K^{-1}.cm^{-2}$)
s	Phonon mode label
T_C	Carrier temperature (T)
u	Atomic displacement
U	Fröhlich effective charge (m^{-3})
Z	Atomic charge (C)

\mathbf{Z}^*	Born effective charge
α, β, γ	Coordinate labels
α_F	Fröhlich coupling constant
Γ	Quantum rate (s^{-1})
δE	Energy selective contact width (eV)
$\delta\mu$	Quasi Fermi level splitting (eV)
Δ	Numerical rectangular <i>delta</i> function (cm^{-1})
ϵ_0	Low frequency dielectric tensor ($F.m^{-1}$)
ϵ_∞	High frequency dielectric tensor ($F.m^{-1}$)
τ	Lifetime (ps)
χ_∞	High frequency susceptibility tensor ($F.m^{-1}$)
ψ	Electronic wavefunction
Ω	Unit cell volume (\AA^3)
BZ	Brillouin zone
DFT	Density Functional Theory
DFPT	Density Functional Perturbation Theory
ELR	Energy Loss Rate
FCC	Face-centred cubic
LA	Longitudinal acoustic
LO	Longitudinal optic
TA	Transverse acoustic
TO	Transverse acoustic
PhDOS	Phonon density of states
1PhDOS	One-phonon density of states
2PhDOS	Two-phonon density of states
PV	Photovoltaic
TDDFT	Time Dependent Density Functional Theory
TPFS	Two-phonon final states

List of publications

Reviewed publications

- 1 Phonon lifetime in SiSn and its suitability for Hot Carrier Solar Cells
H. Levard, S. Laribi, J.-F. Guillemoles
Applied Physics Letters 104, 222106 (2014)
- 2 Optical phonon decay in cubic semiconductors: a hot carrier solar cell picture
H. Levard, S. Laribi, JF Guillemoles
International Society for Optics and Photonics
SPIE Proceeding, 8981OH, 2012

Chapter of book

- 1 Hot-Carrier Solar Cells
G. Conibeer, J.-F. Guillemoles, Feng Yu and **H. Levard**
Advanced Concepts in Photovoltaics, Royal Chemical Society, 2014

Oral presentations

- 1 Study of LO-phonon decay in semiconductors for hot carrier solar cells
APS March meeting, Denver, Colorado, USA, 03-07/03/2014
H. Levard, J. Vidal, S. Laribi, J.-F. Guillemoles
- 2 LO-phonon decay in semiconductors for hot-carrier solar cells : needs, tools, limits
SPIE Photonic West, San Francisco, California, USA, 03-06/02/2014
H. Levard, J. Vidal, S. Laribi, J.-F. Guillemoles
- 3 SiSn as an ideal candidate for hot carrier solar cell absorber ?
EuroMat, Sevilla, Spain, 09-13/09/2013
H. Levard, S. Laribi, J.-F. Guillemoles
- 4 Study of LO-phonon decay in semiconductors for hot carrier solar cells
EuroMat, Sevilla, Spain 09-13/09/2013
H. Levard, S. Laribi, J.-F. Guillemoles
- 5 SiSn as an ideal candidate for hot carrier solar cell absorber ?
European Material Research Society Spring Meeting, Strasbourg, France, 27-31/05/2013
H. Levard, S. Laribi, J.-F. Guillemoles

Visual presentations

- 1 Phonon issues in hot-carrier solar cells
H. Levard, S. Laribi, J.-F. Guillemoles
TRNM VII (Toward Reality is Nanoscale Materials), Levy, Finland, 10-12/02/2014
- 2 Phonon issues in Hot Carrier Solar Cells
H. Levard, S. Laribi, J.-F. Guillemoles
ComMat2013, summerschool, Bakou(Azerbadjan), 01-06/07/2013
- 3 Ab Initio calculation of optical phonon lifetime in III-V and IV-IV semiconductors for hot carriers solar cells
H. Levard, S. Laribi, J.-F. Guillemoles
EMRS(European Material Research Society) ,Fall 2012, Varsovie, Pologne, 17-21/09/2012
- 4 Ab Initio calculation of optical phonon lifetime in III-V and IV-IV semiconductors for hot carriers solar cells
H. Levard, S. Laribi, J.-F. Guillemoles
HEMP12 (High Efficiency Materials for Photovoltaics), Londres, 17-18/08/2012
- 5 LO-phonon lifetime in III-V semiconductors through DFPT Ab Initio calculations for hot carrier solar cells
H. Levard, S. Laribi, J.-F. Guillemoles
PVTC 2012 (Photovoltaic Technical Conference), Aix-en-Provence, 06-08/06/2012

Proceedings

- 1 Advanced Modeling of Hot Carrier Effects in 3rd Generation Solar
E Tea, **H. Levard**, H. Hamzeh, A. Le Bris, F. Aniel, S. Laribi, JF Guillemoles
Proceeding of the 27th European Photovoltaic Solar Energy Conference, 2012
- 2 Hot Carrier Solar Cell: From Simulation to Devices
J. Rodière, **H. Levard**, A. Le Bris, S. Laribi, L. Lombez, JF Guillemoles
Proceeding of the 27th European Photovoltaic Solar Energy Conference, 2012

Prize

- 1 Best Poster award, at ComMat 2013 summer school, Baku, Azerbaijan
Phonon issues in hot-carrier solar cells
H. Levard, S. Laribi, JF Guillemoles

Abstract

This thesis deals with fundamental issues related to phonons in hot-carrier solar cells, a third generation photovoltaic technology. This concept aims at extracting photogenerated charge carriers before they reach a thermal equilibrium with the lattice, and exhibits a theoretical efficiency close to thermodynamic limit. One of the main issue is to hinder carrier cooling, which occurs through LO-phonon emission. In addition to the idea of screening the electron-phonon interaction, one approach consists in designing an absorber in which the LO-phonon has an intrinsic lifetime longer than what it is in conventional materials, enhancing the rate of its reabsorption by the carriers. The LO-phonon decay and lifetime is first investigated in semiconductors within density functional perturbation theory. Specific criteria for relevant absorbing materials choosing, from a phonon point of view, are derived. A full study of the LO-phonon lifetime is performed on a singular material, and the possibility to achieve the sufficient phononic requirements is discussed. Secondly, the above-mentioned electron-phonon interaction is modelled in superlattices. The coupling strength is related to the LO-phonon induced macroscopic electric field, which allows to study the directional dependence of the phonon emission. The latter reveals to differently affect the dimensionality of the electronic and phononic interacting populations. This study calls for development of these structure in the framewok of hot-carrier solar cells.

Résumé court en français

Cette thèse traite des problématiques fondamentales liées aux phonons dans le cadre des cellules solaires à porteurs chauds. Ce concept appartient aux technologies photovoltaïques dites de troisième génération, et vise à l'extraction des porteurs de charges photogénérés non-encore à l'équilibre thermique avec le réseau cristallin, ce qui conduit à un rendement théorique maximum de l'ordre de la limite thermodynamique. Un des enjeux majeurs est ainsi le ralentissement du refroidissement des porteurs, refroidissement qui se traduit principalement par l'émission de phonon LO via l'interactions électron-phonon. En plus de l'idée d'écranter ce dernier processus, une approche consiste à concevoir un matériau absorbeur dans lequel le phonon LO présente un temps de vie intrinsèque plus long qu'il ne l'est dans les matériaux classiques, favorisant ainsi sa réabsorption par les porteurs. Dans une première partie, et utilisant la théorie de la fonctionnelle densité perturbée, la décomposition du phonon LO est étudiée en terme d'états finaux disponibles. Suit une discussion sur le calcul du temps de vie de ces phonons, et sur la possibilité d'atteindre les critères phononiques définis comme suffisants. Dans une deuxième partie, une étude de l'interaction électron-phonon est menée dans les super-réseaux. La constante de couplage est reliée au champ électrique macroscopique induit par le phonon LO, de sorte à pouvoir précisément rendre compte de son anisotropie. Il apparaît que la dimensionalité des populations électroniques et phononiques est différemment affectée. Cette étude appelle à développer l'analyse de ce type de structure dans le cadre des cellules à porteurs chauds.

